

# **The Madden-Julian Oscillation: Observation, Modeling, and Theory**

Thesis by  
**Da Yang**

In Partial Fulfillment of the Requirements for the Degree  
of  
Doctor of Philosophy



CALIFORNIA INSTITUTE OF TECHNOLOGY

Pasadena, California

2014

(Defended May 9, 2014)



*To my parents*

## Acknowledgements

It has been five years and nine months since I first joined Caltech as a graduate student. I appreciate the scientific training that I received at Caltech, and I have also enjoyed my time in Pasadena. Here I would like to express my gratitude to people who helped to make this thesis possible and to make my graduate school smooth sailing.

I am deeply indebted to my thesis advisor Andy Ingersoll for his helpful input on all of the chapters of this thesis. I thank Andy for offering me complete freedom and also for being unconditionally reliable over the whole course of my graduate school. I also thank Andy for constantly reminding me of the importance of observation when I was immersed in developing theories. I not only appreciate Andy's influence on my scientific development, but I also appreciate his balance between work and family life. Additionally, I was delighted every time that I received an invitation to the Ingersoll family Thanksgiving dinner. I will miss it.

I would like to thank my other thesis committee members for education and thoughtful considerations of my research. I thank Tapio Schneider for his insightful lectures on atmospheric circulations and useful suggestions on my research. I also thank Tapio and his group for maintaining the GCM used in Chapter 5. I thank Simona Bordoni for spending many hours in her office discussing my research and offering advice on my career. I have also benefited from Simona's discussion group by either leading the discussion or listening to other people's opinions. I thank Andy Thompson for his thorough introduction to physical oceanography and related topics. I thank Duane Waliser for being supportive over the whole course of this thesis. I thank Duane for his helpful suggestions and for introducing me to a larger MJO community. I thank Yuk Yung for his interests on my MJO research. I have also benefited from discussing my research with Yuk Lunch Seminar speakers. I thank Joao Texiera for teaching me boundary layer dynamics and inviting me to JPL to give a seminar.

I have also benefited from having conversations with scientists from other institutes. I would like to particularly thank Zhiming Kuang and George Kiladis for their encouragement on my research and advice on my career over the past few years. I also thank Zhiming for sharing his experience of being a graduate student at Caltech.

It would not be possible to have a joyful graduate school experience without friends. Yue and Xi picked me up at LAX, and this marked my start at Caltech. I thank Alex for treating me to my first cereal breakfast, and Mike for generously giving me a nickname soon after we met each other. I thank Lindsay for making me my first homemade birthday cakes and for baking cookies for many lunches at Caltech. I thank Zan, the best roommate, together with Na, for sharing many enjoyable moments with me. I thank Zhihong for many helpful conversations on moist convection and numerical methods. I also enjoyed watching him eating five full plates at the Ath and sharing hotel rooms with him at conferences. I thank Xuan for regularly stopping by my office and distracting me at the moments when I was focusing on my research. I enjoyed playing basketball and dining out with Maolin and other CaltechC members. I also want to thank my wonderful officemates, especially Joe and Coco, for pushing me to work harder by coming early in the morning and leaving late at night.

Lastly, I would like to give my most sincere gratitude to my parents, to whom this thesis is dedicated. My parents nurture me with the best they can provide. My parents have visited me regularly during my time at Caltech and have comforted my homesickness. My parents have taken good care of each other in my absence, and let their only child pursue his own dream away from home.



## ABSTRACT

The Madden-Julian Oscillation (MJO) is a pattern of intense rainfall and associated planetary-scale circulations in the tropical atmosphere, with a recurrence interval of 30-90 days. Although the MJO was first discovered 40 years ago, it is still a challenge to simulate the MJO in general circulation models (GCMs), and even with simple models it is difficult to agree on the basic mechanisms. This deficiency is mainly due to our poor understanding of moist convection—deep cumulus clouds and thunderstorms, which occur at scales that are smaller than the resolution elements of the GCMs. Moist convection is the most important mechanism for transporting energy from the ocean to the atmosphere. Success in simulating the MJO will improve our understanding of moist convection and thereby improve weather and climate forecasting.

We address this fundamental subject by analyzing observational datasets, constructing a hierarchy of numerical models, and developing theories. Parameters of the models are taken from observation, and the simulated MJO fits the data without further adjustments. The major findings include: 1) the MJO may be an ensemble of convection events linked together by small-scale high-frequency inertia-gravity waves; 2) the eastward propagation of the MJO is determined by the difference between the eastward and westward phase speeds of the waves; 3) the planetary scale of the MJO is the length over which temperature anomalies can be effectively smoothed by gravity waves; 4) the strength of the MJO increases with the typical strength of convection, which increases in a warming climate; 5)

the horizontal scale of the MJO increases with the spatial frequency of convection; and  
6) triggered convection, where potential energy accumulates until a threshold is reached, is important in simulating the MJO. Our findings challenge previous paradigms, which consider the MJO as a large-scale mode, and point to ways for improving the climate models.

# CONTENTS

<b>Acknowledgements</b> .....	iv
<b>Abstract</b> .....	vi
<b>Contents</b> .....	viii
<b>List of Figures</b> .....	xi
<b>List of Tables</b> .....	xviii
<b>Chapter I: Introduction</b> .....	1
1.1 Motivation .....	1
1.2 Observations.....	4
1.3 Moist Convection.....	7
1.3.1 Quasi-Equilibrium Convection.....	8
1.3.1 Triggered Convection .....	8
1.4 Comprehensive Modeling Efforts.....	9
1.5 Theoretical Considerations .....	10
1.5.1 A Large-Scale Unstable Mode.....	11
1.5.2 Multiscale Interaction .....	15
1.5.3 An Envelope.....	17
1.6 Outline of This Thesis.....	19
<b>Chapter II: Testing the Hypothesis</b>	
<b>That the MJO is an MRG Wave Packet</b> .....	27
2.1 Abstract .....	27
2.2 Introduction .....	28
2.3 Theory and Modeling.....	33
2.4 Data Analysis .....	45

2.5	Discussion and Conclusions .....	53
<b>Chapter III: Triggered Convection, Gravity Waves, and the MJO:</b>		
	<b>A Shallow Water Model .....</b>	<b>61</b>
3.1	Abstract .....	61
3.2	Introduction .....	62
3.3	Model Description.....	66
3.4	Simulation Results .....	70
3.5	Proposed Mechanism.....	77
3.6	Discussion and Conclusions .....	85
<b>Chapter IV: A Theory of the MJO Horizontal Scale.....</b>		
4.1	Abstract .....	93
4.2	Introduction .....	94
4.3	2D Shallow Water Model .....	96
4.4	1D $\beta$ -plane Model .....	102
4.5	Conclusion and Discussions .....	105
<b>Chapter V: Simulating the MJO in a 3D Model</b>		
	<b>with a Convection threshold leading to intermittency .....</b>	<b>111</b>
5.1	Abstract .....	111
5.2	Introduction .....	112
5.3	Model and Experiment Setup .....	114
5.4	Simulation Results .....	115
5.5	Conclusion and Discussions .....	122
<b>Chapter VI: Conclusion and Discussion.....</b>		
6.1	Conclusion.....	129
6.2	Discussion.....	130



## LIST OF FIGURES

- 1.1 Longitude-time diagrams of deep cloud clusters (cloud top infrared temperature  $<208$  K) over  $0^{\circ}$ – $10^{\circ}$ S for (a) 1–31 December 1992 during which an MJO event propagated through the eastern Indian and western Pacific oceans (Yanai et al. 2000). (b) Details for 20–31 December as marked by the lower right box in Fig. 8a. (c) Details for 22–28 December as marked by the box in Figure 8b. Sizes of ovals are proportional to the actual sizes of cloud clusters. From Chen et al. (1996). .....3
- 1.2 Wave number–frequency power spectrum of the symmetric component of Cloud Archive User Services (CLAUS)  $T_b$  for July 1983 to June 2005, summed from  $15^{\circ}$ N to  $15^{\circ}$ S, plotted as the ratio between raw  $T_b$  power and the power in a smoothed red noise background spectrum (see Wheeler and Kiladis 1999 for details). Contour interval is 0.1, and contours and shading begin at 1.1, where the signal is significant at greater than the 95% level. Dispersion curves for the Kelvin,  $n = 1$  equatorial Rossby (ER),  $n = 1$  westward inertio-gravity (WIG) waves are plotted for equivalent depths of 8, 12, 25, 50, and 90 m. From Kiladis et al. (2009). .....4
- 1.3 Anomalous OLR and circulation from ERA-15 reanalysis on day 0 associated with a  $-40$   $\text{W/m}^2$  perturbation in MJO-filtered OLR at the equator,  $155^{\circ}$ E for the period 1979–93, all seasons included; (a) 850 and (b) 200 hPa. Dark (light) shading denotes OLR anomalies less than  $-32$   $\text{W/m}^2$  ( $-16$   $\text{W/m}^2$ ). Streamfunction contour interval is (a)  $4 \times 10^5$   $\text{m}^2/\text{s}$  and (b)  $10 \times 10^5$   $\text{m}^2/\text{s}$ . Locally statistically significant wind vectors at the 95% level are shown. The largest vectors are about 2 m/s in (a) and around 5 m/s in (b). From Kiladis et al. (2005). .....6

- 1.4 Zonal/height cross section of anomalous zonal wind along the equator associated with the pattern in Fig. 1.3. Contour interval is 0.5 m/s; negative contours dashed. Dark (light) shading denotes anomalies greater than (less than)  $\pm 0.5$  m/s. The associated OLR anomaly along the equator is shown at the top in  $\text{W/m}^2$ . From Kiladis et al. (2005). .....7
- 2.1 Longitude-time diagrams of the brightness temperature over  $0^\circ - 10^\circ\text{S}$  for 2 – 31 December 1992, during which an MJO event propagated through the eastern Indian and western Pacific oceans (the same time interval as in Fig. 11 of Chen et al. 1996). Dark represents low brightness temperature, which means high clouds; white represents high brightness temperature.....31
- 2.2 (a) WIG and EIG waves (dot-dashed), MRG waves (solid), equatorial Rossby (ER) waves (marked with x), and Kelvin waves (marked with o). (b) The corresponding group velocities. All the curves are for equivalent depth = 25 m. The Kelvin wave phase speed and group velocity are both equal to  $c = 15.7 \text{ m s}^{-1}$ . .....34
- 2.3 Longitude–time diagrams of the air temperature anomaly in the GCM at  $\sigma \approx 0.5$ . Temperature has been averaged from  $0^\circ\text{N}$  to  $4.2^\circ\text{N}$ . The blue represents a negative temperature anomaly, and the red is a positive anomaly. (a) Source moves west at  $9 \text{ m s}^{-1}$  and lasts for 20 days; boundary-layer damping is  $1 \text{ day}^{-1}$ . (b) Same as (a) except there is no boundary layer damping. (c) Same as (a) except source lasts for 10 days. (d) Same as (a) except source moves at  $4 \text{ m s}^{-1}$ . (e) Same as (a) except source moves east at  $9 \text{ m s}^{-1}$ . (f) Same as (e) except the source moves to the east at  $4 \text{ m s}^{-1}$  and there is no boundary layer damping. ....38
- 2.4 Time-longitude diagram of the air temperature anomaly in the GCM at  $\sigma \approx 0.5$ . Temperature has been averaged from  $4.2^\circ\text{N}$  to  $9.8^\circ\text{N}$ . Anomaly increases with the darkness of the color. The source is a dipole – a positive heating anomaly to the north and a negative anomaly to the south, which is the same as for Fig. 2.3a except the zero line has been

	displaced north from the equator to latitude $5.6^\circ$ . (a) Source moving to the west at $\sim 9 \text{ m s}^{-1}$ . (b) Source moving to the west at $\sim 4 \text{ m s}^{-1}$ . (c) Source moving to the east at $\sim 9 \text{ m s}^{-1}$ . (d) Source moving to the east at $\sim 4 \text{ m s}^{-1}$ . .....	40
2.5	(a) Map view of the MRG divergence field at $\sim 160\text{mb}$ . White represents positive divergence, and black represents negative divergence. Contour intervals are equal. (b) Map view of the rectified MRG divergence field. The white is high, the black is low, and the gray is in between. ....	42
2.6	Pressure-time cross section of the temperature anomaly at $5^\circ\text{N}$ , $220^\circ\text{E}$ . ....	43
2.7	(a) Zonal wavenumber-frequency power spectra of the antisymmetric component of OLR, calculated for the entire period of record from 1974 to 2009. The superimposed green line is the inertio-gravity wave; the red lines are the MRG waves with equivalent depths of 8 and 250 m. (b) As in (a), but for the symmetric component. The green curve is the WIG and EIG wave; blue is the ER wave, and black is the Kelvin wave with equivalent depths of 8 and 90 m. Although not predicted by linear wave theory, the MJO is the power that is concentrated in the white box to the right of center and close to the horizontal axis. For all components, the power has been summed over $10^\circ\text{S} - 10^\circ\text{N}$ . Solid boxes represent regions used in the wavenumber-frequency filtering. ....	46
2.8	(a) The longitude-time diagrams of the OLR ( $\text{W m}^{-2}$ ) averaged for the latitudes from $10^\circ\text{S}$ to $5^\circ\text{N}$ . The record extends from July 11 to August 19, 1985. (b) Longitude-time section of OLR anomalies for the MJO-filtered band for the same 40 day period as in (a). (c) The MRG-filtered band for the same 40-day period. (d) The rectified MRG waves for the same 40-day period. ....	48
2.9	The joint probability distribution (JPD) of the MJO with (a) the rectified westward MRG waves, (b) the rectified eastward MRG waves, (c) the rectified Kelvin waves and (d) the rectified EIG waves, (e) the rectified ER waves, (f) the rectified WIG waves. We filter using the Fourier	

coefficients within the boxes shown in Fig. 2.7. These coefficients were computed from the full global data set. After inverting the filtered coefficients to a time-longitude plot, we construct the JPD from the Indian Ocean section, 10°S-5°N, 75°-100°E. The contour intervals are the same for each figure, and the maximum and minimum values are also the same. The downward tilt to the right in 2.9a and 2.9b is evidence that the rectified MRG waves are correlated with low OLR in the MJO frequency band. ....51

2.10 The same as Fig. 2.9, except for that these coefficients were computed for just the winter season (November to April) and the longitude range from 75°-185°E. ....52

3.1 Hovmöller diagrams of the (a) geopotential, (b) zonal wind, (c) meridional wind, and (d) convective heating of our shallow-water simulation from -15° to 15° latitude. The geopotential, zonal wind, and convective heating are symmetric components about the equator, and the meridional wind is the antisymmetric component. The white (black) represents low (high), and the contour interval is linear. The forcing amplitude is arbitrarily small. Therefore, the absolute value of our model output is not important. The dashed and solid lines represent MJO events A and B, respectively, and the propagation speeds are both about 3.0 m/s. ....72

3.2 Hovmöller diagrams of zonal wind from (a) T85 and (b) T170 simulations. Colors and contour intervals are as in Fig. 3.1b. ....73

3.3 Zonal wavenumber–frequency power spectra of zonal wind from -15° to 15° latitude for (a) symmetric and (b) anti-symmetric components. Red represents high-power density, and blue represents low-power density. Red, blue, black, and green lines denote dispersion curves of IG, Rossby, Kelvin, and MRG waves, respectively, for different meridional modes. The white box in (a) ranges from 1 to 5 in wavenumber and

- from 1/60 to 1/200 cpd in frequency. The logarithm to the base 10 is taken for plotting, and the contour interval is 0.5. ....75
- 3.4 Longitude–latitude map of composites of the MJO-like signals. The arrows denote the wind field  $\mathbf{V} = (u, v)$ , and the contours denote the geopotential. The thick solid (thin dashed) contours represent positive (negative) anomalies with linear contour intervals. ....76
- 3.5 High-resolution Hovmöller diagrams of the (a) geopotential, (b) zonal wind, (c) meridional wind, and (d) convective heating of our shallow-water simulation from  $-6^\circ$  to  $6^\circ$  latitude. The geopotential, zonal wind, and convective heating are symmetric components about the equator, and the meridional wind is the antisymmetric component. The black (gray) line denotes positive (negative) anomalies with linear contour intervals. ....79
- 3.6 Propagation speed (m/s) vs quasi frequency (cpd). The lower and upper solid lines are derived from the dispersion relations of the  $n = 1$  and  $n = 3$  IG waves, respectively. The markers represent the simulation results for different parameters. The thicker markers are for the T170 simulations, and the thin ones are for T85 simulations. The markers are red when  $\dot{\Sigma} = \dot{\Sigma}_0$ , blue when  $\dot{\Sigma} = 0.5\dot{\Sigma}_0$ , and black when  $\dot{\Sigma} = 0.25\dot{\Sigma}_0$ . The triangles are for simulations when  $R = R_0$ , and the circles are for simulations when  $R = 0.5R_0$ , where  $R_0 = 3.0^\circ$ . For example, a thick red circle is from the T170 simulation with  $\dot{\Sigma} = \dot{\Sigma}_0$  and  $R = 0.5R_0$ . We convert  $\tau_c$  to frequency by using frequency equals  $1/2\tau_c$ . The values of  $R_0$  and  $\dot{\Sigma}_0$  are given in Table 1. ....81
- 3.7 Zonal wavenumber vs normalized convection rate  $\dot{\Sigma}/\dot{\Sigma}_0$ , where  $\dot{\Sigma}_0$  is given in Table 1. ....82
- 4.1 Sensitivity study results in 10-based logarithmic scale. (a) the MJO wavenumber  $k$  vs number density of convection  $S_c$  ( $a^{-2} \text{ day}^{-1}$ ). Different colors represent simulations with different Kelvin wave speeds. They

- increase from red to blue, and the values are  $\sim 3, 6, 12, 16, 19 \text{ m s}^{-1}$ . The solid (dashed) line is with the slope of 0.43 (0.33). (b)  $k$  vs. Kelvin wave speed  $c$  ( $a \text{ day}^{-1}$ ). The solid (dashed) line has a slope of -0.82 (-0.62). (c)  $k$  vs. the radius of a convection event  $R_c$  ( $a$ ). The solid (dashed) line has a slope of 0.43 (0.49). (d)  $k$  vs  $\tau_c$  (day). The solid (dashed) line has a slope of -0.3 (0.0). In (b), (c), and (d), colors represent simulations with  $S_c$  increasing from red to blue. The values of  $S_c$  are  $\sim (5.6 \ 11.2 \ 16.8 \ 22.4 \ 28.0) \ a^{-2} \ \text{day}^{-1}$ . .....99
- 4.2 The proposed scaling relation in a 10-based log-log plot. Each marker represents a simulation result. The dashed line has a slope of 1. .... 100
- 4.3 The power spectrum of  $\hat{u}$  from the 1D  $\beta$ -plane model. The contours show the power spectral density in intervals of log to the base 10. Red represents high-power density, and blue represents low-power density. Red, blue, and black lines denote dispersion curves of Rossby, IG, and Kelvin waves, respectively. .... 104
- 4.4 The 1D scaling relation in a 10-based log-log plot. Each marker represents a simulation result. The simulation results with  $\hat{R}_c = 0.4, 0.8, 1.6$  are labeled with squares, circles and triangles. The simulation results with  $\hat{\tau}_c = 0.2$  and  $0.4$  are labeled with thick and thin markers. The dashed line has a slope of 0.5. .... 106
- 5.1 Hovmoller diagram of precipitation anomalies ( $\text{kg/m}^2/\text{s}$ ) averaged over  $10^\circ\text{S}$  to  $10^\circ\text{N}$ . (a) Control experiment, (b)  $\delta q$  experiment, (c) CAPE experiment, (d) CIN experiment. The precipitation anomaly has been multiplied by 3 to illustrate in the same color scale. .... 116
- 5.2 Power spectra of the symmetric component of precipitation averaged over  $10^\circ\text{S}$  to  $10^\circ\text{N}$  in 10-based logarithm scale. Background spectra have been removed. (a) Control experiment, (b)  $\delta q$  experiment, (c) CAPE experiment, (d) CIN experiment. The colors represent the spectral power density, and solid lines show the dispersion relations of

- the lowest order symmetric equatorial waves at 15 m equivalent depth. The black line represents the Kelvin wave, the red line represents the Rossby wave, and the blue line represents the IG wave. The white box contains the MJO signal. .... 117
- 5.3 Horizontal and vertical structure of the MJO composite. (a) Map view of the MJO precipitation anomalies ( $10^{-4}$  kg/m<sup>2</sup>/s, colors). Vectors represent the MJO horizontal wind anomalies at  $\sim 200$  hPa. (b) Vertical cross section of the MJO. The color shows the correlation between the specific humidity and the MJO precipitation anomaly. The color interval in both panels is 0.1385, and white indicates zero correlation. .... 119
- 5.4 Normalized power spectrum of (a) the  $\delta q$  experiment, (b) the CAPE experiment, (c) the CIN experiment and (d) the CAPE experiment with zoomed in wavenumber and frequency range. Normalization means relative to the control experiment (Fig. 5.2a). The contour interval is 0.25 with a 10-based logarithm scale, and the zero line is labeled by the blue contour. The black line represents the Kelvin wave dispersion relation with equivalent depth as 15 m. The blue lines represent the IG wave dispersion relations with equivalent depths of 15 m and 250 m. The red lines represent the corresponding Rossby waves. .... 121



# LIST OF TABLES

3.1	Parameter values in the control simulation .....	70
3.2	Parameter ranges in Fig. 3.6. ....	78



# Chapter 1

## Introduction

### 1.1 Motivation

The Madden-Julian Oscillation (MJO) is a recurring pattern of intense rainfall and associated planetary-scale circulations with an irregular period of 30-90 days (Madden-Julian 1972; Zhang 2005). The MJO associated rainfall pattern initiates in the Indian Ocean and propagates eastward slowly ( $\sim 5$  m/s) until it reaches the dateline. The MJO associated large-scale circulation shows the first baroclinic structure, i.e., it is characterized by low-level convergence and upper level divergence (Hendon and Salby 1994; Kiladis et al. 2005). In addition, within its large-scale envelope, there are both westward- and eastward-moving fine-scale structures (e.g., Nakazawa 1988). Although the MJO was first discovered 40 years ago, it is still a challenge to simulate the MJO in a 3D model, and simple models disagree with basic mechanisms. Both the persistence and slow propagation speed of the MJO are still mysteries.

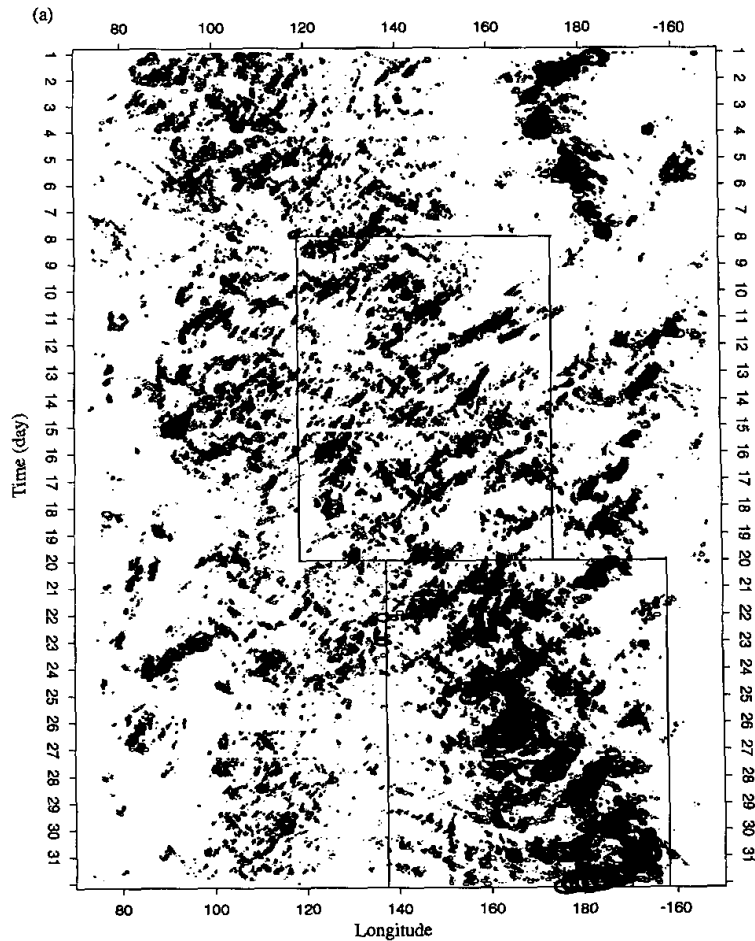
The MJO is the most dominant intraseasonal variability in the tropics. In addition to its impact on local weather, the MJO has a global impact on both weather and climate events

(Zhang 2013). At weather timescale, the large-scale circulation and thermal structure of the MJO serve as the background state for weather systems to develop. At climate timescale, the MJO can serve as high frequency forcing. Tropical cyclones vary coherently with the low-level zonal wind anomalies of the MJO and favor the westerly phase more than the easterly phase of the MJO (e.g., Maloney and Hartmann 2000). El Niño tends to be preceded by enhanced MJO activities and their associated westerly wind bursts (Seiki and Takayabu 2007). In a marginally unstable state, the westerly wind bursts are necessary to initiate El Niño in the tropical atmosphere-ocean system. Equatorial superrotation is observed in warm climate simulations and is attributed to the enhanced MJO activity in a warmer climate (Arnold et al. 2013; Caballero and Huber 2010). The MJO's global impact is therefore across a wide range of both temporal and spatial scales.

The MJO is a convectively coupled phenomenon—the interplay between the atmospheric motions and moist convection, in essence, thunderstorms. The difficulty in simulating the MJO shows our poor understanding of moist convection. Successfully simulating the MJO will improve our understanding of moist convection and renew our confidence in climate forecasting.

In the rest of this chapter, I will give an overview of our current understanding of the MJO with an emphasis on the theoretical aspect. For convenience to compare our results presented in this thesis with observations, I will first briefly introduce the observed MJO structures. Because the MJO at heart is a convectively coupled phenomenon, I will introduce moist convection and in principle how it is treated in 3D GCMs. I will also

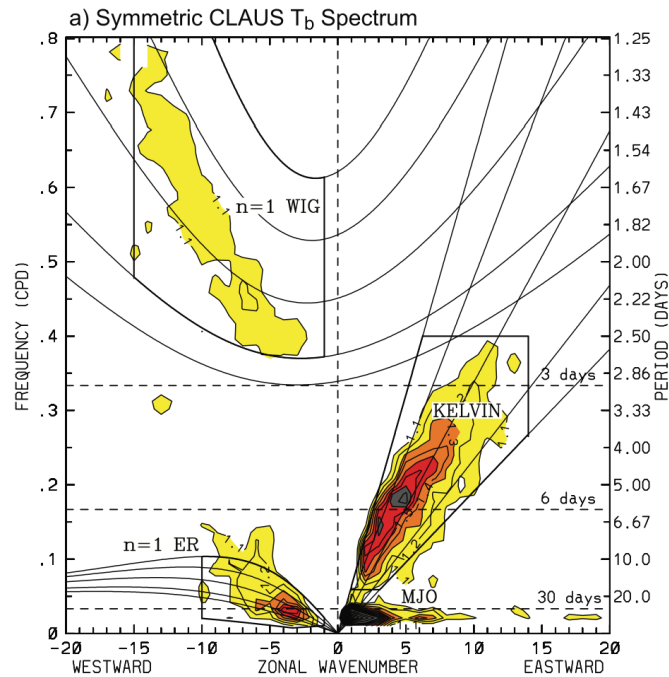
overview how the MJO is represented in state-of-the-art GCMs and then focus on the current MJO theories. Finally, I will outline this thesis.



**Figure 1.1.** Longitude-time diagrams of deep cloud clusters (cloud top infrared temperature  $<208$  K) over  $0^{\circ}$ – $10^{\circ}$ S for (a) 1–31 December 1992 during which an MJO event propagated through the eastern Indian and western Pacific oceans (Yanai et al. 2000). (b) Details for 20–31 December as marked by the lower right box in Figure 8a. (c) Details for 22–28 December as marked by the box in Figure 8b. Sizes of ovals are proportional to the actual sizes of cloud clusters. From Chen et al. (1996).

## 1.2 Observations

In this section, I will summarize the most basic observed features of the MJO, including its propagation behavior in a time-longitude (i.e., Hovmöller) diagram, its dispersion character in a power spectrum, and its horizontal and vertical structures. The purpose is for readers' convenience to compare my simulation results in later chapters with observations.



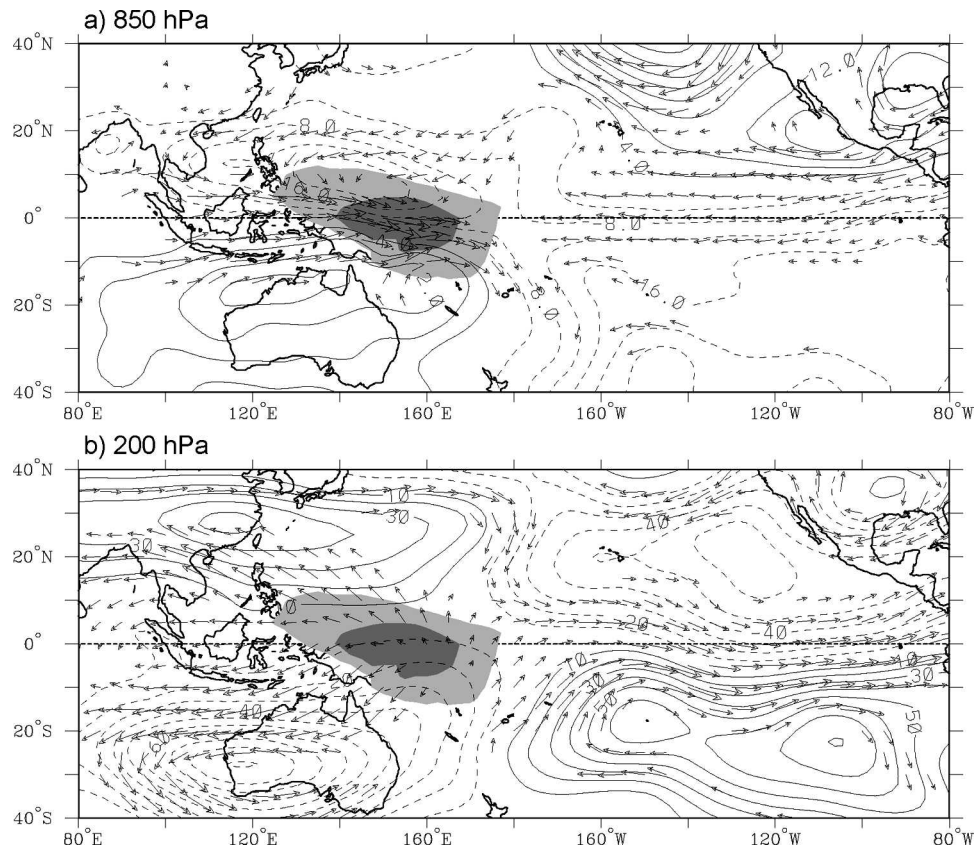
**Figure 1.2.** Wave number–frequency power spectrum of the symmetric component of Cloud Archive User Services (CLAUS)  $T_b$  for July 1983 to June 2005, summed from  $15^\circ\text{N}$  to  $15^\circ\text{S}$ , plotted as the ratio between raw  $T_b$  power and the power in a smoothed red noise background spectrum (see Wheeler and Kiladis 1999 for details). Contour interval is 0.1, and contours and shading begin at 1.1, where the signal is significant at greater than the 95% level. Dispersion curves for the Kelvin,  $n = 1$  equatorial Rossby (ER),  $n = 1$  westward inertio-gravity (WIG) waves are plotted for equivalent depths of 8, 12, 25, 50, and 90 m. From Kiladis et al. (2009).

Figure 1.1 shows a Hovmöller diagram of the brightness temperature in the tropics. Each strip is an image spanning 140 degrees of longitude and latitudes from 0° to 10°S. The black color represents low brightness temperature, which indicates high clouds and therefore precipitation systems. In this 30-day period, we see a large-scale envelope of precipitation systems initiating from the Indian Ocean and slowly propagating to the east at  $\sim 4$  m/s. This is a typical MJO event. Within the large-scale envelope, there are both westward- and eastward-moving small-scale structures. This is often referred as the multi-scale structure of the MJO.

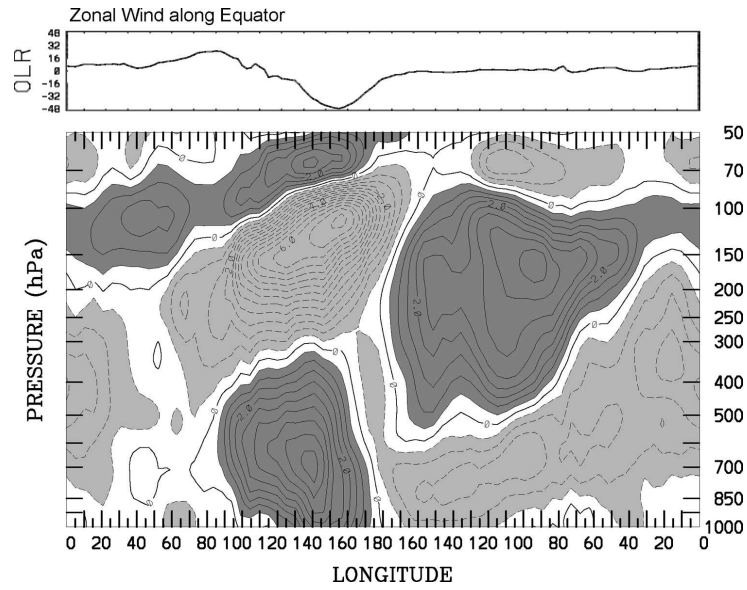
Figure 1.2 shows a 2D power spectrum of the symmetric component of brightness temperature in the tropics. The symmetry is with respect to the equator. The curves represent dispersion relations of the corresponding linear equatorial waves (Matsuno 1966) with different meridional modes and different equivalent depths. Prominent spectral peaks are oriented along these Matsuno dispersion curves. However, the MJO—the most dominant spectral peak—lies in the low-frequency and positive low-wavenumber region, and its dispersion character distinguishes it from the Matsuno modes.

Figure 1.3 shows the horizontal map view of the MJO composite at 200 and 850 hPa. The dark shading represents the MJO convective center. At 850 hPa, wind intrudes from subtropics to the west of the convective center and forms cyclonic gyres at the flanks. To the east, winds are easterlies and are more zonal, and the zonal wind converges slightly to the east of the convective center. This circulation pattern is generally interpreted as a forced response to a heat source in the tropics (Gill 1980). At 200 hPa, there is a significant

amount of divergent flow associated with the MJO convective center. In the subtropics, there are anticyclonic and cyclonic gyres to the west and east of the convective center, respectively. This wind structure—low-level convergence and upper-level divergence—suggests the first baroclinic vertical structure, which is further confirmed by Figure 1.4.



**Figure 1.3.** Anomalous OLR and circulation from ERA-15 reanalysis on day 0 associated with a  $-40 \text{ W/m}^2$  perturbation in MJO-filtered OLR at the equator,  $155^\circ\text{E}$  for the period 1979–93, all seasons included; (a) 850 and (b) 200 hPa. Dark (light) shading denotes OLR anomalies less than  $-32 \text{ W/m}^2$  ( $-16 \text{ W/m}^2$ ). Streamfunction contour interval is (a)  $4 \times 10^5 \text{ m}^2/\text{s}$  and (b)  $10 \times 10^5 \text{ m}^2/\text{s}$ . Locally statistically significant wind vectors at the 95% level are shown. The largest vectors are about 2 m/s in (a) and around 5 m/s in (b). From Kiladis et al. (2005).



**Figure 1.4.** Zonal/height cross section of anomalous zonal wind along the equator associated with the pattern in Fig. 1.3. Contour interval is 0.5 m/s; negative contours dashed. Dark (light) shading denotes anomalies greater than (less than)  $\pm 0.5$  m/s. The associated OLR anomaly along the equator is shown at the top in  $W/m^2$ . From Kiladis et al. (2005).

### 1.3 Moist Convection

Moist convection is a small-scale process, and the typical length scale of a thunderstorm is  $\sim 10$  km. Given the typical GCM grid spacing is  $\sim 100$  km, we cannot resolve moist convection and have to parameterize its effect on atmospheric flows. In a climate model the grid scale is much larger than the convection scale, and one must represent the collective effect of each convective storm on the atmospheric flows.

### 1.3.1 Quasi-Equilibrium Convection

Quasi-equilibrium (QE) convection is the convection scheme that only emphasizes its effect on large-scale, slowly varying circulations. For such circulations, convection can be viewed as in statistically equilibrium with its large-scale environment (Arakawa and Schubert 1974; Emanuel *et al.* 1994). The QE hypothesis can be formulated in terms of the convective available potential energy (CAPE), which measures the total buoyancy of a parcel lifting adiabatically from surface to the level of neutral buoyancy. According to this hypothesis, the generation of CAPE through large-scale processes, including radiation and surface heat fluxes, is consumed by convection roughly at the same rate. This idea is more transparent in a time-dependent differential equation (1.1).

$$\frac{\delta CAPE}{\delta \tau} = P - D, \quad (1.1)$$

where  $P$  and  $D$  represent production and destruction of CAPE, and  $\tau$  is the timescale that we are interested in. For slowly varying processes, the tendency term is small, and production is nearly balanced by destruction. This has at least two consequences. One is that the temperature profile in deep tropics, where convection is ubiquitous, follows the moist adiabat (e.g., Xu and Emanuel 1989). The other is that moist convection damps equatorial wave activities with preference on high-frequency waves (Emanuel *et al.* 1994). The Betts-Miller convection scheme used in Chapter 5 is consistent with this QE idea.

### 1.3.2 Triggered Convection

For high-frequency atmospheric circulations, the change in CAPE is not negligible, and the QE assumption does not apply. Such circulations depend crucially on when and how

convection is triggered—when a certain threshold in the environment is reached. For this reason, we refer to this type of convection as triggered convection. Triggered convection allows the environment to accumulate CAPE due to inhibitions, such as capping inversion and middle troposphere entrainment. This convection representation treats convection as a series of intermittent and energetic events. As opposed to QE convection, triggered convection excites high-frequency waves and brings kinetic energy into the atmosphere. Under QE assumption, moist convection is a moist form of dry convection. Triggered convection, however, can only happen in a moist atmosphere, and there is no counterpart in a dry atmosphere.

Although we can treat convection separately as QE or triggered convection in numerical models, there is no such distinction in nature. In reality, convection interacts with both large-scale slowly-varying circulations and small-scale short-lived atmospheric waves at once. These small-scale short-lived waves can organize together by interacting with convection, and the envelope of these waves can form a large-scale pattern. This is the idea we will further explore in later chapters.

## **1.4 Comprehensive Modeling Efforts**

Here I present progress in MJO simulations by using comprehensive 3D climate models, weather forecasting models, and a novel multi-scale modeling framework. The MJO simulations have been evaluated for models used in the Intergovernmental Panel on Climate Change (IPCC) Fourth and Fifth Assessment Report (AR4 and AR5) (Lin et al. 2006; Hung et al. 2013). Although the AR5 models show significant improvements from

the AR4 models in terms of the total intraseasonal variance, only one (Hung et al. 2013) of the twenty models is able to simulate realistic eastward propagation of the MJO.

However, the ECMWF weather forecast model shows improved MJO simulations with prescribed sea surface temperature (Bechtold et al. 2008). The improvement is obtained by making convection more sensitive to environmental moisture—by making entrainment a function of environmental relative humidity. This suggests that moisture-convection feedback—more moisture allows more convection, which in turn moistens the atmosphere—is important to the MJO.

A novel multi-scale modeling framework provides improved MJO simulations (e.g., Grabowski 2001, 2002, 2003; Randall et al. 2003). Superparameterized (SP-) Community Atmosphere Model (CAM), for example, replaces conventional parameterization with a 2D cloud-resolving model (CRM) to simulate convection explicitly in a small fraction of each grid box (Randall et al. 2003). This CRM runs continuously to provide averaged convective heating to compute the grid-scale fields, which in turn provide large-scale forcing to this CRM. Without assuming QE, this representation of convection is more accurate, and realistic MJOs have been simulated in the SPCAM (Benedict and Randall 2009, 2011).

## **1.5 Theoretical Considerations**

A successful MJO theory has to at least explain its propagation direction, speed, spatial and temporal scales, although only two of the latter three features are independent. In this section, I review works that aim at explaining one or more of the above features. These

works include quantitative theories and also observational and modeling evidence that support these theories. The goal here is to put major theoretical works into one big picture.

The trend for MJO theories shifts from emphasizing large-scale processes to small-scale processes. Before I started this thesis, there were mainly two schools of theories. One considers the MJO as a large-scale unstable mode, and the large-scale processes are responsible to the existence and propagation of the MJO. The other still considers the MJO as a larger-scale mode, but the major instability comes from smaller scales, and the scale interaction is crucial to the existence of the MJO. This thesis, together with other studies emerged recently, further emphasizes the role of small-scale high-frequency waves and proposes that the MJO is a rectified envelope of these waves—the third school of MJO theories. Here I will review important recipes in the first and second school of theories and discuss related caveats. I will also discuss evidence that motivates or supports the research presented in this thesis.

### **1.5.1 A Large-Scale Unstable Mode**

Due to its appearance, the MJO has been considered as a large-scale low-frequency phenomenon when the MJO was first discovered. Given its persistence, unstable theories have been proposed. The most popular theory in this category is the moisture mode theory. The moisture mode depends essentially on a prognostic equation of moisture and has no analog in a dry atmosphere (Sobel and Maloney 2012). Growth of such modes depends on positive feedbacks that increase the moist static energy (MSE) anomaly, a measure of the total energy perturbation. The propagation of such modes depends on processes that make

MSE anomalies move horizontally. The MSE is the sum of gravitational potential, sensible and latent energy, and is a materially conserved quantity in moist adiabatic processes by assuming hydrostatic balance. The change of column integrated MSE depends on diabatic processes. Here I will first introduce the key recipes in the moisture mode theory and then discuss a simple MJO model that emphasizes these essential recipes.

Several different but related physical processes have been considered as key recipes for the existence or propagation of the MJO, and they include: moisture-convection feedback, wind induced surface heat exchange (WISHE), cloud-radiation feedback, and horizontal advection of moisture. The first three provide energy to maintain the MJO, and the last one account for the eastward propagation. None of these processes directly account for the horizontal scale. Now I will introduce these processes in detail and also discuss the caveats.

- Moisture-convection feedback: Spatial fluctuations of deep convection cause perturbations of free-tropospheric moisture, which in turn affects the spatial distribution of deep convection. Improving the moisture-convection feedback can improve the MJO simulations (e.g., Grabowski 2004; Bechtold et al. 2008; Holloway et al. 2013). Raymond and Fuchs (2007) simulate a moisture mode by making precipitation a strong function of precipitable water in a toy model. They argue that this moisture mode bears similar dynamics to the MJO, but the growth rate of this moisture decreases with wavelength. Instead of supporting the MJO is a large-scale mode, this result may suggest that moisture-mode dynamics works more efficiently at small scales. Raymond and Fuchs (2009) adapt a similar

convection scheme to a 3D aquaplanet  $\beta$ -plane model with realistic sea surface temperatures and produce robust MJO-like signals. However, it is unclear what determines the propagation speed and horizontal scale of the MJO in this model.

- WISHE: Surface heat fluxes increase the column integrated MSE and can amplify positive MSE anomalies. Using observational datasets, Sobel et al. (2008 and reference therein) show that surface heat fluxes are correlated with precipitation at regions where the MJO is strong. Maloney et al. (2010) simulate the MJO over an aquaplanet and find robust MJO signals with interactive surface fluxes. When the interactive surface flux is turned off, the MJO disappears. This result, however, can be model dependent. Anderson and Kuang (2012) analyze the MJO simulated in the SPCAM and show that the MJO-related latent heat flux from surface to the atmosphere is a MSE sink, which tends to stabilize the environment and to damp the MJO. This suggests that WISHE is not essential to simulate the MJO in the SPCAM.
- Cloud-radiation feedback: Although the longwave radiation in general cools the atmosphere, high clouds associated with deep convection reduce the longwave radiation and are effective MSE sources in the perturbed sense. The MSE budget analysis shows that the cloud-radiation feedback is the dominant contribution to the MJO MSE anomalies in SPCAM simulations (e.g., Anderson and Kuang 2012; Arnold et al., 2013) and in observations from a recent field campaign (Sobel et al. 2014). However, other modeling studies suggest that cloud-radiation feedback is not essential to produce MJO-like signals (e.g., Grabowski 2003; Raymond and Fuchs 2009). They argue that other MSE sources provide stronger

feedback and can compensate the effect of cloud-radiation feedback. It is also possible that the MSE anomalies are passive responses to the existing eastward propagating MJO, and the MSE partition between different processes varies in different cases as a consequence.

- Horizontal advection: Given the small temperature gradient in the tropics, the horizontal moisture anomaly determines the MSE anomaly. Drying to the west and moistening to the east due to horizontal advection of moisture have been considered as the key for the eastward propagation of the MJO (e.g., Maloney 2009; Anderson and Kuang 2012; Arnold et al. 2013; Sobel et al. 2014).

Sobel and Maloney (2012, 2013) argue that a prognostic equation for moisture is essential to simulate the MJO and construct a semi-empirical model by parameterizing the important physical processes into their single prognostic equation—column water vapor equation. The included processes are mainly the processes discussed above and are selected based on the MSE analysis results. These authors found unstable modes in this model, and there are two major conclusions. One is that the MJO propagation is controlled by the mean westerly in the lower troposphere. The other is that only if another free parameter—water vapor diffusion—is added, the growth rate increases with wavelength. Otherwise, the largest growth rate is at the smallest scale. Unfortunately, both of the major findings are not consistent with SPCAM simulation results. Arnold et al. (2013) run the SPCAM over an aquaplanet with fixed SSTs, and the SST varies from 26°C to 35°C to represent different climate states. It is clear that the MJO propagation is not controlled by the lower troposphere mean wind speed. It is also clear that the MJO wavenumber shifts from the

cold climate to the warm climate. The wavenumber shift is robust and is further confirmed by studies under much wider range of climates (Yang and Pritchard 2014; Pritchard and Yang 2014).

Many efforts have been made to understand the MJO in the moisture-mode context, and yet theories fail to explain its propagation speed and horizontal scale. The recent development of the moisture mode theory heavily relies on the MSE analysis of the MJO composite, but such analysis has not proven that the MJO is a large-scale mode and cannot distinguish causalities. First, the moisture mode dynamics is in essence a way to provide energy for the MJO and can function at small scales as well. The common MSE analysis, however, has completely ignored the energy provided by small-scale processes by focusing on only the MSE budget of the MJO-composite, a filtered large-scale low-frequency signal. Second, such analyses are diagnoses and cannot distinguish causality. The large-scale Gill-type circulation (Gill 1980) propagating with the MJO is a forced response to the large-scale convective envelope. The MSE budget could be the same thing. This is a fundamental difference between the MJO and free convectively coupled equatorial waves.

### **1.5.2 Multiscale Interaction**

The second school of theory that still considers the MJO as a large-scale mode, but the major instability comes from smaller scales. Multi-scale interaction is therefore important to maintain the MJO—a neutral mode. Both observational and modeling evidence show that upscale convective momentum transport (CMT), from small scales to the MJO envelope, can provide energy to maintain the MJO. Here I first will review both

observational and modeling works that support the upscale CMT hypothesis, and then I will discuss a simple MJO model that emphasizes the role of multi-scale interaction.

The multi-scale structure is an intrinsic nature of tropical meteorology. Wheeler and Kiladis (1999) construct power spectra for the tropics by using the outgoing longwave radiation (OLR) dataset. They show that equatorial disturbances occur at all temporal and spatial scales, and that the spectral peaks correspond to the MJO and the theoretically predicted equatorial waves (Matsuno 1966). It is also known that in the large-scale MJO envelope, there are small-scale high-frequency activities moving at various speeds (e.g., Nakazawa 1988; Chen et al. 1996). These synoptic and mesoscale convective activities are enhanced during the active phase of the MJO (e.g., Hendon and Liebmann 1994; Yasunaga and Mapes 2011a, b).

Convective momentum transport (CMT) has been recognized as an important process to maintain the large-scale circulation of the MJO (Fig. 1.4). CMT is attributed to the well-observed tilting structure of tropical convective organizations, including mesoscale systems, and equatorial waves (e.g., Kiladis et al. 2009). Upscale CMT can enhance or reduce the vertical wind shear, and can therefore maintain one phase of the MJO or help to transition from one phase to the other. Grabowski (2002) successfully simulates the MJO with a superparameterized GCM, in which a 2D cloud-resolving model aligns either zonally or meridionally in each grid box. The zonal (meridional) alignment only allows zonal (meridional) CMT. The simulated MJOs are different in strength and horizontal scale in these two experiments, and these differences are obtained from different CMTs. The

author then suggests that CMT is important to the MJO. However, the MJO signal is robust in both experiments, and this suggests that CMT is not essential to the existence of the MJO. Khouider et al. (2012) use a 3D GCM to study the interaction between equatorial waves and the MJO. In their model, easterly and westerly phases of the MJO—the phases with corresponding surface winds—favor different equatorial waves, which in turn transport momentum and maintain the corresponding MJO phases. This work, however, does not address what sets the propagation speed and horizontal scale of the MJO.

Based on these studies, Majda and Stechmann (2009) present a simple MJO model that emphasizes the role of small-scale high-frequency waves. In their model, the effects of small-scale waves are parameterized, *i.e.*, the amplitude of the wave envelope matters. It is not important that any particular wave makes up the envelope. In this model, the MJO is a neutral mode, and the major instability is assumed to occur in the synoptic scale. This neutral mode oscillates at an intraseasonal timescale within a certain parameter range. However, this neutral mode does not prefer any propagation direction or any horizontal scale. This model therefore fails to explain the most fundamental features of the MJO.

### **1.5.3 An Envelope**

It is well known that in the large-scale MJO envelope, there are many small-scale high-frequency activities moving at various speeds (e.g., Nakazawa 1988; Chen et al. 1996). In this thesis, we propose that the MJO is the effect of convection driven by high-frequency small-scale waves. These waves, instead of feeding the MJO, are self-organized as the

MJO. To successfully simulate the MJO, it is important to represent these high-frequency small-scale waves well. Our idea is motivated or supported by the following research.

- The wave packet hypothesis: Wheeler and Kiladis (1999) point out that the mixed Rossby-gravity (MRG) wave group velocity is  $\sim 5$  m/s, which is close to the observed MJO propagation speed. Straub and Kiladis (2003) propose that the MJO could be a wave packet of the MRG waves and find the MRG variance and the MJO are significantly correlated, although the correlation is not large. In Chapter 2, we further test this hypothesis by using both an idealized GCM and the OLR dataset.
- Departures from QE convection: All recent successes in simulating the MJO in 3D models come from improved convection parameterization, and these improvements account for departures from QE convection in different ways. Increasing *moisture-convection feedback* (e.g., Bechtold et al. 2008) effectively inhibits occurrence of convection when there is not enough moisture. While accumulating moisture, CAPE is also increased. Replacing conventional parameterization by *superparameterization* (e.g., Benedict and Randall 2009) simulates moist convection and its interaction with environment more realistically. The simulated convection has a continuous spectrum from triggered convection to QE convection and treats small-scale high-frequency waves and large-scale low-frequency waves equally well. Including *multi-cloud types* (e.g., Khouider et al. 2011) in parameterization suggests that the column-integrated instability can be accumulated until the mid-troposphere is moistened by congestus. This behavior involves triggered convection.

- Observed precipitation events: Precipitation events in the active phase of the MJO are intermittent, and CAPE has significant changes in each precipitation events. In the dynamics of the MJO (DYNAMO) field campaign, for example, rainfall is separated by non-rainy days during the active phase of the MJO, and CAPE increases before maximum rainfall accumulation and then decreases. The magnitude of change in CAPE is  $\sim 300$  J/kg, which is a significant amount.

As discussed in Sections 1.5.1 and 1.5.2, the MJO has been considered as a large-scale mode for 40 years, and yet no theory accounts for its most basic features. This fact, together with the discussion in this section, suggests that one must take into account small-scale high-frequency waves and departures from QE convection in order to successfully simulate the MJO. In this thesis, we advance our understanding of the MJO by investigating how small-scale waves interact with convection and organize together as the MJO.

## **1.6 Outline of This Thesis**

The outstanding questions in this field include: What is the MJO and what determines its behavior? How does the MJO vary with climate change? How can we improve our understanding of moist convection and thereby improve climate models by studying the MJO? In this thesis, we will address these fundamental questions by analyzing observational datasets, constructing a hierarchy of numerical models, and developing quantitative theories.

In Chapter 2, we test the hypothesis that if the MJO could be a wave packet of a particular type equatorial waves and travels with the group velocity of this type of waves. In Chapter 3, we successfully simulate the MJO with a 2D shallow water model, in which triggered convection is employed. Without tuning any parameters in our model, we can capture all the MJO basic features, including its slow eastward drift rate and large horizontal scale. This is the important fact, because no other model matches all observations at once even with free parameters (see Section 1.5). We further propose that the MJO is an envelope of high-frequency inertia-gravity waves, and its eastward propagation is due to Earth's differential rotation. In Chapter 4, we seek the minimum recipe of the MJO and construct a 1D  $\beta$ -plane model that captures the most fundamental features of the MJO. We then develop a scaling theory of the MJO, and this theory helps to make predictions of how the MJO would vary with climate change. The success of simulating the MJO by using simple models in Chapters 3 and 4 implies that triggered convection, an extreme form of departures from QE convection, is important in simulating the MJO. In Chapter 5, we implement triggered convection in a 3D GCM by raising the convection threshold and robust MJO signals have been observed in our simulations. The major findings in this thesis put many MJO-related observations and recent modeling progress in a coherent picture. Given its success in explaining all the observed MJO features and predicting its behavior in climate change, this thesis challenges previous theoretical paradigms of the MJO dynamics. In Chapter 6, we conclude and discuss remaining questions.

## References:

Andersen, J. A., and Z. Kuang, 2012: Moist Static Energy Budget of MJO-like Disturbances in the Atmosphere of a Zonally Symmetric Aquaplanet. *J. Climate*, **25**, 2782-2804.

Arakawa, A., and W. H. Schubert, 1974: Interaction of a Cumulus Cloud Ensemble with Large-Scale Environment, Part I. *J. Atmos. Sci.*, **31**, 674-701.

Arnold, N. P., Z. Kuang, and E. Tziperman, 2013: Enhanced MJO-like Variability at High SST. *J. Climate*, **26**, 988-1001.

Bechtold, P., and Coauthors, 2008: Advances in simulating atmospheric variability with the ECMWF model: From synoptic to decadal time-scales. *Q. J. Roy. Meteor. Soc.*, **134**, 1337-1351.

Benedict, J. J., and D. A. Randall, 2009: Structure of the Madden–Julian Oscillation in the Superparameterized CAM. *J. Atmos. Sci.*, **66**, 3277-3296.

Caballero, R., and M. Huber, 2010: Spontaneous transition to superrotation in warm climates simulated by CAM3. *Geophys. Res. Lett.*, **37**, L11701.

Chen, S. S., R. A. Houze, and B. E. Mapes, 1996: Multiscale variability of deep convection in relation to large-scale circulation in TOGA COARE. *J. Atmos. Sci.*, **53**, 1380-1409.

Emanuel, K. A., J. D. Neelin, and C. S. Bretherton, 1994: On Large-Scale Circulations in Convecting Atmospheres. *Q. J. Roy. Meteor. Soc.*, **120**, 1111-1143.

Gill, A. E., 1980: Some Simple Solutions for Heat-induced Tropical Circulation. *Quart.*

*J. R. Met. Soc.*, **106**, 447-462.

Grabowski, W. W., 2001: Coupling cloud processes with the large-scale dynamics using the Cloud-Resolving Convection Parameterization (CRCP). *J. Atmos. Sci.*, **58**, 978-997.

———, 2002: Large-scale organization of moist convection in idealized aquaplanet simulations. *Int. J. Numer. Meth. Fl.*, **39**, 843-853.

———, 2003: MJO-like coherent structures: Sensitivity simulations using the cloud-resolving convection parameterization (CRCP). *J. Atmos. Sci.*, **60**, 847-864.

———, 2004: An improved framework for superparameterization. *J Atmos Sci*, **61**, 1940-1952.

Hendon, H. H., and B. Liebmann, 1994: Organization of Convection within the Madden-Julian Oscillation. *J. Geophys. Res.-Atmos.*, **99**, 8073-8083.

Hendon, H. H., and M. L. Salby, 1994: The Life-Cycle of the Madden-Julian Oscillation. *J. Atmos. Sci.*, **51**, 2225-2237.

Holloway, C. E., S. J. Woolnough, and G. M. S. Lister, 2013: The Effects of Explicit versus Parameterized Convection on the MJO in a Large-Domain High-Resolution Tropical Case Study. Part I: Characterization of Large-Scale Organization and Propagation. *J. Atmos. Sci.*, **70**, 1342-1369.

Hung, M. P., J. L. Lin, W. Q. Wang, D. Kim, T. Shinoda, and S. J. Weaver, 2013: MJO and Convectively Coupled Equatorial Waves Simulated by CMIP5 Climate Models. *J. Climate*, **26**, 6185-6214.

Khouider, B., Y. Han, A. J. Majda, and S. N. Stechmann, 2012: Multiscale Waves in an MJO Background and Convective Momentum Transport Feedback. *J. Atmos. Sci.*, **69**, 915-933.

Khouider, B., A. St-Cyr, A. J. Majda, and J. Tribbia, 2011: The MJO and Convectively Coupled Waves in a Coarse-Resolution GCM with a Simple Multicloud Parameterization. *J. Atmos. Sci.*, **68**, 240-264.

Kiladis, G. N., K. H. Straub, and P. T. Haertel, 2005: Zonal and vertical structure of the Madden-Julian oscillation. *J. Atmos. Sci.*, **62**, 2790-2809.

Kiladis, G. N., M. C. Wheeler, P. T. Haertel, K. H. Straub, and P. E. Roundy, 2009: Convectively coupled equatorial waves. *Rev. Geophys.*, **47**.

Lin, J. L., and Coauthors, 2006: Tropical intraseasonal variability in 14 IPCC AR4 climate models. Part I: Convective signals. *J. Climate*, **19**, 2665-2690.

Madden, R. A., and P. R. Julian, 1972: Description of Global-Scale Circulation Cells in Tropics with a 40-50 Day Period. *J. Atmos. Sci.*, **29**, 1109-1123.

Majda, A. J., and S. N. Stechmann, 2009: A Simple Dynamical Model with Features of Convective Momentum Transport. *J. Atmos. Sci.*, **66**, 373-392.

Maloney, E. D., 2009: The Moist Static Energy Budget of a Composite Tropical Intraseasonal Oscillation in a Climate Model. *J. Climate*, **22**, 711-729.

Maloney, E. D., and D. L. Hartmann, 2000: Modulation of hurricane activity in the Gulf of Mexico by the Madden-Julian oscillation. *Science*, **287**, 2002-2004.

Maloney, E. D., A. H. Sobel, and W. M. Hannah, 2010: Intraseasonal variability in an aquaplanet general circulation model. *J. Adv. Model. Earth Syst.*, **2**.

———, 2010: Intraseasonal variability in an aquaplanet general circulation model. *J. Adv. Model. Earth Syst.*, **2**.

Matsuno, T., 1966: Quasi-Geostrophic Motions in the Equatorial Area. *J. Meteorol. Soc. Jpn.*, **44**, 25-43.

Nakazawa, T., 1988: Tropical Super Clusters within Intraseasonal Variations over the Western Pacific. *J. Meteorol. Soc. Jpn.*, **66**, 823-839.

Pritchard, M., and D. Yang, 2014: Sensitivity of the superparameterized Madden-Julian Oscillation to extreme climate variation on a uniform temperature aquaplanet. *WWOSC, August 2014 at Montreal, Canada*, Abstract 56348.

Randall, D., M. Khairoutdinov, A. Arakawa, and W. Grabowski, 2003: Breaking the cloud parameterization deadlock. *Bull. Amer. Meteor. Soc.*, **84**, 1547-1564.

Raymond, D. J., and Z. Fuchs, 2007: Convectively coupled gravity and moisture modes in a simple atmospheric model. *Tellus*, **59A**, 627-640.

Raymond, D. J., and Ž. Fuchs, 2009: Moisture Modes and the Madden–Julian Oscillation. *J. Climate*, **22**, 3031-3046.

Seiki, A., and Y. N. Takayabu, 2007: Westerly wind bursts and their relationship with intraseasonal variations and ENSO. Part I: Statistics. *Mon. Wea. Rev.*, **135**, 3325-3345.

Sobel, A., and E. Maloney, 2012: An Idealized Semi-Empirical Framework for Modeling the Madden–Julian Oscillation. *J. Atmos. Sci.*, **69**, 1691-1705.

———, 2013: Moisture Modes and the Eastward Propagation of the MJO. *J. Atmos. Sci.*, **70**, 187-192.

Sobel, A. H., E. D. Maloney, G. Bellon, and D. M. Frierson, 2008: The role of surface heat fluxes in tropical intraseasonal oscillations. *Nat. Geosci.*, **1**, 653-657.

Straub, K. H., and G. N. Kiladis, 2003: Interactions between the boreal summer intraseasonal oscillation and higher-frequency tropical wave activity. *Mon. Wea. Rev.*, **131**, 945-960.

Wheeler, M., and G. N. Kiladis, 1999: Convectively coupled equatorial waves: Analysis of clouds and temperature in the wavenumber-frequency domain. *J. Atmos. Sci.*, **56**, 374-399.

Xu, K. M., and K. A. Emanuel, 1989: Is the Tropical Atmosphere Conditionally Unstable. *Mon. Wea. Rev.*, **117**, 1471-1479.

Yanai, M., B. Chen, and W. W. Tung, 2000: The Madden-Julian oscillation observed during the TOGA COARE IOP: Global view. *J. Atmos. Sci.*, **57**, 2374-2396.

Yang, D., and M. Pritchard, 2014: Testing the Yang and Ingersoll dynamical paradigm of the MJO. *WWOSC, August 2014 at Montreal, Canada*, Abstract 55630.

Yasunaga, K., and B. Mapes, 2012: Differences between More Divergent and More Rotational Types of Convectively Coupled Equatorial Waves. Part I: Space-Time Spectral Analyses. *J. Atmos. Sci.*, **69**, 3-16.

———, 2012: Differences between More Divergent and More Rotational Types of Convectively Coupled Equatorial Waves. Part II: Composite Analysis based on Space-Time Filtering. *J. Atmos. Sci.*, **69**, 17-34.

Zhang, C., 2005: Madden-Julian Oscillation. *Rev. Geophys.*, **43**.

Zhang, C. D., 2013: Madden-Julian Oscillation Bridging Weather and Climate. *Bull. Amer. Meteor. Soc.*, **94**, 1849-1870.



## Chapter 2

# Testing the Hypothesis that the MJO Is an MRG Wave Packet\*

### 2.1 Abstract

The Madden-Julian oscillation (MJO), a.k.a. the intraseasonal oscillation (ISO), is a planetary scale mode of variation in the tropical Indian and western Pacific Oceans. Basic questions about the MJO are why it propagates eastward at  $\sim 5 \text{ m s}^{-1}$ , why it lasts for intraseasonal timescales, and how it interacts with the fine structure that is embedded in it. This study will test the hypothesis that the MJO is not a wave, but a wave packet—the interference pattern produced by a narrow frequency band of mixed Rossby-gravity (MRG) waves. As such, the MJO would propagate with the MRG group velocity, which is eastward at  $\sim 5 \text{ m s}^{-1}$ . Simulation with a 3D model shows that MRG waves can be forced independently by relatively short-lived, eastward- and westward-moving disturbances, and the MRG wave packet can last long enough to form the intraseasonal variability. This

---

\* Appeared as: Yang, Da, Andrew P. Ingersoll, 2011: Testing the Hypothesis that the MJO is a Mixed Rossby–Gravity Wave Packet. *J. Atmos. Sci.*, **68**, 226–239.

hypothesis is consistent with the view that the MJO is episodic, with an irregular time interval between events rather than a periodic oscillation. The packet is defined as the horizontally smoothed variance of the MRG wave – the rectified MRG wave, which has features in common with the MJO. Our two-dimensional Fourier analysis of the NOAA outgoing longwave radiation (OLR) dataset indicates that there is a statistically significant correlation between the MJO amplitude and wave packets of MRG waves but not equatorial Rossby waves or Kelvin waves, which are derived from the Matsuno shallow water theory. However, the biggest absolute value of the correlation coefficient is only 0.21, indicating that the wave packet hypothesis explains only a small fraction of the variance of the MJO in the OLR data.

## **2.2 Introduction**

The Madden-Julian Oscillation (MJO) is the dominant intraseasonal variability in the tropical atmosphere. It is a planetary scale, slowly eastward propagating (about  $5 \text{ m s}^{-1}$ ) perturbation of both dynamical and thermodynamical fields. During an MJO event, a positive convection and rainfall anomaly develops in the western Indian Ocean and propagates to the western Pacific Ocean. Once the perturbation reaches the date line, the perturbation is largely confined to dynamical fields. The associated planetary-scale wind structure is baroclinic, and is characterized by low level convergence and upper level divergence (Madden and Julian 1972, 1994; Hendon and Salby 1994). More details can be found in recent and comprehensive reviews, such as Madden and Julian (2005), and Zhang (2005). In addition, within the MJO envelope, there are both westward and eastward moving fine scale structures (Nakazawa 1988; Hendon and Liebmann 1994).

The significance of the MJO for phenomena such as monsoon onset, ENSO, and rainfall patterns in the Tropics has been well established (Lau and Waliser 2005; Zhang 2005). However, a successful MJO theory, which accounts for all of the above features, is elusive. General circulation models (GCMs) simulate tropical intraseasonal variability with varying degrees of fidelity. Intercomparison studies (Lin et al. 2006; Zhang et al. 2006) show that most GCMs underestimate the variance associated with the MJO. Because of the complexity of GCMs, simple models can provide suggestions for improvement of GCM simulations of the MJO.

Emanuel (1987) and Neelin et al. (1987) proposed that the MJO arises from wind-induced surface heat exchange (WISHE), or wind-evaporation feedback. Sobel et al. (2010) and Maloney et al. (2010) provide further evidence to support the significance of the surface heat flux on the MJO. Although referred as an oscillation, the MJO is episodic rather than periodic (Salby and Hendon, 1994; Hartmann and Hendon, 2007). Therefore, instead of an instability mechanism, it is possible that it is irregularly forced. Motivated by Gill (1980), Chao (1987) interpreted the MJO as an atmospheric response to a large-scale eastward-moving heat source. Wang and Rui (1990) suggested that frictional moisture convergence couples the equatorial Kelvin and Rossby waves through organized convective heating, and selects a slowly eastward moving, planetary-scale unstable mode. The boundary-layer convergence leading the convective center is the key to this theory, and it has been confirmed by observations (Wang 2005; Zhang 2005). Raymond (2001) emphasizes the cloud-radiative feedback mechanism, which points to cloud parameterization for possible

improvements of the GCMs.

Majda and Biello (2004) and Biello and Majda (2005) focus on the observed multiscale nature of the MJO. In their model, fluxes of kinetic energy and heat arise at synoptic scales and form a planetary scale convective envelope that forces the MJO. Majda and Stechmann (2009) show how planetary scale moisture and heating anomalies interact with synoptic scale wave activity, and they derive a frequency that matches that of the MJO when realistic values of parameters are used.

Also focusing on the multiscale structure, Zou and Cho (2000) investigated the idea that the MJO is a wave packet. They reduced the problem to the one-dimensional nonlinear Schrödinger equation and concluded that the MJO is the result of eastward propagation of a group of mixed Rossby-gravity (MRG) waves or Rossby waves. They did not provide an observational test of this hypothesis.

Wheeler and Kiladis (1999) (hereinafter WK99) pointed out that the MRG group velocity is  $\sim 5 \text{ m s}^{-1}$ . Straub and Kiladis (2003) pursued the wave packet idea further and noted that the group velocity of MRG waves matches the speed of the MJO. They performed a statistical test using OLR data and concluded that the MRG variance is correlated with the MJO signal. The correlation is not large, although it is statistically significant, and the paper does not figure prominently in later review articles (e.g., Kiladis et al. 2009). Solodoch et al. (2010, in this issue) have suggested concurrently with the work reported here that equatorial winds due MRG wave packets (a.k.a. Yanai waves) lead to convective

heating via a nonlinear wind induced surface heat exchange (WISHE) feedback. In their model, this heating forces Kelvin waves with characteristics similar to those of the observed MJO.

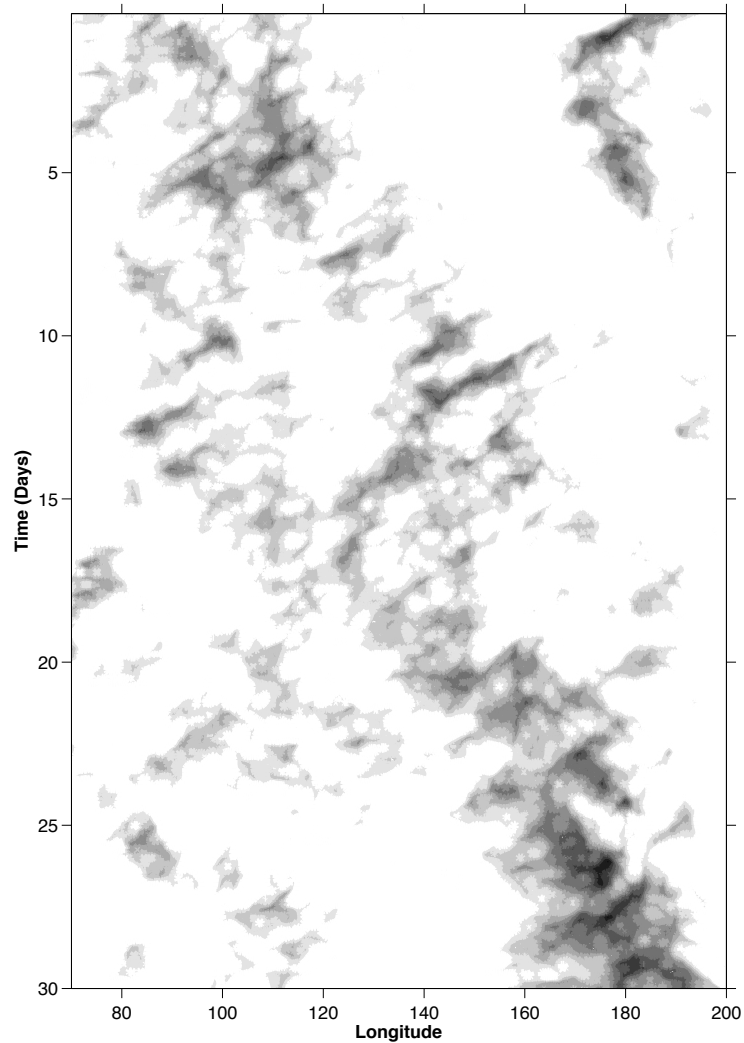


**Figure 2.1.** Longitude-time diagrams of the brightness temperature over  $0^{\circ} - 10^{\circ}\text{S}$  for 2 – 31 December 1992, during which an MJO event propagated through the eastern Indian and western Pacific oceans (the same time interval as in Fig. 11 of Chen et al. 1996). Dark represents low brightness temperature, which means high clouds; white represents high brightness temperature.

Figure 2.1 shows brightness temperature over the Indian and western Pacific oceans for a typical MJO event. Low brightness temperature represents deep convection. The convective center of the MJO propagates to the east at a speed of  $\sim 5 \text{ m s}^{-1}$  and lasts from Day 1 to Day 30. Besides the eastward moving MJO envelope, the  $11 \text{ m s}^{-1}$  westward propagating fine structure is prominent as well. The apparent eastward propagation of the large-scale convective center of the MJO is due to consecutive development of new convective systems, each to the east of the previous one. This behavior resembles that of a dispersive wave in which the phase speed is westward and the group velocity is eastward. In this study, we will further test the hypothesis that the MJO is a packet of MRG waves and that it propagates with the MRG group velocity, which is eastward at  $5 \text{ m s}^{-1}$ . The MRG wave packets share important features of the MJO, including its large- and small-scale space-time structure and its propagation behavior, but this hypothesis does not fully pass the observational test that we describe below.

In section 2 we carry out numerical simulations with an idealized three-dimensional GCM. We interpret the GCM results using the linear equatorial waves derived by Matsuno (1966) from the shallow water equations on an equatorial beta plane. These waves are classified into different wave types including Kelvin, equatorial Rossby (ER), westward and eastward inertio-gravity (WIG and EIG), and mixed Rossby-gravity (MRG) waves. In section 3 we use the filtering technique developed by WK99 to analyze the OLR observations from the National Oceanic and Atmospheric Administration (NOAA), focusing on the relation between MRG waves and the MJO. In section 4 we discuss the results of sections 2 and 3, and we present our conclusions and ideas for future work.

## 2.3 Theory and Modeling

Matsuno (1966) theory applies to small-amplitude surface waves in two dimensions on the equator of a rotating planet. The assumption of a basic state of rest is implicit. The theory can be applied to small-amplitude waves in three dimensions by treating each vertical normal mode separately. There are two parameters in the Matsuno theory, the planetary vorticity gradient  $\beta$  and the gravity wave  $c$ . Each normal mode has a different value of  $c$ . The value of  $c$  depends on the mode number, the scale height of the atmosphere, whether it is weakly or strongly stratified, and whether it is moist or dry. There are theories on how to relate the dry dynamics to the moist dynamics, although exactly why moist waves have the same dispersion pattern as the dry waves, but with different values of  $c$ , remains a mystery (Kiladis et al. 2009). WK99 have shown that there is a particular range of  $c$  values for which a close correspondence exists between wavenumber-frequency spectral peaks of the OLR data and the dispersion relations of the linear equatorial waves. The  $c$  values are usually expressed in terms of equivalent depth  $h = c^2/g$ , where  $g$  is the gravitational acceleration.

Figure 2.2a shows equatorial wave dispersion curves for  $h = 25$  m ( $c = 15.7$  m s<sup>-1</sup>), which is a typical value from the WK99 analysis. For a point on one of the curves, the slope of the line to the origin gives the phase speed, and the slope of the tangent to the curve gives the group velocity. Positive slope (upward to the right) means eastward propagation. Figure 2.2b shows the group velocities of equatorial waves with the same equivalent depth as Fig. 2.2a, all as functions of their longitudinal wavelengths. The Kelvin wave phase speed and group velocity are both equal to  $c$ , and are too fast to match the MJO. The MRG group

velocity is consistent with the MJO propagation speed within a wide zonal wavenumber range. The ER, WIG and EIG waves have positive group velocity for part of the zonal wavenumber range, but the ER group velocity seems too slow to match the MJO propagation speed. Of all these waves, the MRG group velocity has the best match to the MJO.

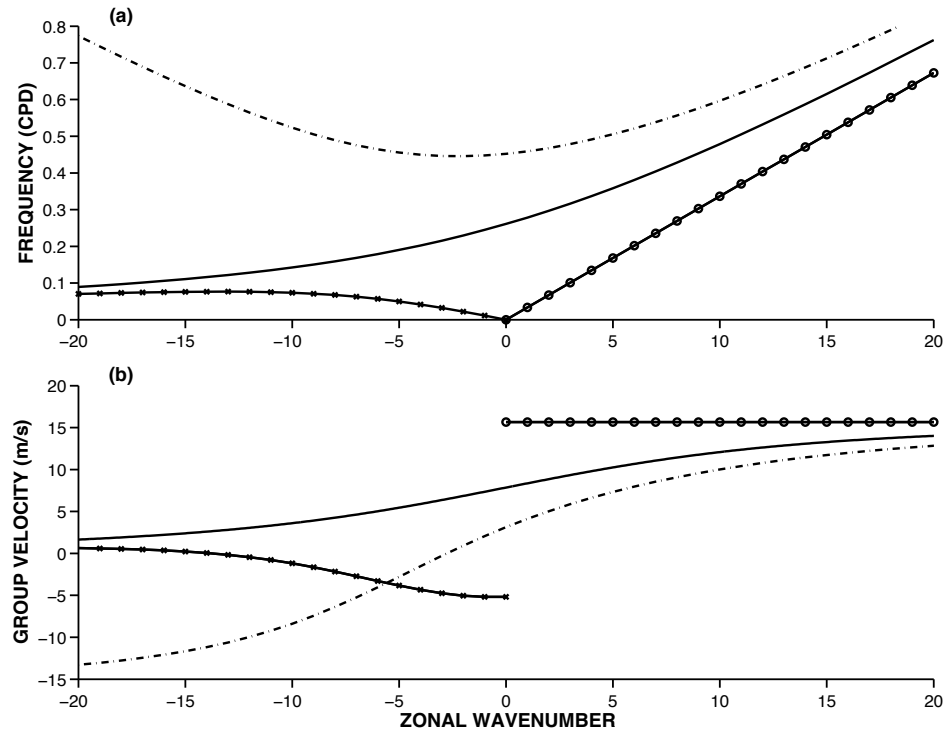


**Figure 2.2.** (a) WIG and EIG waves (dot-dashed), MRG waves (solid), equatorial Rossby (ER) waves (marked with x), and Kelvin waves (marked with o). (b) The corresponding group velocities. All the curves are for equivalent depth = 25 m. The Kelvin wave phase speed and group velocity are both equal to  $c = 15.7 \text{ m s}^{-1}$ .

In our first test of the wave packet hypothesis, we use an idealized general circulation model (GCM) to simulate the equatorial waves. The GCM is based on the spectral dynamical core of the Geophysical Fluid Dynamics Laboratory's Flexible Modeling

System. The horizontal resolution is T42 and there are 26 unevenly spaced sigma levels. This is a dry model, but we have reduced the effective static stability by increasing the specific heat. With this change, the first baroclinic mode – the one that spans the troposphere from top to bottom – matches the phase speed  $c \approx 15.7 \text{ m s}^{-1}$  of the observed convectively coupled waves. A more realistic GCM must match the phase speed by correctly simulating the interaction of waves with moist convection. This is an important requirement for any GCM if the interaction with convectively coupled waves turns out to be an important element of the MJO.

The two types of dissipation in our GCM are a linear damping of velocities in the boundary layer (Held and Suarez 1994) and a sponge layer in the stratosphere (Eq. 2.1):

$$\begin{aligned} \frac{\partial v}{\partial t} &= \dots - k_v(\sigma)v; \\ k_v &= k_f \left[ \max\left(0, \frac{\sigma_s - \sigma}{\sigma_s}\right) + \max\left(0, \frac{\sigma - \sigma_b}{1 - \sigma_b}\right) \right]; \\ \sigma_s &= 0.1; \quad \sigma_b = 0.7; \\ k_f &= 1 \text{ day}^{-1}. \end{aligned} \tag{2.1}$$

Here  $v$  is the vector velocity,  $t$  is time,  $\sigma$  is  $p/p_{\text{surf}}$ , and  $p_{\text{surf}}$  is the surface pressure.  $\sigma_b$  is the top of the boundary layer and  $\sigma_s$  is the base of the sponge layer. Temperatures are relaxed to the equilibrium temperature field (Held and Suarez 1994), but the equilibrium temperature is a function of altitude only. Simulations are carried out over an aqua planet. Each simulation is initiated by a heat source (Eq. 2.2) moving at speed  $c_s$  ( $c_s > 0$  is eastward;  $c_s < 0$  is westward).  $Q$  represents the heating. Also,  $x$ ,  $y$ , and  $\sigma$  are zonal, meridional and vertical coordinates, and  $x_0$  and  $t_0$  are the initial zonal and temporal

positions.

$$\begin{aligned}
 Q &\sim Q_t Q_h Q_\sigma; \\
 Q_t &= 1 - \frac{(t - t_0/2)^2}{(t_0/2)^2}, \quad 0 \leq t \leq t_0; \\
 Q_h &= y \left( 1 - \frac{(x - x_0 - c_s t)^2 + y^2}{r^2} \right), \quad (x - x_0 - c_s t)^2 + y^2 < r^2; \\
 Q_\sigma &= \cos\left(\frac{\pi}{2} \frac{\sigma - \sigma_0}{1 - \sigma_0}\right), \quad \sigma_s \leq \sigma \leq 1.
 \end{aligned} \tag{2.2}$$

The forcing (Eq. 2.2) increases from zero to a maximum and then decreases to zero again during a time interval  $t_0$ . It has an imposed horizontal scale  $r \sim 3000$  km. The heating profile has its maximum at the middle troposphere ( $\sigma_0 = 0.55$ ) and is zero at the ground ( $\sigma = 1$ ) and the base of the stratosphere ( $\sigma = \sigma_s = 0.1$ ). The forcing is near the equator and can be either symmetric or antisymmetric about it.

Examples are shown in Fig. 2.3. Although these are 3D simulations on a sphere, we interpret the results using the Matsuno (1966) theory of 2D waves trapped at the equator (Fig. 2.2). Figure 2.3a shows the waves excited by an antisymmetric forcing that increases from 0 to the maximum and decreases to 0 again over a 20-day period and moves westward at  $9 \text{ m s}^{-1}$ . The waves whose phase speed matches that of the forcing are resonantly excited – they remain in phase with the forcing – and in Fig. 2.3a these are the westward-moving MRG waves (Fig. 2.2). The bandwidth in frequency is inversely proportional to the duration of the forcing. The wave's group velocity is  $\sim 4 \text{ m s}^{-1}$  to the east. Despite having the same damping rates ( $1 \text{ day}^{-1}$  in the boundary layer and no sponge layer) as those used in idealized climate modeling (Held and Suarez 1994), the MRG wave packet maintains its identity for longer than 30 days. Moreover, the wave packet is a planetary scale feature.

Because the spectrum analysis shows the scales of waves only, the scale of the wave packet cannot be seen on the wavenumber-frequency spectrum. Such time-space structure and propagation speed are the same as for the MJO events. We also experimented with a sponge layer (Eq. 2.1). This is to prevent energy from being reflected back from the upper boundary. With or without the sponge layer, the wave packet still lasts longer than 30 days. Figure 2.3b shows another simulation with the same forcing but without the boundary layer damping. The intense contours maintain longer than 40 days.

The simulation shown in Fig. 2.3c is forced with a 10-day storm moving westward at  $9 \text{ m s}^{-1}$ . Because the forcing lasts for a shorter length of time than in the previous simulations, the excited waves are not purely MRG waves. However, the dominant feature is still the MRG wave packet, which moves to east at  $\sim 4 \text{ m s}^{-1}$ . In Fig. 2.3d, the waves are excited by a storm moving to the west at  $4 \text{ m s}^{-1}$ , which is slower than the speed in Figs. 2.3a – 2.3c. From Fig. 2.2a, we can see that if there is a heat source moving west at  $4 \text{ m s}^{-1}$ , both ER and MRG waves will be excited. Fig. 2.3d shows the mixture of ER and MRG waves. During day 1 to day 25, there is a dominant MRG wave packet between  $120^\circ$  and  $250^\circ$  E, which propagates to east at  $\sim 4.6 \text{ m s}^{-1}$ . Between day 25 and day 50, the dominant features are the westward drifting phase lines with a stationary wave packet. Both the phase speed and the group velocity are small, which suggests ER waves. The weak eastward propagating wave packet could be an MRG wave packet. These figures tell us that eastward and westward MRG waves can form wave packets that mimic the features of the MJO.

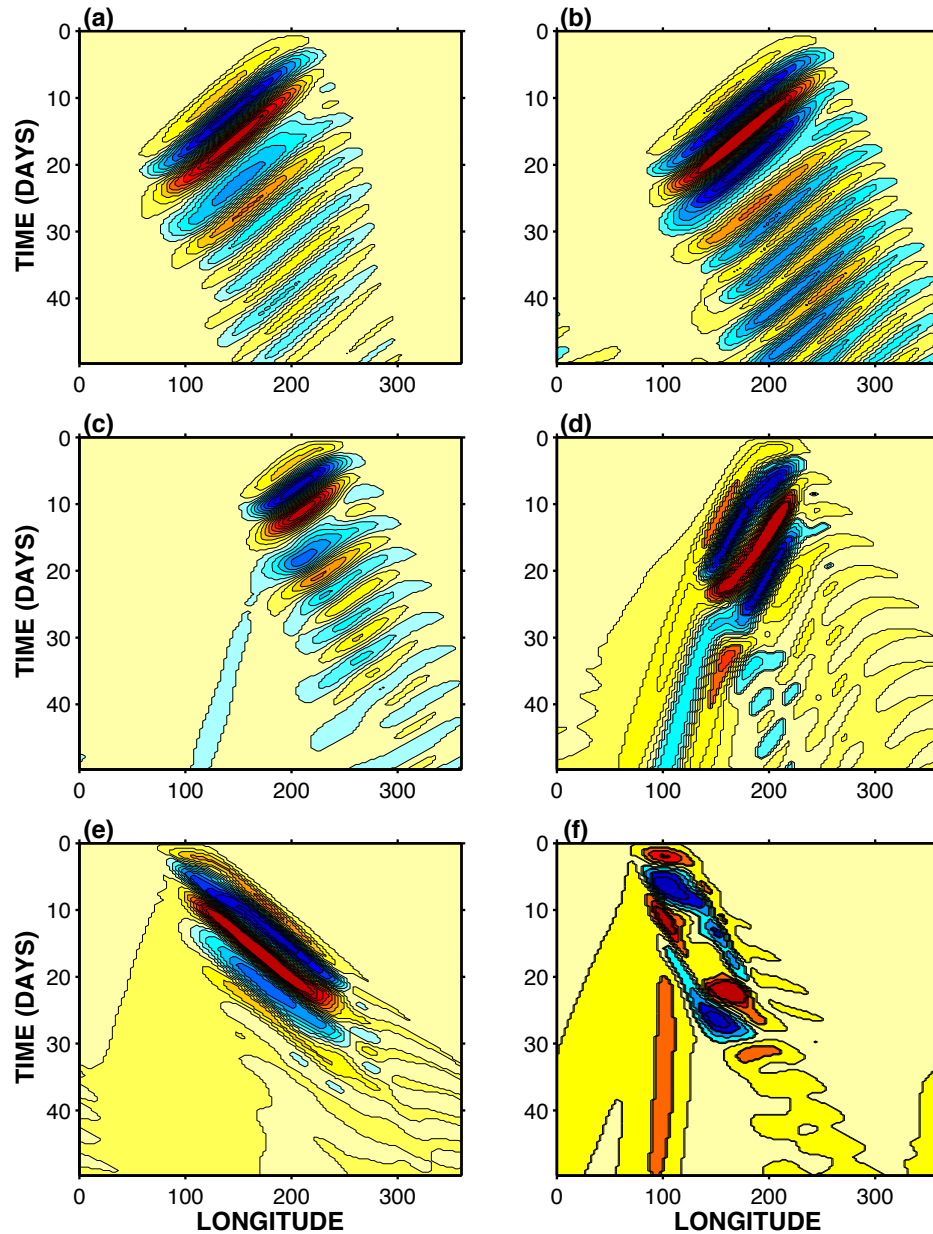


**Figure 2.3.** Longitude–time diagrams of the air temperature anomaly in the GCM at  $\sigma \approx 0.5$ . Temperature has been averaged from  $0^\circ\text{N}$  to  $4.2^\circ\text{N}$ . The blue represents a negative temperature anomaly, and the red is a positive anomaly. (a) Source moves west at  $9 \text{ m s}^{-1}$  and lasts for 20 days; boundary-layer damping is  $1 \text{ day}^{-1}$ . (b) Same as (a) except there is no boundary layer damping. (c) Same as (a) except source lasts for 10 days. (d) Same as (a) except source moves at  $4 \text{ m s}^{-1}$ . (e) Same as (a) except source moves east at  $9 \text{ m s}^{-1}$ . (f) Same as (e) except the source moves to the east at  $4 \text{ m s}^{-1}$  and there is no boundary layer damping.

Figure 2.3e shows a wave packet excited by the same forcing as that in Fig. 2.3a but moving to east at  $9 \text{ m s}^{-1}$ . From Fig. 2.2a, we can see that an eastward  $9 \text{ m s}^{-1}$  heating source cannot resonantly excite any of the eastward waves in the Matsuno diagram. Thus Fig. 2.3e shows a variety of linear responses, one of which might be an MRG wave. Figure 2.3f shows a simulation with an eastward forcing at  $4 \text{ m s}^{-1}$  over a 20-day period. As discussed above, the slow moving source will not resonantly excite any waves in the Matsuno diagram. Thus the response in Fig. 2.3f does not have the typical wave structure.

Figure 2.3 tells us that westward moving storms can excite MRG wave packets moving eastward at  $\sim 5 \text{ m s}^{-1}$ . Even eastward moving storms can excite MRG wave packets, as in Fig. 2.3e. The packet speed is relatively insensitive to the speed of the storm. The packets last longer than the storms, but the storms determine the interval between events. We have varied the meridional extent of the forcing, including forcings with an extent of  $\sim 1000 \text{ km}$ , which is about the equatorial wave-guide, *i.e.*, one Rossby deformation radius. The results are similar to those of Fig. 2.3. The MRG wave packets are not sensitive to the meridional extent of the forcing. If the MJO is composed of MRG waves, it could be an atmospheric response to an equatorial or extra-tropical forcing. This idea is consistent with the view that the MJO is episodic, with an irregular time interval between events rather than a periodic oscillation (Salby and Hendon, 1994; Hartmann and Hendon, 2007).

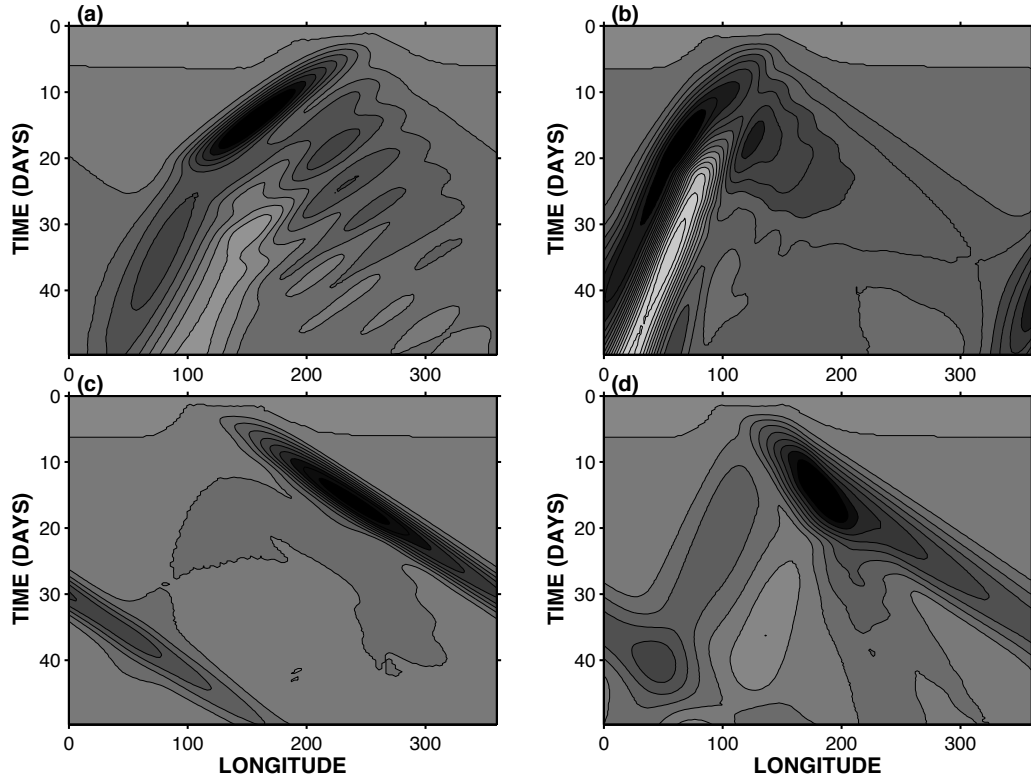


**Figure 2.4.** Time-longitude diagram of the air temperature anomaly in the GCM at  $\sigma \approx 0.5$ . Temperature has been averaged from  $4.2^\circ\text{N}$  to  $9.8^\circ\text{N}$ . Anomaly increases with the darkness of the color. The source is a dipole – a positive heating anomaly to the north and a negative anomaly to the south, which is the same as for Fig. 2.3a except the zero line has been displaced north from the equator to latitude  $5.6^\circ$ . (a) Source moving to the west at  $\sim 9 \text{ m s}^{-1}$ . (b) Source moving to the west at  $\sim 4 \text{ m s}^{-1}$ . (c) Source moving to the east at  $\sim 9 \text{ m s}^{-1}$ . (d) Source moving to the east at  $\sim 4 \text{ m s}^{-1}$ .

The forcings in Fig. 2.4 resemble those in Fig. 2.3a but are displaced northward by  $5.6^\circ$ . That is, the coordinate  $y$  in Eq. (2.2) is replaced by  $y - y_1$ , where  $y_1$  is the  $5.6^\circ$  latitude line. As in Fig. 2.3a, the forcing of Fig. 2.4a moves to the west at  $\sim 9 \text{ m s}^{-1}$ . Since the forcing is

neither symmetric nor antisymmetric about the equator, one would expect a linear combination of different meridional equatorial waves. There is a non-dispersive wave moving to the west at  $\sim 3.3 \text{ m s}^{-1}$  from day 25 to 50. It could be a low wavenumber ER wave. There is also an eastward propagating wave packet with a group velocity of  $\sim 7.5 \text{ m s}^{-1}$ . The phase lines of the packet move to the west at  $\sim 10 \text{ m s}^{-1}$ . This wave packet could be composed of MRG waves. Although the forcing is not strictly antisymmetric about the equator, an MRG wave packet has been excited. The forcing in Fig. 2.4b moves to the west at  $\sim 4 \text{ m s}^{-1}$ . There is a strong non-dispersive wave moving to the west at  $\sim 2.8 \text{ m s}^{-1}$ , which could be a low wavenumber ER wave. Another strong signal is a wave packet moving eastward at  $\sim 11.6 \text{ m s}^{-1}$ . Within the wave packet, there are westward moving phase lines, which is a signature of MRG waves. However, it is faster than the MJO propagation speed. The forcing in Fig. 2.4c moves eastward at  $\sim 9 \text{ m s}^{-1}$ . The most dominant feature is the non-dispersive wave, which propagates at  $\sim 11.1 \text{ m s}^{-1}$ . Considering this propagation speed and the non-dispersive feature, this could be a Kelvin wave. The forcing in Fig. 2.4d moves eastward at  $\sim 4 \text{ m s}^{-1}$ . The forcing excites both westward and eastward moving structures. The structure moving westward at  $\sim 3.8 \text{ m s}^{-1}$  could be the ER wave. The non-dispersive structure moving eastward at  $10.6 \text{ m s}^{-1}$  could be the Kelvin wave. There is another westward moving anomaly, which is weaker and moves at  $\sim 2 \text{ m s}^{-1}$ . Simulations in Fig. 2.4a-d do not excite pure MRG waves. In contrast, they excite mixtures of equatorial waves, because the forcing is neither symmetric nor antisymmetric about the equator and such forcing corresponds to a mixture of different meridional modes.

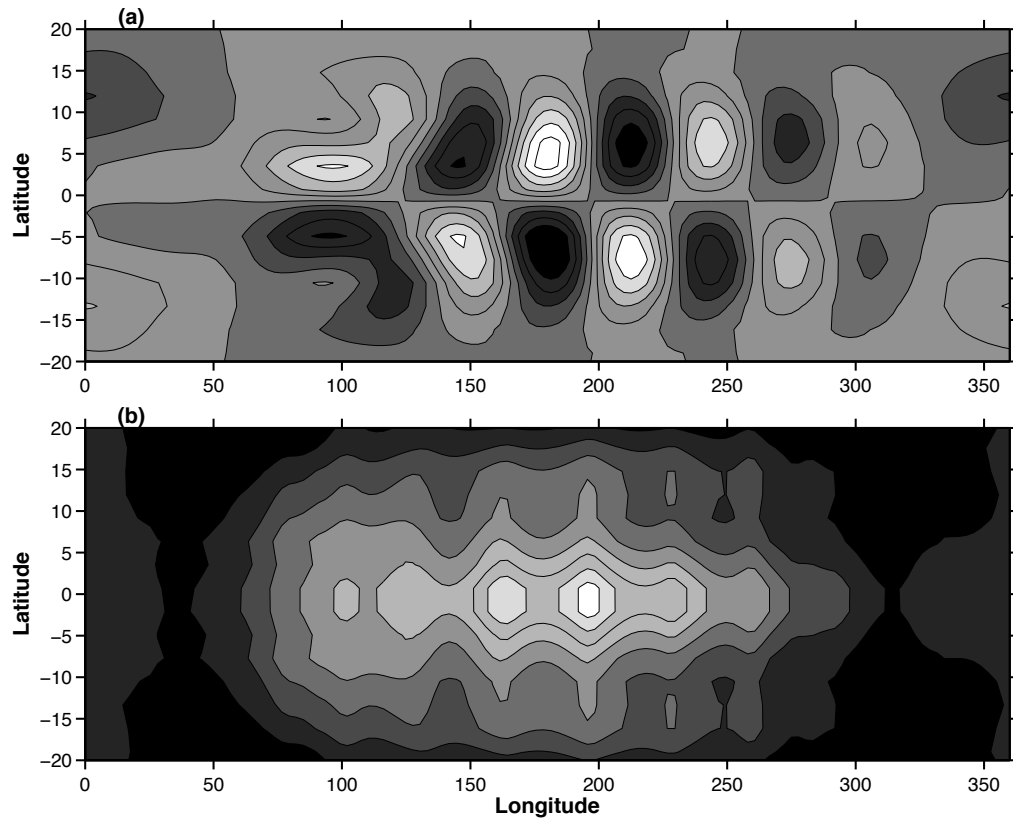


**Figure 2.5.** (a) Map view of the MRG divergence field at ~160mb. White represents positive divergence, and black represents negative divergence. Contour intervals are equal. (b) Map view of the rectified MRG divergence field. The white is high, the black is low, and the gray is in between.

Certain aspects of this hypothesis need further discussion. First, the MRG waves (Fig. 2.5a) are antisymmetric about the equator, but the MJO and the MRG wave packets are symmetric. To get the wave packet, we square the wave amplitude to get the variance and

then smooth the result over several spatial wavelengths. The packets are the rectified MRG waves (Fig. 2.5b). When we rectify the MRG waves, we use a 2-dimensional boxcar average over  $\sim 20^\circ$  in latitude and longitude. The hypothesis is that clouds will spread in the upper troposphere and form the rectified MRG waves. The rectified MRG waves are symmetric: They have a maximum at the equator and look strong only in the active MRG wave regions—where the original MRG wave signal varies periodically from a large negative anomaly to a large positive anomaly. The packets—the large-scale, rectified MRG waves—have a different structure than the individual crests and troughs. It is the rectified wave—the wave packet—that has some of the features of the MJO.

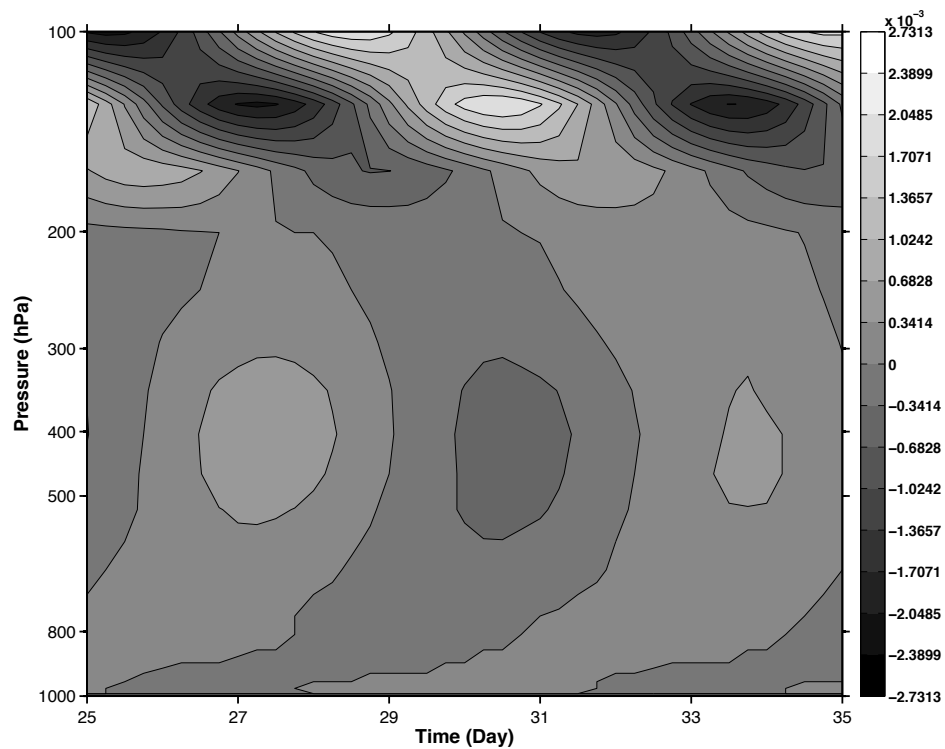


**Figure 2.6.** Pressure-time cross section of the temperature anomaly at  $5^\circ\text{N}$ ,  $220^\circ\text{E}$ .

Second, the model does not require a reduced vertical wavelength to get a slow propagation

speed. In fact, the vertical structure of the waves in these simulations is similar to the observations. Figure 2.6 shows the time-pressure cross section of the temperature anomalies of the simulated MRG waves. The first baroclinic mode is dominant—the temperature anomaly reaches the maximum in the mid-troposphere and decreases both toward the ground and toward the tropopause, but the second baroclinic mode is present. Since time increases to the right, the downward slope in the upper atmosphere indicates downward phase propagation or upward energy propagation, which is consistent with energy dissipation in the sponge layer. The opposite slope in the lower atmosphere is consistent with energy dissipation in the boundary layer. As a result, the temperature maximum in the boundary layer occurs at the same time as the temperature minimum at 400 hPa and vice versa, indicating the presence of the second baroclinic mode. The direction of slope in the upper and lower atmosphere agrees with observation (Kiladis et al. 2009), but the second baroclinic mode is stronger in the observations than in Fig. 2.6.

Third, De-Leon et al. (2010) showed that the MRG wave does not exist on a sphere if there are boundaries at mid-latitudes; instead, the first ER mode and the first westward inertio-gravity wave mode are separated by the anti-Kelvin wave for all values of the zonal wavenumber (the anti-Kelvin wave is a westward-propagating edge wave with maximum amplitude at the mid-latitude boundary). However, our 3D simulation is carried out on a sphere without mid-latitude boundaries, and the MRG waves still behave as predicted in the Matsuno theory. For these equivalent depths, the MRG waves are trapped within  $\sim 1000$  km of the equator, which is small compared to the pole-to-equator distance. As a result, the equatorial beta-plane without boundaries is a good approximation.

## 2.4 Data Analysis

The other test of the wave packet hypothesis uses once-daily estimates of outgoing longwave radiation (OLR) from the NOAA polar orbiting satellites (Liebmann and Smith 1996) extending from June 1974 to July 2009. Low brightness temperatures are taken to be areas of deep tropical convection and enhanced precipitation (WK99). The data from each scanning swath of the satellite are archived on a  $2.5^\circ$  grid allowing representation of high wavenumber features.

The method used for this part of the study is space-time spectral analysis as pioneered by WK99. Figures 2.7a and 2.7b show contours of the logarithm of the power in the antisymmetric and symmetric (about the equator) components of the OLR. Superimposed upon these two plots are the dispersion curves for linear equatorial waves with even and odd meridional mode number, for various equivalent depths and for a zero wind basic state. The equivalent depths of the two MRG dispersion curves (the solid and dashed red lines curving upward to the right) in Fig. 2.6a are 8 m and 250 m, respectively. The other dispersion curves (Kelvin = black, ER = blue) in Figs. 2.7a and 7b have equivalent depths of 8 m and 90 m, respectively. The equatorial waves are most active within these equivalent depth ranges (WK99). Most of the power is located at the low frequency and low wavenumber region. In this study, the MJO spectral power is defined in the white box to the right of the origin close to the horizontal axis. This is the power within the wavenumber range from 1 to 5 and the frequency domain from  $1/96$  to  $1/40$  cycles per day, and it appears in both Figs. 2.7a and 2.7b. Although the MJO signal is the strongest signal

in the wavenumber-frequency diagram, no linear equatorial wave in the Matsuno theory matches the MJO signal. Following WK99, we filter the signal by looking only at the Fourier coefficients in each of the boxes outlined in Fig. 2.7.

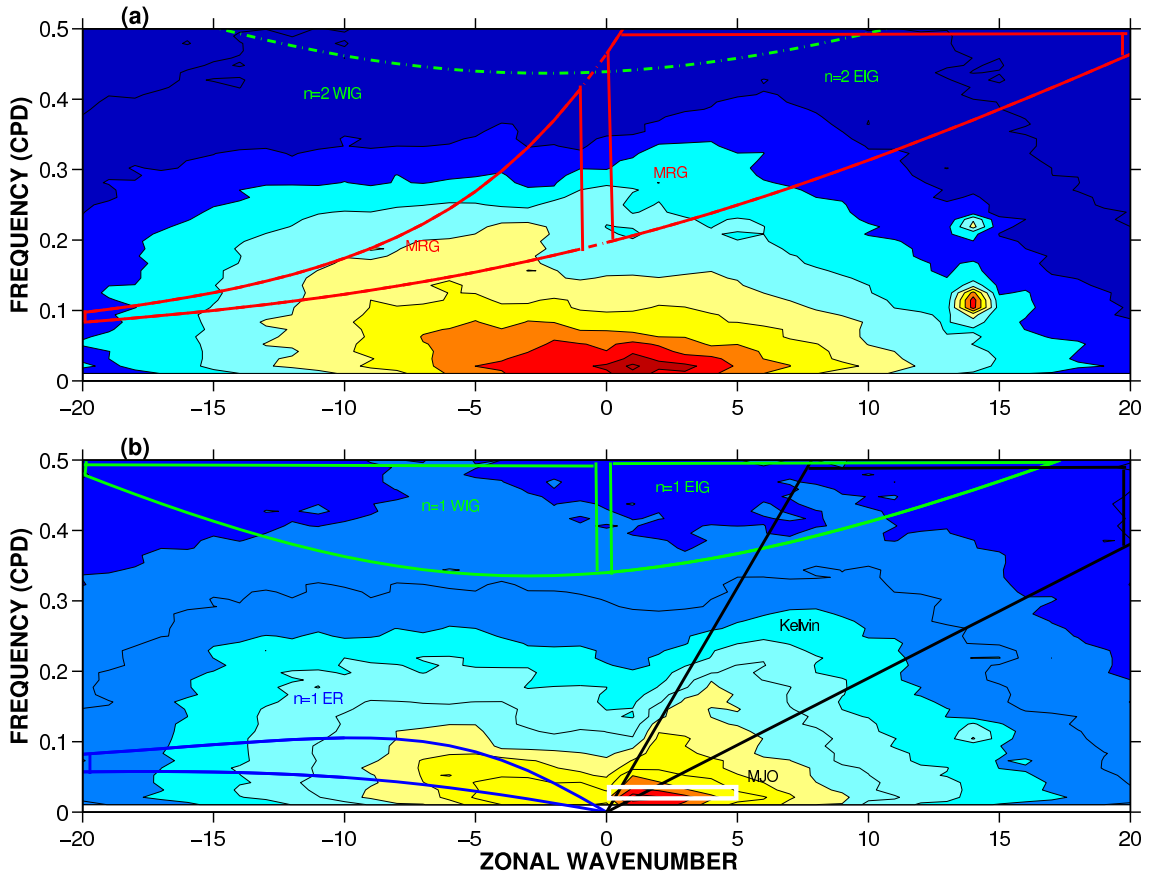


**Figure 2.7.** (a) Zonal wavenumber-frequency power spectra of the antisymmetric component of OLR, calculated for the entire period of record from 1974 to 2009. The superimposed green line is the inertio-gravity wave; the red lines are the MRG waves with equivalent depths of 8 and 250 m. (b) As in (a) but for the symmetric component. The green curve is the WIG and EIG wave; blue is the ER wave, and black is the Kelvin wave with equivalent depths of 8 and 90 m. Although not predicted by linear wave theory, the MJO is the power that is concentrated in the white box to the right of center and close to the horizontal axis. For all components, the power has been summed over  $10^{\circ}\text{S} - 10^{\circ}\text{N}$ . Solid boxes represent regions used in the wavenumber-frequency filtering.

In Fig. 2.8 we show a specially selected example that illustrates our method—a time-longitude section of a 40-day OLR field (Fig. 2.8a) at its full  $2.5^\circ$  longitude and once-daily time resolution. Not all 40-day sections are this illustrative. The OLR has been averaged over  $10^\circ\text{S}$ - $5^\circ\text{N}$ , which is the mean latitudinal position of Indian Ocean MJO events (CLIVAR 2009). There are three longitudinal centers of low OLR, which correspond to the three convectively active regions. Over the Indian and western Pacific Oceans, besides the slow eastward propagating convection systems, there are smaller scale disturbances moving to the west. These small disturbances could be the MRG waves (WK99). We first examine the convective signals that can be associated with the MJO. Figure 2.8b shows the same time-longitude section as Fig. 2.8a, but only for the Fourier coefficients in the MJO box. The negative OLR anomaly represents deep convection and therefore the active phase of the MJO. We see that the MJO involves slow progression ( $\sim 5 \text{ m s}^{-1}$ ) of convective activity from the Indian Ocean to the central Pacific, and it is dominated by zonal wavenumbers 2 and 3, which is a typical horizontal scale for the OLR signature of the MJO. In Fig. 2.8c, the MRG wave has a phase speed that varies between  $-10 \text{ m s}^{-1}$  and  $-15 \text{ m s}^{-1}$  and a positive group velocity of  $\sim 6 \text{ m s}^{-1}$ . Between day 5 and day 25, when the MJO is the strongest, there is an intense MRG wave packet traveling eastward from  $70^\circ$  to  $150^\circ$ . Figure 2.8d shows the rectified MRG wave, which captures the major characteristics of the MRG packets. Comparing Figs. 2.8b and 2.8d, we see that the MRG packet matches the MJO event. They have similar propagation speeds, and they occur at the same place during the same time. In addition, the MRG phase speed is similar to that of the small disturbances propagating within the MJO (shown in the raw OLR field, Fig. 2.8a).

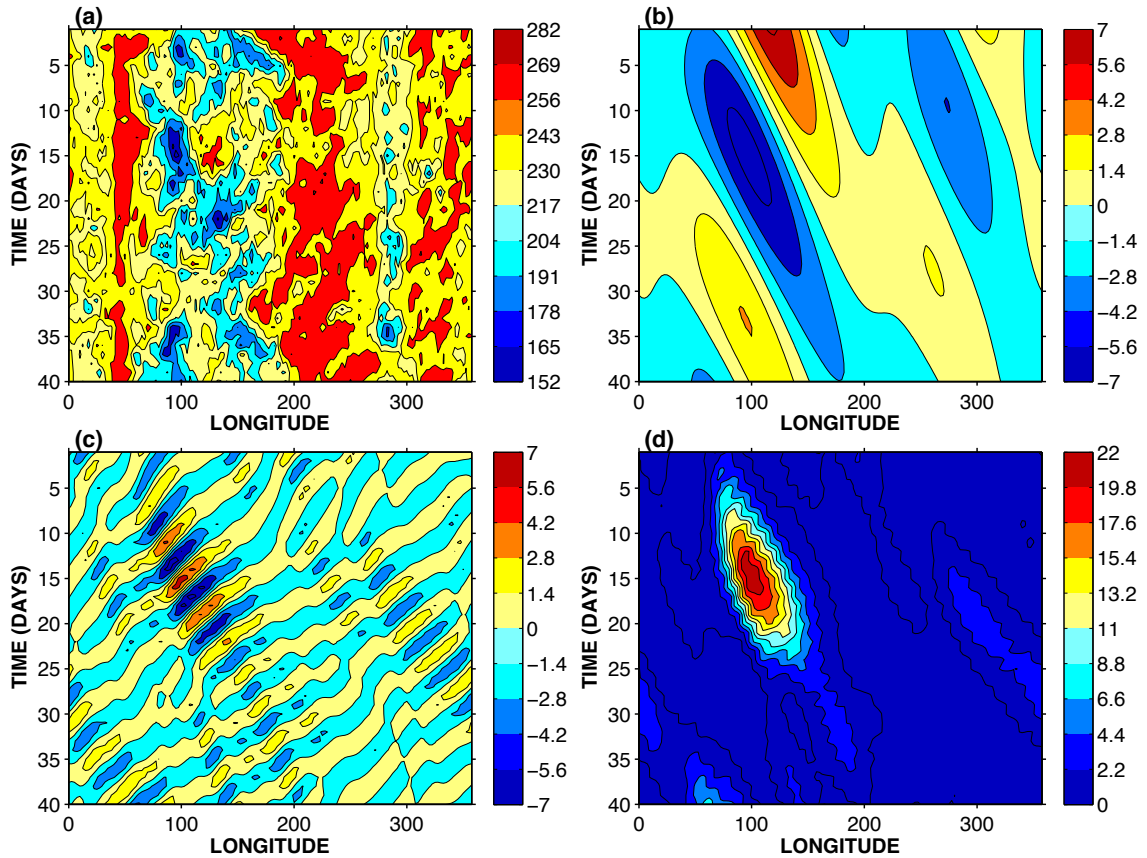


**Figure 2.8.** (a) The longitude-time diagrams of the OLR ( $\text{W m}^{-2}$ ) averaged for the latitudes from  $10^{\circ}\text{S}$  to  $5^{\circ}\text{N}$ . The record extends from July 11 to August 19, 1985. (b) Longitude-time section of OLR anomalies for the MJO-filtered band for the same 40-day period as in (a). (c) The MRG-filtered band for the same 40-day period. (d) The rectified MRG waves for the same 40-day period.

Figure 2.9\* shows the results of an analysis that uses the complete 1974-2009 OLR data to

---

\* **Figure 2.9.** The joint probability distribution (JPD) of the MJO with (a) the rectified westward MRG waves, (b) the rectified eastward MRG waves, (c) the rectified Kelvin waves and (d) the rectified EIG waves, (e) the rectified ER waves, (f) the rectified WIG waves. We filter using the Fourier coefficients within the boxes shown in Fig. 2.7. These coefficients were computed from the full global data set. After inverting the filtered

calculate the joint probability distribution (JPD) of the MJO and the rectified westward and eastward MRG, Kelvin, EIG and ER waves. From the raw data, we can filter the MJO signal and then project back into the longitude and time domain, as we did in Fig. 2.8b. The figure is for the Indian Ocean MJO, which is defined as the MJO anomaly within the Indian Ocean longitude band, 75°-100°E. The common feature of Fig. 2.9 is that the largest probability density is near the origin – at low tropical wave activity (rectified waves of each type) and  $MJO = 0 \text{ W m}^{-2}$ . The JPD decreases when the tropical wave activity and the absolute value of the MJO anomaly go up. Figures 2.9a and 2.9b show the JPD of the westward and eastward MRG waves with the MJO. Both distributions are tilted. That is, when the rectified MRG wave activity is high, there is more likely to be an active MJO phase—a negative MJO signal. The correlation coefficients between westward and eastward MRG waves and the MJO are -0.08 and -0.21, respectively. The correlation coefficients between the EIG, Kelvin, ER and WIG waves and the MJO (Figs. 2.9c, 2.9d, 2.9e and 2.9f) are -0.11, -0.001, -0.04 and -0.11, respectively. In order to test whether these correlations are significant, one needs an estimate of the degrees of freedom (DOF). By analogy with coin flips, if there are N tails in an average experiment, then there are 2N flips of the coin, or 2N DOF's. Our statistical test uses 35 years of data, and the average year has 9 MJO events. Within one MJO event, there is one active and one inactive phase.

---

coefficients to a time-longitude plot, we construct the JPD from the Indian Ocean section, 10°S-5°N, 75°-100°E. The contour intervals are the same for each figure, and the maximum and minimum values are also the same. The downward tilt to the right in 2.9a and 2.9b is evidence that the rectified MRG waves are correlated with low OLR in the MJO frequency band.

Accordingly, the DOF is  $35 \times 9 \times 2 = 630$ . With this DOF, no significant correlation exists between the Kelvin and ER waves and the MJO. However, there is a statistically significant relation between the MJO and both the westward and eastward MRG waves at the 95% significance level. Also both EIG and WIG waves are correlated with the MJO signal at the 95% significance level.

Figure 2.10 shows the results of another statistical analysis, which uses just the November – April OLR data and covers  $75^{\circ}$ - $185^{\circ}$ E range of longitudes. The distributions in Figs. 2.10c, d, e and f are not obviously tilted. Only the JPDs between the MJO and the rectified MRG waves (Fig. 2.10a and b) are tilted, but the correlation coefficients are only -0.07 and -0.1. The absolute values of correlation coefficients of other JPDs are even smaller. Compared to the analysis in Fig. 2.9, this analysis uses a longitude range that is larger by a factor of 4.4 and a temporal range that is smaller by a factor of 2. So the DOF is approximately 1386. With this DOF, there is a significant correlation only between the MJO and the MRG waves at the 95% significance level. No significant correlation exists between the IG, Kelvin and ER waves and the MJO.

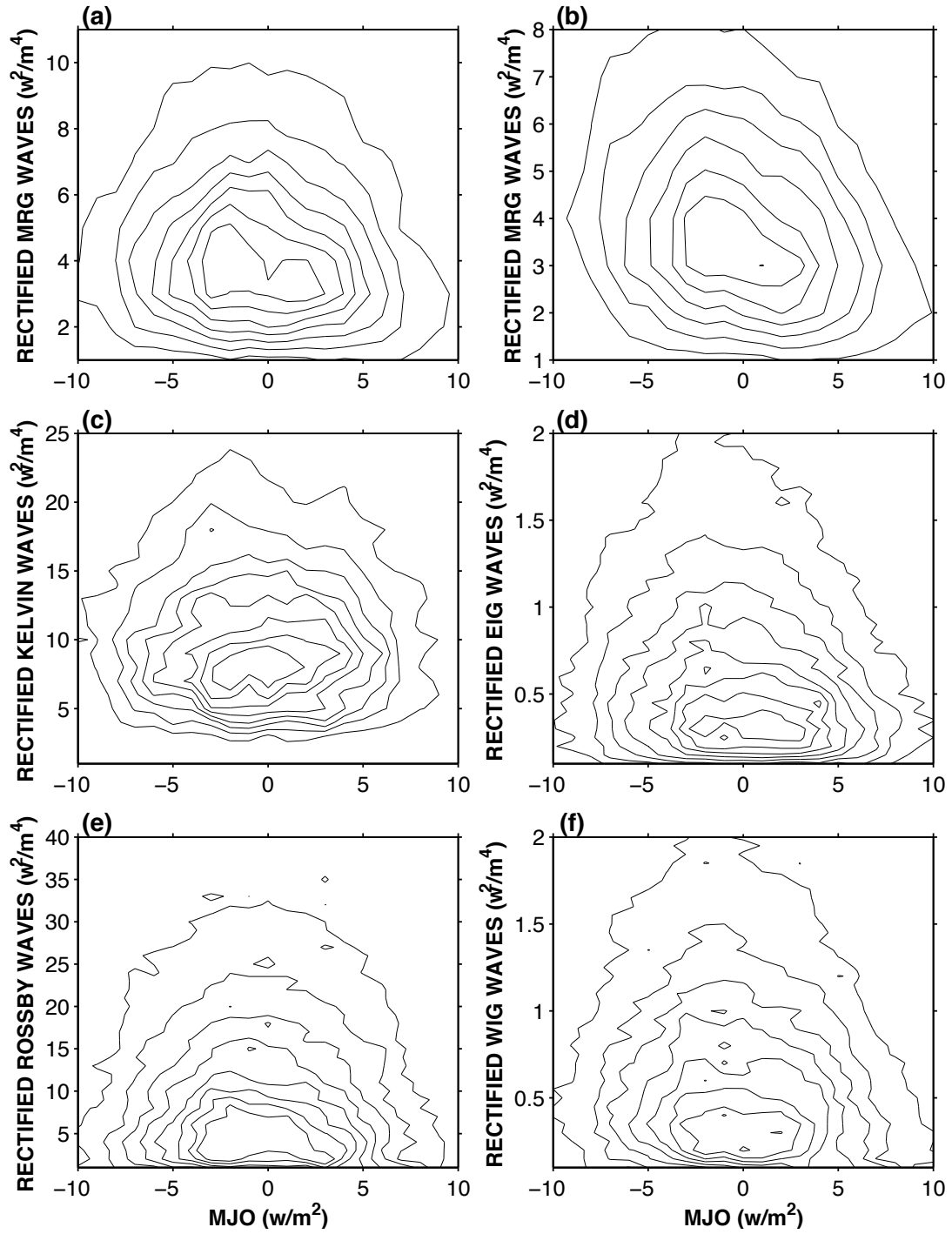
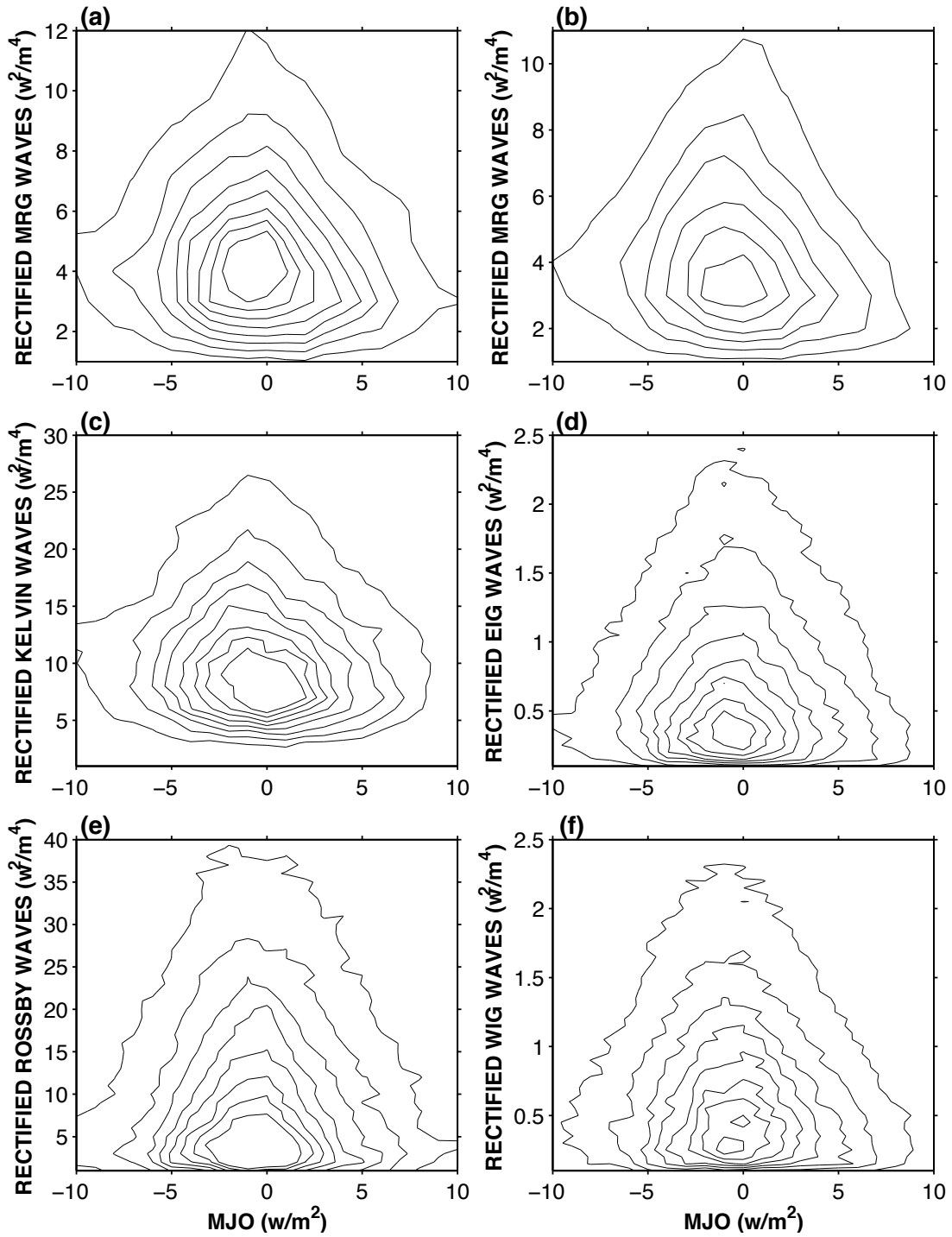


Figure 2.9. The joint probability distribution (JPD).



**Figure 2.10.** The same as Fig. 2.9, except for that these coefficients were computed for just the winter season (November to April) and the longitude range from 75°-185°E.

The above statistical analysis has been carried out within one Rossby deformation radius of the equator. Therefore the wave signals are mainly equatorial waves. We did not find significant correlations between the MJO and ER waves. This does not rule out the possibility that the MJO is initiated by subtropical Rossby waves (Hsu et al., 1990), or its propagation is associated with subtropical Rossby waves (Matthews et al., 1996), or that the mid-latitude exerts an influence on the tropics on intraseasonal time scales (Liebmann and Hartmann, 1984).

## **2.5 Discussion and Conclusions**

We have tested the hypothesis that the MJO is an MRG wave packet propagating with the MRG wave group velocity. The 3D numerical simulation indicates how the MRG wave packet could be forced, and it has some common features with the MJO, including the observed horizontal scale, local duration, and propagation speed. The numerical results suggest that the MJO could be an atmospheric response to a westward- or eastward-moving perturbation. However, when the forcing is not strictly antisymmetric, the MRG wave packet is not the dominant feature of the atmospheric response.

We are using a dry GCM. It will not simulate the relative arrangement of moisture and convection. With small amplitude forcing, it is a linear model. As a result, we cannot get all the MJO features, such as the horizontal wind structure and divergence field. This is because the divergence and vertical velocities of the MRG waves average out to zero on the scale of the wave packet, i.e., on the scale of the MJO. Nonlinear effects could alter this.

For instance, if updrafts were stronger than downdrafts, one would have net low-level convergence on the scale of the wave packet. Similarly, if condensation on updrafts outweighs evaporation on downdrafts, one would have net heating on the scale of the wave packet. In these cases the response would be similar to the model result of Gill (1980). It is possible that by adding a convection scheme to the GCM a more realistic MJO would be simulated, in that it would be covered by a cloud top, would have a baroclinic wind field, and would be subject to weather noise from higher latitudes.

We have carried out two analyses with the NOAA OLR data set. The first analysis is for the Indian Ocean MJO. We have found that there is a significant correlation between the MJO and most of the equatorial waves, except the ER and Kelvin waves. The second analysis is for the MJO from November to April. There is a significant correlation only between the MJO and the MRG waves. There are two caveats: First, correlations do not indicate causality, which means it is possible that the MJO is a separate entity that simply modulates the MRG wave (Aiyyer and Molinari 2003) and other correlated waves. Second, correlation analysis is a search for linear relationships, and there is no guarantee of a linear relationship between the rectified waves and the MJO signal. Nevertheless, the main conclusion is that the correlation coefficient is small, which suggests that the MRG waves explain only a small fraction of the MJO variance. The OLR data provide little support for the idea that the MJO propagation speed is set by the MRG wave group velocity. In addition, WK99 pointed out that the strongest OLR variance of the MRG band is near the dateline, with a weak variance in the Indian Ocean, which further weakens this hypothesis. Nevertheless, it is still possible that other data sets would reveal a larger correlation

between eastward-propagating wave packets and the MJO. Both using a moist GCM to simulate the MRG wave packets and doing a similar test with other more recent data sets would be worthwhile activities for the future work.

**Acknowledgments:** We thank Dr. Duane Waliser for useful comments and suggestions. This research was supported by the Geological and Planetary Sciences Davidow Fund of the California Institute of Technology.

## References:

Aiyyer, A. R. and J. Molinari, 2003: Evolution of mixed Rossby–gravity waves in idealized MJO environments. *J. Atmos. Sci.*, **60**, 2837–2855.

Biello, J., and A. J. Majda, 2005: A new multiscale model for the Madden–Julian oscillation. *J. Atmos. Sci.*, **62**, 1694–1721.

Chao, W. C., 1987: On the origin of the tropical intraseasonal oscillation. *J. Atmos. Sci.*, **44**, 1940–1949.

Chen, S. S., R. A. Houze Jr., and B. E. Mapes, 1996: Multiscale variability of deep convection in relation to large-scale circulation in TOGA COARE. *J. Atmos. Sci.*, **53**, 1380–1409.

De-Leon, Y., C. Erlick, and N. Paldor, 2010: The eigenvalue equations of equatorial waves on a sphere. *Tellus*, **62A**, 62-70, DOI: 10.1111/j.1600-0870.2009.00420.x.

Emanuel, K. A., 1987: An air–sea interaction model of intraseasonal oscillations in the Tropics. *J. Atmos. Sci.*, **44**, 2324–2340.

Gill, A. E., 1980: Some simple solutions for heat-induced tropical circulation. *Quart. J. Roy. Meteor. Soc.*, **106**, 447–462.

Hartmann D., and H. H. Hendon, 2007: Resolving an atmospheric enigma. *Science* **318**, 1731–1732, doi: 10.1126/science.1152502.

Held, I., and M. Suarez, 1994: A proposal for the intercomparison of the dynamical cores of atmospheric general circulation models. *Bull. Amer. Meteor. Soc.*, **75**, 1825-1830.

Hendon, H. H., and B. Liebmann, 1994: Organization of convection within the Madden-

Julian oscillation. *J. Geophys. Res.*, **99**, 8073–8083.

———, and M. L. Salby, 1994: The life cycle of the Madden and Julian oscillation. *J. Atmos. Sci.*, **51**, 2225–2237.

Hsu, H.-H., B. J. Hoskins, and F.-F. Jin, 1990: The 1985/86 intraseasonal oscillation and the role of the extratropics. *J. Atmos. Sci.*, **47**, 823–839.

Kiladis, G. N., M. C. Wheeler, P. T. Haertel, K. H. Straub, and P. E. Roundy, 2009: Convectively coupled equatorial waves. *Rev. Geophys.*, **47**, RG2003, doi:10.1029/2008RG000266.

Lau, K. M. and D. E. Waliser, 2005: Intraseasonal Variability in the Atmosphere–Ocean Climate System. Praxis, 436 pp.

Liebmann, B., and D. L. Hartmann, 1984: An observational study of tropical–midlatitude interaction on intraseasonal timescales during winter. *J. Atmos. Sci.*, **41**, 3333–3350.

Liebmann, B. and C.A. Smith, 1996: Description of a Complete (Interpolated) Outgoing Longwave Radiation Dataset. *Bulletin of the American Meteorological Society*, **77**, 1275–1277.

Lin, J.L., and Coauthors, 2006: Tropical Intraseasonal Variability in 14 IPCC AR4 Climate Models. Part I: Convective Signals. *J. Climate*, **19**, 2665–2690.

Madden, R. A., and P. R. Julian, 1972: Description of global-scale circulation cells in the tropics with a 40–50 day period. *J. Atmos. Sci.*, **29**, 1109–1123.

———, and ———, 1994: Observations of the 40–50-day oscillation—A review. *Mon. Wea. Rev.*, **122**, 814–837.

——, and ——, 2005: Historical perspective. *Intraseasonal Variability in the Atmosphere–Ocean Climate System*, K. M. Lau and D. E. Waliser, Eds., Springer-Verlag, 1–18.

Majda, A. J. and J. Biello, 2004: A multiscale model for tropical intraseasonal oscillations. *Proc. Natl. Acad. Sci. USA*, **101**, 4736–4741. doi:10.1073/pnas.0401034101.

—— and S. N. Stechmann, 2009: The skeleton of tropical intraseasonal oscillations. *Proc. Natl. Acad. Sci.*, **106**, 8417–8422, doi:10.1073/pnas.0903367106.

Maloney, E.D., A.H. Sobel, and W.M. Hannah, 2010: Intraseasonal Variability in an aquaplanet general circulation model. *J. Adv. Model. Earth Syst.* **2**, doi:10.3894/JAMES.2010.2.5.

Matsuno, T., 1966: Quasi-geostrophic motions in the equatorial area. *J. Meteor. Soc. Japan*, **44**, 25–42.

Matthews, A. J., B. J. Hoskins, J. M. Slingo, and M. Blackburn, 1996: Development of convection along the SPCZ within a Madden–Julian Oscillation. *Quart J. Roy. Meteor. Soc.*, **122**, 669–688.

Nakazawa, T., 1988: Tropical super clusters within intraseasonal variations over the western Pacific. *J. Meteor. Soc. Japan*, **66**, 823–839.

Neelin, J. D., I. M. Held, and K. H. Cook, 1987: Evaporation-wind feedback and low-frequency variability in the tropical atmosphere. *J. Atmos. Sci.*, **44**, 2341–2348.

Raymond, D. J., 2001: A new model of the Madden–Julian oscillation. *J. Atmos. Sci.*, **58**, 2807–2819.

Salby, M. L., and H. H. Hendon, 1994: Intraseasonal behavior of clouds, temperature and motion in the tropics. *J. Atmos. Sci.*, **51**, 2207–2224.

Sobel, A.H., E.D. Maloney, G. Bellon, and D.M. Frierson, 2010: Surface fluxes and tropical intraseasonal variability: a reassessment. *J. Adv. Model. Earth Syst.* **2**, doi:10.3894/JAMES.2010.2.2.

Solodoch, A., W. Boos, Z. Kuang, and E. Tziperman, 2010: Excitation of slow MJO-like Kelvin waves in the equatorial atmosphere by Yanai wave-group via a WISHE-induced convection. *J. Atmos. Sci.*, **68**, 210-225.

Straub, K. H., and G. N. Kiladis, 2003: Interactions between the boreal summer intraseasonal oscillation and higher frequency tropical wave activity. *Mon. Weather Rev.*, **131**, 945–960.

Wang, B., 2005: Theories. *Intraseasonal Variability in the Atmosphere–Ocean Climate System*. K. M. Lau and D. E. Waliser, Eds., Praxis, 307–360.

———, and H. Rui, 1990: Dynamics of the coupled moist Kelvin–Rossby wave on an equatorial  $\beta$ -plane. *J. Atmos. Sci.*, **47**, 397–413.

Wheeler, M., and G. N. Kiladis, 1999: Convectively coupled equatorial waves: Analysis of clouds and temperature in the wavenumber-frequency domain. *J. Atmos. Sci.*, **56**, 374–399.

Zhang, C., 2005: Madden-Julian Oscillation. *Rev. Geophys.*, **43**, RG2003, doi:10.1029/2004RG000158.

———, M. Dong, S. Gualdi, H. H. Hendon, E. D. Maloney, A. Marshall, K. R. Sperber, and W. Q. Wang, 2006: Simulations of the Madden-Julian oscillation in four pairs of coupled and uncoupled global models. *Climate Dyn.*, **27**, 573–592.

Zou, J., and H-R. Cho, 2000: A nonlinear Schrödinger equation model of the intraseasonal oscillation. *J. Atmos. Sci.*, **57**, 2435–2444.



## Chapter 3

# Triggered Convection, Gravity Waves, and the MJO: A Shallow Water Model<sup>\*</sup>

### 3.1 Abstract

The Madden—Julian oscillation (MJO) is the dominant mode of intraseasonal variability in the tropics. Despite its primary importance, a generally accepted theory that accounts for fundamental features of the MJO, including its propagation speed, planetary horizontal scale, multi-scale features, and quadrupole structures, remains elusive. In this study, we use a shallow water model to simulate the MJO. In our model, convection is parameterized as a short-duration localized mass source, and is triggered when the layer thickness falls below a critical value. Radiation is parameterized as a steady uniform mass sink. The following MJO-like signals are observed in our simulations: (1) slow eastward-propagating large-scale disturbances, which show up as low-frequency, low-wavenumber features with eastward propagation in the spectral domain, (2) multi-scale structures in the time-longitude (Hovmoller) domain, and (3) quadrupole vortex structures in the longitude-latitude (map view) domain. We propose that the simulated MJO signal is an interference

---

<sup>\*</sup> Appeared as: Yang, Da, Andrew P. Ingersoll, 2013: Triggered Convection, Gravity Waves, and the MJO: A Shallow-Water Model. *J. Atmos. Sci.*, **70**, 2476–2486.

pattern of westward and eastward inertia-gravity (WIG and EIG) waves. Its propagation speed is one half of the speed difference between the WIG and EIG waves. The horizontal scale of its large-scale envelope is determined by the bandwidth of the excited waves, and the bandwidth is controlled by the number density of convection events. In our model, convective events trigger other convective events, thereby aggregating into large-scale structures, but there is no feedback of the large-scale structures onto the convective events. Our results suggest that the MJO is not so much a low-frequency wave, in which convection acts as a quasi-equilibrium adjustment, but is more a pattern of high-frequency waves that interact directly with the convection.

### **3.2 Introduction**

The Madden–Julian oscillation (MJO) is the dominant intraseasonal variability in the tropical atmosphere. It is a planetary-scale, slow eastward-propagating (about 5 m/s) perturbation of both dynamical and thermodynamical fields. During an MJO event, a positive convection and rainfall anomaly develops in the western Indian Ocean and propagates to the western Pacific Ocean. Once the perturbation reaches the date line, the perturbation is largely confined to dynamical fields. The associated planetary-scale wind structure is baroclinic and is characterized by low-level convergence and upper-level divergence (Madden and Julian 1972, 1994; Hendon and Salby 1994). More details can be found in comprehensive reviews such as Madden and Julian (2005) and Zhang (2005). In addition, within the MJO envelope, there are both westward- and eastward-moving finescale structures (Nakazawa 1988; Hendon and Liebmann 1994).

The significance of the MJO for phenomena such as monsoon onset, ENSO, and rainfall patterns in the tropics has been well established (Zhang 2005). However, a successful MJO theory is elusive. For a historical and detailed review of theories, please refer to Zhang (2005) and Wang (2005). Here we will review three schools of theories. One school considers the MJO as a large-scale unstable mode in the tropics, and it is often referred to as the moisture mode. The moisture mode arises from positive feedbacks between precipitation and the source of moist static energy (e.g., Neelin and Yu 1994; Sobel et al. 2001; Fuchs and Raymond 2002, 2005; Bretherton et al. 2005; Fuchs and Raymond 2007; Maloney 2009; Raymond and Fuchs 2009; Andersen and Kuang 2012). Another school still considers the MJO as a large-scale mode, but the major instability to maintain the planetary-scale envelope happens in the synoptic scales. Both observational and modeling studies suggest that high-frequency small-scale waves are important to the MJO (e.g., Hendon and Liebmann 1994; Tung and Yanai 2002; Moncrieff 2004; Biello and Majda 2005; Khouider et al. 2012). Thus, Majda and Stechmann (2009, 2011) emphasize the importance of small-scale waves within the MJO envelope, but they parameterize the effect of the waves. In their model, it is only the amplitude of the wave activity envelope that is needed, not any of the details of the particular synoptic-scale waves that make up the envelope. The third school considers the MJO as a wave packet of a certain type of equatorial waves, and the MJO propagates with the group velocity of the equatorial waves. Yang and Ingersoll (2011) hypothesize that the MJO is a mixed Rossby–gravity (MRG) wave packet that propagates with the MRG group velocity, and they test this hypothesis, both with an idealized general circulation model (GCM) and with the outgoing longwave radiation (OLR) dataset. They force with a westward-moving heat source that lasts for 10

or 20 days. At the same time, Solodoch et al. (2011) suggest that the MJO could be a forced response to the MRG wave group in the quasi-equilibrium (QE) convection and wind-induced surface heat exchange context. Neither theory considers inertia–gravity (IG) waves, which have frequencies greater than 0.5 cpd. In the QE context, these high-frequency, small-scale waves will be damped the fastest, and it is possible that the QE approach does not apply there. Therefore, the role of high-frequency, small-scale waves has not really been investigated in any of the theories, including the wave packet theories of the MJO. Here we present a simple MJO model with triggered (non-QE) convection that emphasizes the multiscale structures of the MJO.

General circulation models (GCMs) simulate tropical intraseasonal variability with varying degrees of fidelity. Intercomparison studies (Lin et al. 2006) show that most GCMs underestimate the MJO variance. The weak MJO signals in GCMs are believed to be caused by inadequate convection schemes in the GCMs. Holloway et al. (2012) compare limited-area simulations of the tropical atmosphere over a very large domain at different horizontal resolutions with both parameterized and explicit convection versions for a 10-day MJO case study in April 2009. They claim that the parameterized models consume convective available potential energy (CAPE) and reach radiative–convective equilibrium too quickly and that they lack the ability to transition from suppressed to active conditions and vice versa. As a result, propagating MJO signals are absent in the parameterized runs.

There are two common ways of treating convection: triggered and QE convection. There is

not a clear distinction between these two categories. Over a long period, in the tropics, the generation of CAPE by large-scale processes nearly balances its consumption by convection. The convection may be considered to be in a state of statistical equilibrium with the large-scale circulation. The QE idea was first applied by Arakawa and Schubert (1974). This idea has been validated using observational datasets by Xu and Emanuel (1989) and Holloway and Neelin (2007). QE is a good assumption for studying large-scale circulations that vary slowly with time compared with convective time scales. Such circulations include tropical cyclones, the Hadley cell, and monsoon circulations (e.g., Emanuel et al. 1994; Emanuel 2007), but so far the MJO has not been successfully simulated under the QE context. If we are interested in high-frequency, small-scale waves, however, QE does not work well. First, over a short period, CAPE builds up. When some threshold is reached, convection is triggered and CAPE is released. Second, in a QE scheme, convection will damp small-scale waves faster and leave the large-scale waves.

Recent studies (Benedict and Randall 2009) with a superparameterized (SP) Community Atmosphere Model (CAM) show improved MJO simulations. The SP CAM replaces conventional boundary-layer, moist-convection parameterizations with a cloud-resolving model embedded in each CAM grid cell (Khairoutdinov and Randall 2001). The SP CAM deals with subgrid-scale variability more accurately. Our interpretation of the SP CAM results is that the cloud-resolving model has a continuous spectrum from the triggered convection to statistical equilibrium convection, such that it treats the high-frequency, small-scale waves, which are crucial to the MJO, equally well as the low-frequency, large-scale variability.

Motivated by the success of SP CAM simulations, we develop a theory emphasizing the role of high-frequency, small-scale waves. In this paper, we use a shallow-water model with triggered convection and radiation represented as Newtonian relaxation. Slow eastward-propagating (MJO-like) signals are observed in our simulations. Instead of thinking of the MJO as a large-scale stable or unstable mode, we propose that the MJO-like signals are interference patterns of westward and eastward inertia– gravity (WIG and EIG) waves that interact directly with the convection. Eastward propagation is due to the zonal asymmetry of the EIG and WIG waves. In section 2, we will introduce the shallow-water model used in this study. In sections 3 and 4 we show our simulation results and attempts to understand the simulated signal. In section 5, we will discuss our results and present our conclusions and future work.

### **3.3 Model Description**

We use a 2D shallow-water model in this study. We simulate the upper troposphere by assuming the first baroclinic mode, since the large-scale circulation associated with the MJO shows the first baroclinic structure. Thus, divergence in the model refers to upper-level divergence and low-level convergence. Similarly, large layer thickness in the model corresponds to high pressure aloft and low pressure near the surface. In this section, we will introduce the shallow-water model used in this study.

This shallow-water model describes the evolution of constant density, incompressible fluid

over the surface of the sphere. The model equations are

$$\partial_t u = fv - \frac{u}{a \cos \theta} \partial_\lambda u + \frac{v}{a} \partial_\theta u + \frac{uv \tan \theta}{a} - \frac{1}{a \cos \theta} \partial_\lambda \phi, \quad (3.1)$$

$$\partial_t v = -fu - \frac{u}{a \cos \theta} \partial_\lambda v + \frac{v}{a} \partial_\theta v + \frac{u^2 \tan \theta}{a} - \frac{1}{a} \partial_\theta \phi, \quad (3.2)$$

$$\partial_t \phi = -\nabla \cdot (V\phi) + q - r. \quad (3.3)$$

Equations (3.1) and (3.2) are momentum equations, where  $u$  and  $v$  are zonal and meridional velocities;  $\phi$  is the geopotential, which is gravity  $g$  times the equivalent layer thickness (equivalent depth);  $a$  is the earth radius;  $f$  is the Coriolis parameter (also known as planetary vorticity); and  $\lambda$  and  $\theta$  represent longitude and latitude in radians. Equation (3.3) is the continuity equation, where  $q$  represents convective heating, which is a mass source, and  $r$  represents radiative cooling, which is a mass sink.

In this model, convection events are triggered by a low value of the layer thickness, that is, if the layer thickness is lower than a threshold  $\phi_c$ , convection will start to add mass into this shallow-water system. This trigger mechanism can be related to mass accumulation in the lower troposphere. In this model, we assume the first baroclinic mode and simulate the upper troposphere. A low value of  $\phi$  is equivalent to an accumulation of mass and moisture in the lower troposphere. This is an environment that favors convection. The convective heating is given by

$$q = \begin{cases} \frac{q_0}{\tau_c A_0} \left[ 1 - \left( \frac{\Delta t - \tau_c / 2}{\tau_c / 2} \right)^2 \right] \left( 1 - \frac{L^2}{R^2} \right) & \text{when } \phi < \phi_c, \quad 0 < \Delta t < \tau_c, \quad L^2 < R^2, \\ 0 & \text{otherwise,} \end{cases} \quad (3.4)$$

where  $q_0$  is a free parameter of the heating amplitude,  $\tau_c$  is the convective time scale, and  $\Delta t$  is measured relative to the time when convection is triggered. Each convection event operates in a certain area  $A_0 = \pi R^2$ , where  $R$  is the radius of each convection event. The equation  $L = (\Delta x^2 + \Delta y^2)^{1/2}$  measures the distance from the convective center, where  $\Delta x$  and  $\Delta y$  are measured relative to the location where the convection is triggered.

The radiative cooling is constant in both time and space. The ratio  $3r / q_0$  determines  $\dot{\Sigma}$ , the rate of initiation of convection events per unit area per unit time. In a statistically steady state, the total mass of this system will not change with time. Convection, the mass source, will be balanced by the mass sink, radiation. The equilibrium geopotential is approximately  $\phi_c$ .

The shallow-water equations have characteristic length and time scales through the planetary radius and the rotation. In addition to the planetary radius and rotation, there are four parameters: the equilibrium geopotential  $\phi_c$ ,  $A_0$ ,  $\tau_c$ , and  $\dot{\Sigma}$ , which is controlled by  $r$  through the relation  $\dot{\Sigma} \sim 3r / q_0$ . Both  $q_0$  and  $r$  are small, so the fluid dynamics in our

model are linear. Therefore, the forcing amplitudes are not free parameters and only the ratio between the two terms matters. The forcing is through  $q_0$  and  $r$ , and they cause  $\phi$  to fluctuate around  $\phi_c$ , which appears in Eq. (3.4). So for constant  $\dot{\Sigma} \sim 3r/q_0$ , the three variables  $u$ ,  $v$ , and  $\phi - \phi_c$  all scale as  $r$ , which can be arbitrarily small. We can scale  $r$  and the other variables by any small number, then run the model, undo the scaling, and the results are statistically the same. Therefore, the absolute value of our model output is not important. Only the relative magnitude matters.

Scaling is one property of linear systems, but our model is not linear. It does not satisfy superposition. The model has a given climatology, which is independent of the initial conditions. If we superpose two sets of initial conditions and then run the model, we get a different answer than we would get by superposing the two solutions after running the model. The nonlinearity does not come from the advection term, since the scaled amplitude can be arbitrarily small. Instead, it comes from the forcing terms  $r$  and  $q$  and the threshold condition in Eq. (3.3).

The Kelvin wave speed  $c$  is equal to  $\sqrt{\phi_c}$ . In this study, we fix  $c \sim 16$  m/s. The mean depth  $h_e$  (equivalent depth) of this SW system is given by  $\phi_c/g$ . In our control simulation,  $R$  is  $3^\circ$  of latitude, which is approximately the size of the grid in T42 simulations. Parameter values of our control simulation are documented in Table 1. We vary the horizontal resolution from T42 to T170 and find our main results are not sensitive to resolution. The

results presented in this paper are mainly from T42 simulations. We solve these equations in spherical coordinates by using the spectral dynamical core of the Geophysical Fluid Dynamics Laboratory (GFDL) Flexible Modeling System. Each simulation is initialized with random noise. Although we do not have a moisture variable explicitly in our model, our model does illustrate the importance of moisture to the MJO.

**Table 3.1** Parameter values in the control simulation.

$\phi_c$ (m/s) <sup>2</sup>	$R_\theta$ (°)	$\tau_c$ (day)	$\dot{\Sigma}$ (m <sup>-2</sup> s <sup>-1</sup> )
250	3	0.25	$1.12 \times 10^{-17}$

### 3.4 Simulation Results

Figure 3.1 shows Hovmöller diagrams of our shallow water simulation from day 500 to day 600. Figure 3.1 shows the symmetric components of the geopotential, zonal wind, and convective heating and the antisymmetric components of meridional wind. The symmetry is with respect to the equator. Such meridional symmetry excludes the even meridional-wind modes and leaves the odd modes. Figure 3.1a shows the geopotential. There are two major large-scale events labeled A and B. These are the MJO-like signals. They move

eastward at  $\sim 3.0$  m/s. Small-scale waves are present, and they include Kelvin waves, inertia-gravity (IG) waves and Rossby waves. Since the IG waves are small scale waves, the absolute values of their speed are close to the Kelvin wave speed, which is  $\sim 16$  m/s. Figure 3.1b shows the zonal wind. The white represents westward zonal wind, and the black represents eastward zonal wind. The edge between the white and black indicates the divergence of zonal wind. Two regions of large-scale divergence are observed, and they are collocated with events A and B in Fig. 3.1a. Figure 3.1c shows the meridional velocity  $v$ . Small-scale westward and eastward waves are observed, but large-scale envelopes are not clear in the  $v$  field. Figure 3.1d shows convective heating. Convection is a small-scale, short-duration process, but two organized long-lasting events are observed, and they are collocated with events A and B in Fig. 3.1a and with large-scale divergence in Fig. 3.1b. Similar to the observation, large-scale divergence is collocated with convective centers, and dynamical fields are coupled to convection.

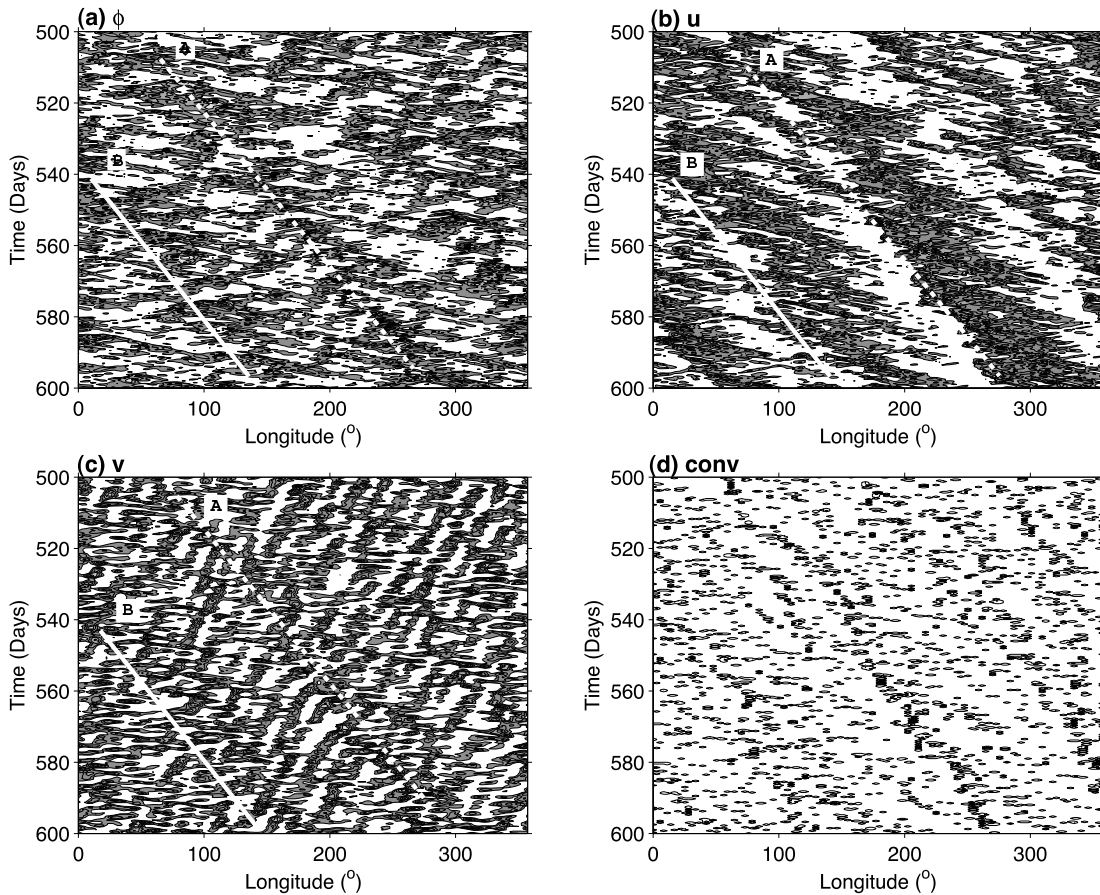


**Figure 3.1.** Hovmöller diagrams of the (a) geopotential, (b) zonal wind, (c) meridional wind, and (d) convective heating of our shallow-water simulation from  $-15^\circ$  to  $15^\circ$  latitude. The geopotential, zonal wind, and convective heating are symmetric components about the equator, and the meridional wind is the antisymmetric component. The white (black) represents low (high), and the contour interval is linear. The forcing amplitude is arbitrarily small. Therefore, the absolute value of our model output is not important. The dashed and solid lines represent MJO events A and B, respectively, and the propagation speeds are both about 3.0 m/s.

Figure 3.2 shows the Hovmöller diagrams of the zonal wind from T85 and T170 simulations with the same parameters as the T42 simulations of Fig. 3.1b. The size of the convection in kilometers is the same. They both show propagation speeds and horizontal structures that are similar to the T42 simulations. This comparison suggests that the T42

simulations have already converged. When  $R$  is  $3^\circ$ , convection is not well resolved in T42 simulations, and this induces discontinuities between grid points. However, such discontinuity can be smoothed out by hyperviscosity. As a result, T42 simulations produce similar results to T85 and T170 simulations, where convection is well resolved. In the rest of the paper, the simulation results are from the T42 simulations, unless otherwise noted.

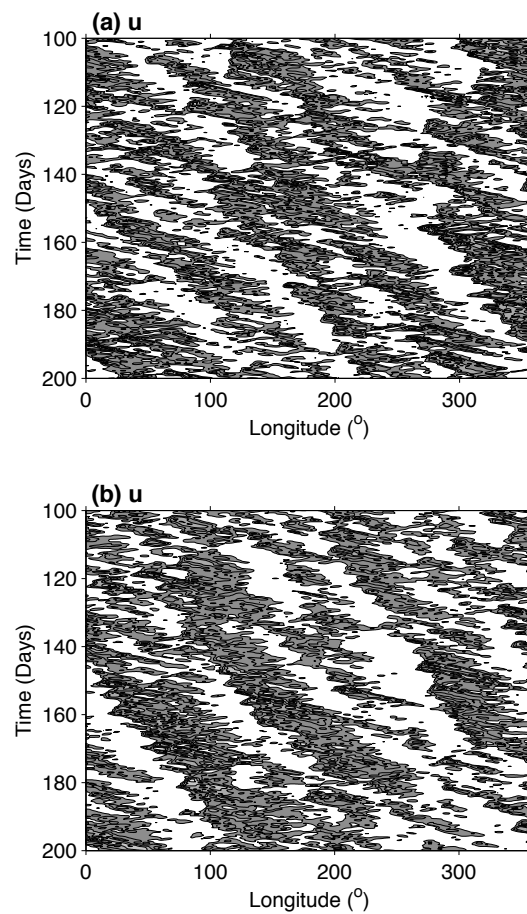


**Figure 3.2.** Hovmöller diagrams of zonal wind from (a) T85 and (b) T170 simulations. Colors and contour intervals are as in Fig. 3.1b.

To understand the multi-scale structures in our simulation, we carried out space-time spectral analysis as pioneered by Wheeler and Kiladis (1999, hereafter WK99). Figures 3.3a and b show, respectively, the symmetric and antisymmetric components (about the equator) of the zonal wind. Superimposed curves represent dispersion relations of equatorial waves for an assumed 16 m/s Kelvin wave speed. The dispersion curves of the equatorial waves were first derived by Matsuno (1966). Different equatorial waves are characterized by different dispersion relations and meridional mode numbers  $n$ . The spectral power under the superimposed curves is associated with the corresponding equatorial waves. In Fig. 3.3a, we can see spectral peaks associated with the  $n = 1$  Rossby wave, the Kelvin wave, and the  $n = 1$  and  $n = 3$  IG waves. Consistent with the slowly eastward moving signals in Fig. 3.1, Fig. 3.3a has an MJO-like signal within the white box. This signal has planetary scale and low frequency. In the rest of this paper, we will try to understand this interesting phenomenon. In Fig. 3.3b, we can see spectral peaks associated with the  $n = 2$  Rossby wave, the MRG wave and the  $n = 2$  IG wave. A striking feature of Fig. 3.3 is the intense power associated with high frequency IG waves. High IG wave activity is associated with the convective parameterization in our model. We will argue that high IG wave activity is the key to the MJO-like signal. Nevertheless, most of the power is concentrated in low wavenumber and low frequency region. This is, in general, a red spectrum. Although different in details, Fig. 3.3 captures some fundamental features of the observed spectra by WK99.

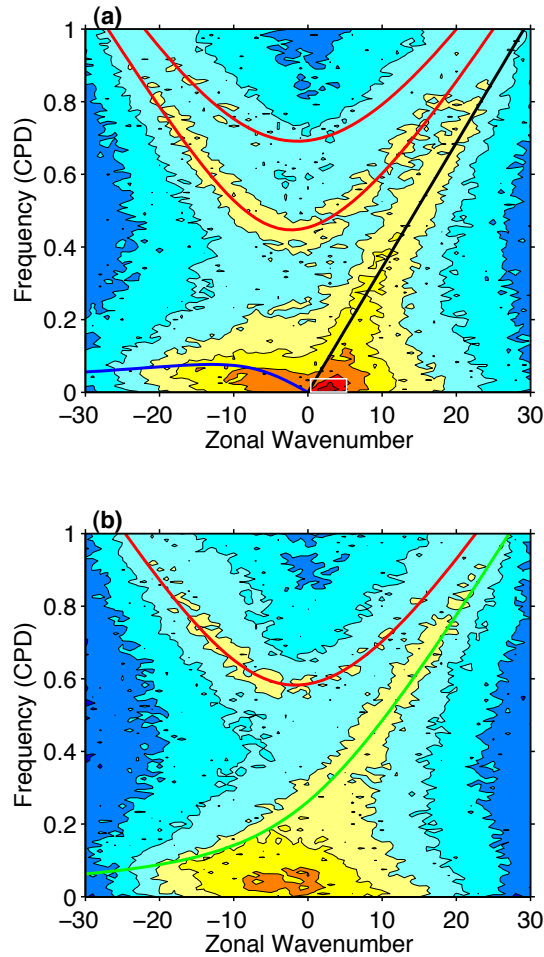


**Figure 3.3.** Zonal wavenumber–frequency power spectra of zonal wind from  $-15^{\circ}$  to  $15^{\circ}$  latitude for (a) symmetric and (b) anti-symmetric components. Red represents high-power density, and blue represents low-power density. Red, blue, black, and green lines denote dispersion curves of IG, Rossby, Kelvin, and MRG waves, respectively, for different meridional modes. The white box in (a) ranges from 1 to 5 in wavenumber and from  $1/60$  to  $1/200$  cpd in frequency. The logarithm to the base 10 is taken for plotting, and the contour interval is 0.5.

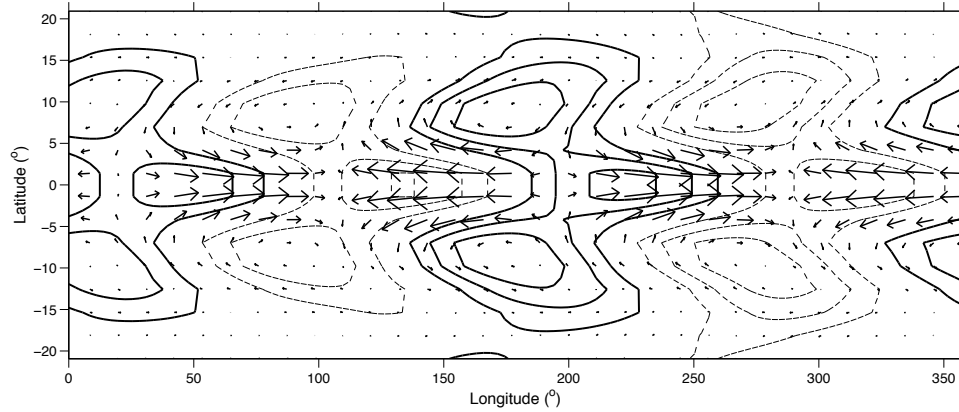


**Figure 3.4.** Longitude–latitude map of composites of the MJO-like signals. The arrows denote the wind field  $\mathbf{V} = (u, v)$ , and the contours denote the geopotential. The thick solid (thin dashed) contours represent positive (negative) anomalies with linear contour intervals.

Figure 3.4 shows the horizontal structure of the MJO-like signal in our simulation. To get Fig. 3.4, we take the MJO-filtered signal of the zonal wind in the wavenumber-frequency domain. The filtering excludes all wavenumbers and frequencies except those in the MJO box (Fig. 3.3a). Following Wheeler and Hendon (2004), we carried out empirical orthogonal function (EOF) analysis of the MJO filtered signal. We found the first two EOFs can contribute about 85% of the total variance of the MJO filtered signal. The EOFs together with the corresponding principal components (PCs) show the propagation behavior of the MJO-like signal. Combining all the phases of the MJO-like signal, we get the horizontal structure shown in Fig. 3.4. The contours represent the geopotential, and the vectors represent the wind. Away from the equator we can see cyclonic and anticyclonic vortices. At the equator, the wind is more zonal, and the contours are more parallel to the equator. In this figure, a wavenumber-2 pattern stands out, that is, the zonal wind alternates from eastward to westward twice in the domain. Consider one cycle of the pattern, that between  $100^\circ$  and  $280^\circ$  longitude. The maximum divergence of the zonal wind occurs at

180°. To the west of the maximum divergence, at about 160°, there are anticyclones to the north and the south, collocated with high geopotential anomalies. To the east of the divergence of the zonal wind, there are cyclones centered at about 10° latitude, together with low geopotential anomalies. This structure is referred to as the quadrupole vortex structure (Majda and Stechmann 2009). The quadrupole vortices in our simulations are confined more closely to the equator than in the MJO as reported by Kiladis et al. (2005), where the off-equatorial vortices center at about 20° latitude.

### 3.5 Proposed Mechanism

MJO-like signals have been simulated in our model. The simulated signal captures major features of the MJO, including propagation speed, horizontal scale, multiscale structures, and quadrupole vortex structures. The next step is to understand the slow eastward propagation and the low wavenumber of the disturbance. Figure 3.5 shows high-resolution Hovmöller diagrams. In this high-resolution view, we are able to diagnose how convection is triggered and how waves are excited. In Fig. 3.5a, there is a standing oscillation at a longitude of about 206°. On day 163.75, there is a local minimum of  $\phi$  at 206°. This triggers a convection event. A quarter cycle later, the convection reaches its maximum value, and a quarter cycle after that,  $\phi$  reaches a local maximum. Half a cycle later,  $\phi$  is a local minimum and another convection event is triggered. Such cycles repeat five times in Fig. 3.5 with a period of 0.5 day, which is twice  $\tau_c$ . The amplitude of convective heating is small, so there is no nonlinearity due to advection. Standing waves are excited, and their frequency is approximately  $1/2 \tau_c$ . We call this the quasi frequency. Convection excites IG waves at this frequency, but it excites waves at other frequencies, including zero, as well.

The series of convection events shown in Fig. 3.5 is like the top half of a truncated sine wave. Many frequencies are present in this function. Thus, energy is introduced into this shallow-water system. The standing oscillation can be viewed as a superposition of eastward and westward waves with similar speeds. In the power spectra, WIG and EIG waves are the only waves that propagate toward each other with the same meridional structures and similar propagation speed. Therefore, the simulated MJO signal is an interfering pattern between WIG and EIG waves, which are excited by convection. The propagation speed of the MJO pattern is associated with the phase speed difference between WIG and EIG waves.

**Table 3.2** Parameter ranges in Fig. 3.6.

$R$ (°)	$\tau_c$ (day)	$\dot{\Sigma}$ ( $10^{-18} \text{ m}^2 \text{ s}^{-1}$ )	Resolution
1.5-3.0	0.5-0.85	2.8-11.2	T85-T170

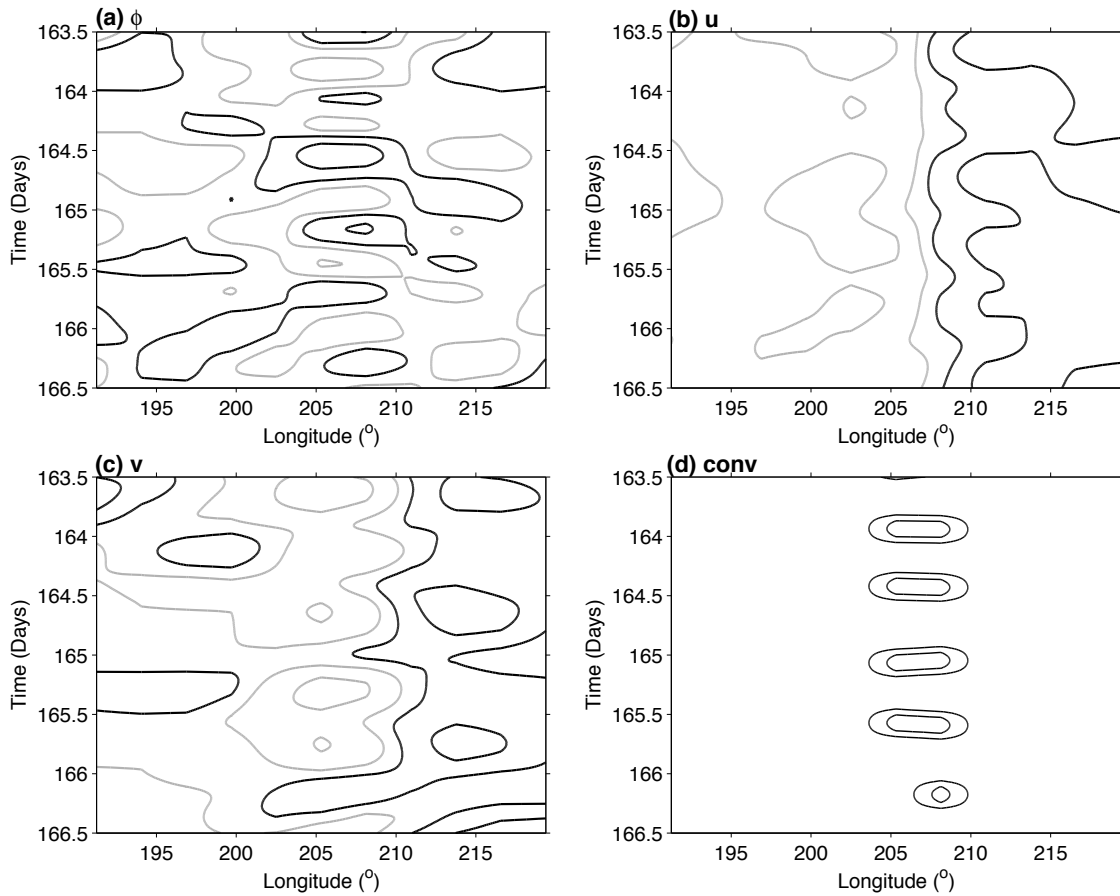


**Figure 3.5.** High-resolution Hovmöller diagrams of the (a) geopotential, (b) zonal wind, (c) meridional wind, and (d) convective heating of our shallow-water simulation from  $-6^\circ$  to  $6^\circ$  latitude. The geopotential, zonal wind, and convective heating are symmetric components about the equator, and the meridional wind is the antisymmetric component. The black (gray) line denotes positive (negative) anomalies with linear contour intervals.

Figure 3.6 shows how our hypothesis could explain the MJO propagation speed quantitatively. If the hypothesis is correct, the MJO propagation speed is one-half of the phase speed difference between the WIG and EIG waves. In Eq. (3.5), the EIG phase speed is  $c_1$ , the WIG phase speed is  $c_2$ , and the cosine factor on the right-hand side is the standing oscillation. The sine factor on the right-hand side is the drift of the pattern at the MJO propagation speed:

$$\sin[k(x - c_1 t)] + \sin[k(x + c_2 t)] = 2 \sin\left[k\left(x - \frac{c_1 - c_2}{2} t\right)\right] \cos\left(k \frac{c_1 + c_2}{2} t\right). \quad (3.5)$$

The solid line denotes the theoretically derived MJO propagation speed from the dispersion relation of the two lowest symmetric IG waves, with  $n = 1$  and  $n = 3$ . The markers represent simulation results with different parameters. The abscissa is the quasi frequency of IG waves. We have systematically varied the parameters in our model, including  $R$ ,  $\tau_c$ ,  $\dot{\Sigma}$ , and the model resolution (Table 2). There is a finite spread in speed when fixing  $\tau_c$  and changing other parameters. However, simulation results show consistent behavior when varying  $\tau_c$ . The lower solid curve, corresponding to  $n = 1$ , fits our simulation results relatively well, especially for the T170 simulations. At the high-frequency end of this plot, the simulated speeds seem to level off at 2 m/s, which corresponds to the quasi-standing wave speed at a frequency of about 0.7 cpd. As shown in Fig. 3.3a, this is the minimum frequency of the  $n = 3$  mode. The  $n = 1$  mode fits the numerical model below this frequency because it is the only mode that can exist. At frequencies above 0.7 cpd, convection excites both the  $n = 1$  mode and the  $n = 3$  mode. At still higher frequencies, convection will excite even higher meridional modes, and no single mode will match the numerical results.

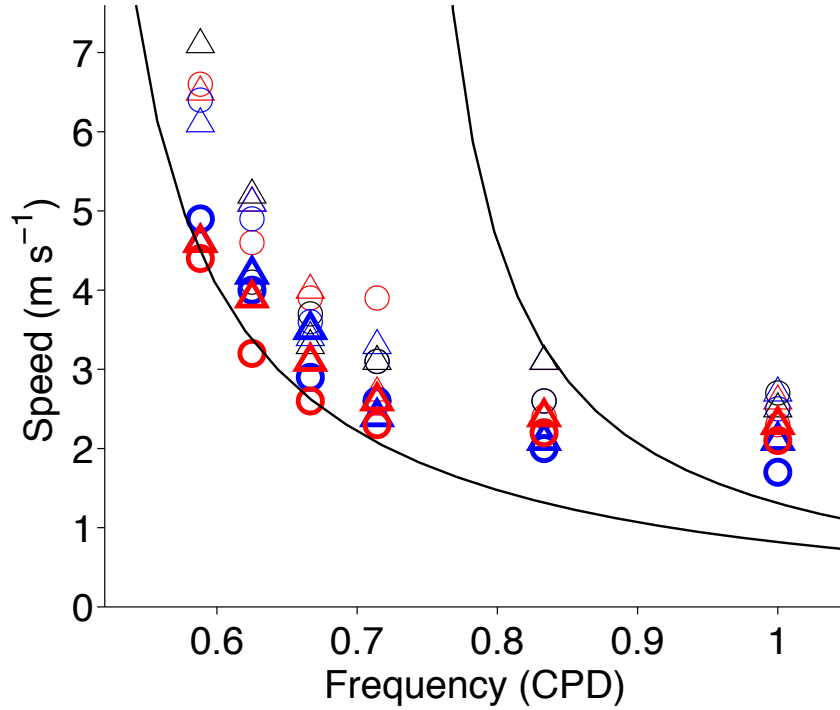


**Figure 3.6.** Propagation speed (m/s) vs quasi frequency (cpd). The lower and upper solid lines are derived from the dispersion relations of the  $n = 1$  and  $n = 3$  IG waves, respectively. The markers represent the simulation results for different parameters. The thicker markers are for the T170 simulations, and the thin ones are for T85 simulations. The markers are red when  $\dot{\Sigma} = \dot{\Sigma}_0$ , blue when  $\dot{\Sigma} = 0.5\dot{\Sigma}_0$ , and black when  $\dot{\Sigma} = 0.25\dot{\Sigma}_0$ . The triangles are for simulations when  $R = R_0$ , and the circles are for simulations when  $R = 0.5R_0$ , where  $R_0 = 3.0^\circ$ . For example, a thick red circle is from the T170 simulation with  $\dot{\Sigma} = \dot{\Sigma}_0$  and  $R = 0.5R_0$ . We convert  $\tau_c$  to frequency by using frequency equals  $1/2\tau_c$ . The values of  $R_0$  and  $\dot{\Sigma}_0$  are given in Table 1.

Another reason the propagation speeds level off at high frequencies (Fig. 3.6) is that convection might be exciting quasi-standing waves at frequencies below  $1/2\tau_c$ . This could happen because the convection is not a single-frequency signal and has a dc component. Because of the positive-only convective heating, there is a net heating at one place that

persists over several cycles of the wave—a time period longer than  $2\tau_c$ . As a result, waves with frequency lower than  $1/2\tau_c$  will be excited and possibly amplified. This is why we call  $1/2\tau_c$  the quasi frequency rather than the forcing frequency. The main conclusion from Fig. 3.6 is that the propagation speed of the MJO-like disturbance is that of the quasi-standing IG wave. The evidence for this statement is strongest at frequencies below 0.7 cpd, where only the  $n = 1$  wave can be excited. At those frequencies, the quantitative agreement is quite good. At higher frequencies there is a mixture of waves, and it is harder to see the effects of any one wave.

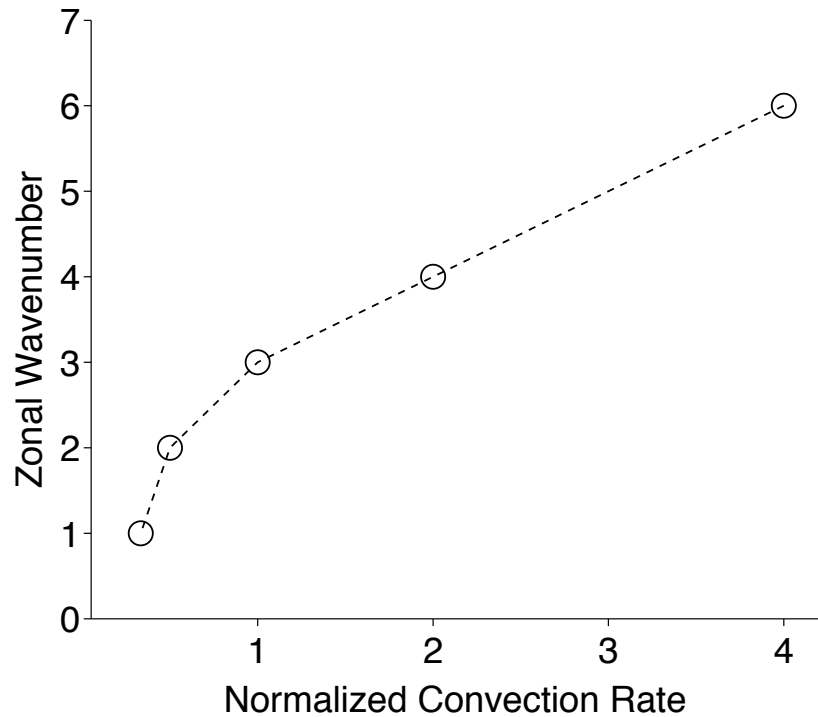


**Figure 3.7.** Zonal wavenumber vs. normalized convection rate  $\dot{\Sigma}/\dot{\Sigma}_0$ , where  $\dot{\Sigma}_0$  is given in Table 1.

As an interference pattern, the horizontal scale of the MJO will be inversely related to the bandwidth of the excited waves—the number of zonal wavenumbers that are excited. Our simulations show that the bandwidth of waves is associated with how many convection events are happening at the same time, that is,  $\dot{\Sigma}$ . If  $\dot{\Sigma}$  is large, many waves with various frequencies are excited and the bandwidth is large. However, if there are only a few convection events during the simulation, only a few waves are excited and the bandwidth is small. Because of the dc component of the heating, the low frequencies are related to the persistence of the gravity wave rather than to its period. With many convection events happening at once, the phase and amplitude of the gravity waves are constantly changing. The heating does not persist at any one place, and the low frequencies do not develop. Since the convection rate  $\dot{\Sigma}$  is of order  $3r/q_0$ , increasing  $r$  will increase  $\dot{\Sigma}$  if all the other parameters are fixed. As a result, the MJO wavenumber increases. Figure 3.7 shows the results of systematic experiments where the MJO wavenumber increases as  $r$  increases. The amplitude of the convective forcing is small so that the waves are linear waves, and decreasing the convective strength does the same job as increasing  $r$ .

One must ask, how does convection, which is a small-scale, short-duration event, generate a large-scale, low-frequency response in our shallow-water system? The answer is that convection excites a range of frequencies, including zero frequency since convection has a dc component, given by the threshold behavior of convection. It may appear strange that a model forced at short time scales is giving rise to oscillations at low frequencies, especially since the advection terms are negligible. But the model is not externally forced: it is self-

excited. Convection excites a quasi standing IG wave, which triggers more convection events in the vicinity of recent convection events. In the statistically steady state, one has a large-scale, slowly varying aggregation of convection events. In our model, the large-scale pattern does not directly affect the convection events, which have an intrinsic tendency to self-aggregate through exciting quasi-standing IG waves. However, the convection has a dc component—it is positive only—so the envelope of convection events has a large-scale effect on the dynamics. Figure 3.1 provides an illustration. Convection is organized in events A and B, and  $\dot{\Sigma}$  is larger within the MJO envelopes. The organized convection along events A and B in Fig. 3.1d constantly puts mass into the shallow-water system while propagating eastward. This propagating mass source creates a large-scale eastward-propagating divergence (Fig. 3.1b). The envelopes of both the convection and the divergence have dc components. The dc components occupy a large horizontal area and persist for a long time. Therefore, the interference pattern of IG waves shows its unique dispersion character—low frequency and low wavenumber. The MJO structure in Fig. 3.4 is constructed from the low-frequency, low-wavenumber components in the Fourier domain. Therefore, it should show the large-scale response to the dc component of the convection envelope. That is why the MJO composites exhibit the quadrupole vortex structure instead of the IG wave structures.

We have done simulations with different sizes of convection by varying  $R$  from  $0.7^\circ$  to  $3.0^\circ$  with the T170 resolution. Both the propagation speed and the horizontal scale of the MJO do not show significant dependence on  $R$ . We have also varied the hyperviscosity by an

order of magnitude from the reference value,  $1.0 \times 10^{-4} \text{ m}^8/\text{s}$ , and the simulation results are still robust. The redness of the power spectrum is not a result of the hyperviscosity. Instead, it results from the persistence of the quasi standing wave and the convection that it triggers. The large scale is related to the large size of the envelope, which is the interference pattern of the IG waves.

### 3.6 Discussion and Conclusions

In this paper, we have presented a shallow-water model with triggered convection and simple radiation treatments. MJO-like signals are observed in our simulations. We propose that the MJO-like signal is an interference pattern of the WIG and EIG waves, whose frequency is set by the duration of individual convection events. Our simulation results suggest that the MJO is not a large-scale, low-frequency wave in which convection acts as a QE adjustment. Small-scale, high-frequency waves might be crucial. Therefore, in order to simulate the MJO, the behavior of moist convection in a short time period should be represented properly.

Moisture is implicit in our model. Triggered convection only occurs in a moist atmosphere, where conditional instability can exist. In a shallow-water model, the geopotential  $\phi$  is a measure of the static stability  $N^2$  of the atmosphere. Low  $\phi$  indicates reduced  $N^2$ . Only if  $N^2$  has been reduced to a critical value, in other words, CAPE has been accumulated by a certain amount, will convection be triggered. This mimics the processes of conditional

instability and triggered convection in a moist atmosphere with the minimum recipes.

Because of the simplicity of our model, we have to make assumptions about the MJO vertical structure and the Kelvin wave speed. Although these assumptions are consistent with observations, a complete theory will have to explain why the MJO has a first baroclinic structure, and why the Kelvin wave speed is about 16 m/s. The next step is to use a 3D model to test our hypothesis. We do not need to assume the MJO vertical structure and the Kelvin wave speed in the 3D model. To keep the key features of our current model, we will implement triggered convection in the 3D model. In this model, CAPE will be accumulated until convective inhibition falls below a certain value close to zero, thus making it more difficult for convection to occur. This allows a large amount of CAPE to accumulate before convection occurs.

The IG wave signal in our power spectrum is stronger than that reported in the observations (e.g., Fig. 1 of Kiladis et al. 2009). This could be due to the simplicity of our convection scheme. It is also likely due to the rectification by clouds. Clouds can spread and cover the IG waves, such that they do not show up clearly in the distributions of cloudiness or brightness temperature. Therefore, their variability is reduced in the OLR power spectrum. Instead, one would like to use dynamical variables like the zonal wind field to test our hypotheses. The correlation between the MJO and the IG waves has already been examined using observational datasets (e.g., Yang and Ingersoll 2011; Yasunaga and Mapes 2012). Statistically significant correlations have been identified, but the IG waves can only explain

very limited variance of the MJO. However, previous studies do not help to test our hypothesis. First, most of the previous studies used coarse temporal- and spatial-resolution datasets, so they cannot resolve high-frequency IG waves. A second problem is that these studies examined the correlations between the MJO and the WIG waves, and the MJO and the EIG waves separately. The interference pattern of the WIG and EIG waves is not even included. To test our hypothesis, one should first combine the WIG and EIG signals in a high-resolution dataset and identify their interference patterns. Then one should examine the correlations between the MJO and this identified interference pattern.

**Acknowledgments.** We thank two anonymous reviewers for their helpful comments. Da Yang was supported by the Earle C. Anthony Professor of Planetary Science Research Pool and the Division of Geological and Planetary Sciences Davidow Fund of the California Institute of Technology. He is currently supported by the Astronomy and Astrophysics Research Program of the National Science Foundation. We thank these organizations for their support.

## References:

Andersen, J. A., and Z. Kuang, 2012: Moist static energy budget of MJO-like disturbances in the atmosphere of a zonally symmetric aquaplanet. *J. Climate*, **25**, 2782–2804.

Arakawa, A., and W. Schubert, 1974: Interaction of a cumulus cloud ensemble with the large-scale environment, Part I. *J. Atmos. Sci.*, **31**, 674–701.

Benedict, J. J., and D. A. Randall, 2009: Structure of the Madden–Julian oscillation in the superparameterized CAM. *J. Atmos. Sci.*, **66**, 3277–3296.

Biello, J. A., and A. J. Majda, 2005: A new multiscale model for the Madden–Julian oscillation. *J. Atmos. Sci.*, **62**, 1694–1721.

Bretherton, C. S., P. N. Blossey, and M. Khairoutdinov, 2005: An energy-balance analysis of deep convective self-aggregation above uniform SST. *J. Atmos. Sci.*, **62**, 4273–4292.

Emanuel, K., 2007: Quasi-equilibrium dynamics of the tropical atmosphere. *The Global Circulation of the Atmosphere*, T. Schneider and A. H. Sobel, Eds., Princeton University Press, 186–218.

—, J. Neelin, and C. Bretherton, 1994: On large-scale circulations in convecting atmospheres. *Quart. J. Roy. Meteor. Soc.*, **120**, 1111–1143.

Fuchs, Z., and D. J. Raymond, 2002: Large-scale modes of a non-rotating atmosphere with water vapor and cloud–radiation feedbacks. *J. Atmos. Sci.*, **59**, 1669–1679.

Fuchs, Z., and D. J. Raymond, 2005: Large-scale modes in a rotating atmosphere with radiative–convective instability and WISHE. *J. Atmos. Sci.*, **62**, 4084–4094.

Fuchs, Z., and D. J. Raymond, 2007: A simple, vertically resolved model of tropical disturbances with a humidity closure. *Tellus*, **59A**, 344–354, doi:10.1111/j.1600-0870.2007.00230.x.

Hendon, H. H., and B. Liebmann, 1994: Organization of convection within the Madden-

Julian oscillation. *J. Geophys. Res.*, **99D**, 8073–8083.

———, and M. L. Salby, 1994: The life cycle of the Madden–Julian oscillation. *J. Atmos. Sci.*, **51**, 2225–2237.

Holloway, C. E., and J. D. Neelin, 2007: The convective cold top and quasi equilibrium. *J. Atmos. Sci.*, **64**, 1467–1487.

———, S. J. Woolnough, and G. M. S. Lister, 2012: Precipitation distributions for explicit versus parametrized convection in a large-domain high-resolution tropical case study. *Quart. J. Roy. Meteor. Soc.*, **138**, 1692–1708, doi:10.1002/qj.1903.

Khairoutdinov, M. F., and D. A. Randall, 2001: A cloud resolving model as a cloud parameterization in the NCAR community climate system model: Preliminary results. *Geophys. Res. Lett.*, **28**, 3617–3620.

Khouider, B., Y. Han, A. J. Majda, and S. N. Stechmann, 2012: Multiscale waves in an MJO background and convective momentum transport feedback. *J. Atmos. Sci.*, **69**, 915–933.

Kiladis, G. N., K. H. Straub, and P. T. Haertel, 2005: Zonal and vertical structure of the Madden–Julian oscillation. *J. Atmos. Sci.*, **62**, 2790–2809.

———, M. C. Wheeler, P. T. Haertel, K. H. Straub, and P. E. Roundy, 2009: Convectively coupled equatorial waves. *Rev. Geophys.*, **47**, RG2003, doi:10.1029/2008RG000266.

Lin, J.-L., and Coauthors, 2006: Tropical intraseasonal variability in 14 IPCC AR4 climate models. Part I: Convective signals. *J. Climate*, **19**, 2665–2690.

Madden, R. A., and P. R. Julian, 1972: Description of global-scale circulation cells in the tropics with a 40–50 day period. *J. Atmos. Sci.*, **29**, 1109–1123.

———, and ———, 1994: Observations of the 40–50-day tropical oscillation—A review. *Mon. Wea. Rev.*, **122**, 814–837.

———, and ———, 2005: Historical perspective. *Intraseasonal Variability in the Atmosphere—*

*Ocean Climate System*, W. K. M. Lau and D. E. Waliser, Eds., Springer, 1–18.

Majda, A. J., and S. N. Stechmann, 2009: The skeleton of tropical intraseasonal oscillations. *Proc. Natl. Acad. Sci. USA*, **106**, 8417–8422.

——, and ——, 2011: Nonlinear dynamics and regional variations in the MJO skeleton. *J. Atmos. Sci.*, **68**, 3053–3071.

Maloney, E. D., 2009: The moist static energy budget of a composite tropical intraseasonal oscillation in a climate model. *J. Climate*, **22**, 711–729.

Matsuno, T., 1966: Quasi-geostrophic motions in the equatorial area. *J. Meteor. Soc. Japan*, **44**, 25–43.

Moncrieff, M. W., 2004: Analytic representation of the large-scale organization of tropical convection. *J. Atmos. Sci.*, **61**, 1521–1538.

Nakazawa, T., 1988: Tropical super clusters within intraseasonal variations over the western Pacific. *J. Meteor. Soc. Japan*, **66**, 823–839.

Neelin, J. D., and J.-Y. Yu, 1994: Modes of tropical variability under convective adjustment and the Madden–Julian oscillation. Part I: Analytical theory. *J. Atmos. Sci.*, **51**, 1876–1894.

Raymond, D. J., and Z. Fuchs, 2009: Moisture modes and the Madden–Julian oscillation. *J. Climate*, **22**, 3031–3046.

Sobel, A. H., J. Nilsson, and L. M. Polvani, 2001: The weak temperature gradient approximation and balanced tropical moisture waves. *J. Atmos. Sci.*, **58**, 3650–3665.

Solodoch, A., W. R. Boos, Z. Kuang, and E. Tziperman, 2011: Excitation of intraseasonal variability in the equatorial atmosphere by Yanai wave groups via WISHE-induced convection. *J. Atmos. Sci.*, **68**, 210–225.

Tung, W.-W., and M. Yanai, 2002: Convective momentum transport observed during the TOGA COARE IOP. Part I: General features. *J. Atmos. Sci.*, **59**, 1857–1871.

Wang, B., 2005: Theories. *Intraseasonal Variability in the Atmosphere–Ocean Climate System*, W. K. M. Lau and D. E. Waliser, Eds., Springer, 307–360.

Wheeler, M., and H. H. Hendon, 2004: An all-season real-time multivariate MJO index: Development of an index for monitoring and prediction. *Mon. Wea. Rev.*, **132**, 1917–1932.

———, and G. N. Kiladis, 1999: Convectively coupled equatorial waves: Analysis of clouds and temperature in the wavenumber–frequency domain. *J. Atmos. Sci.*, **56**, 374–399.

Xu, K.-M., and K. A. Emanuel, 1989: Is the tropical atmosphere conditionally unstable? *Mon. Wea. Rev.*, **117**, 1471–1479.

Yang, D., and A. P. Ingersoll, 2011: Testing the hypothesis that the MJO is a mixed Rossby–gravity wave packet. *J. Atmos. Sci.*, **68**, 226–239.

Yasunaga, K., and B. Mapes, 2012: Differences between more divergent and more rotational types of convectively coupled equatorial waves. Part II: Composite analysis based on space–time filtering. *J. Atmos. Sci.*, **69**, 17–34, doi:10.1175/JAS-D-11-034.1.

Zhang, C., 2005: Madden-Julian oscillation. *Rev. Geophys.*, **43**, RG2003, doi:10.1029/2004RG000158.



## Chapter 4

# A Theory of the MJO Horizontal Scale\*

### 4.1 Abstract

Here we ask, what controls the horizontal scale of the Madden-Julian Oscillation, i.e., what controls its zonal wavenumber  $k$ ? We present a new one-dimensional (1D)  $\beta$ -plane model that successfully simulates the MJO with the same governing mechanism as the 2D shallow water model of *Yang and Ingersoll (2013)*. Convection is parameterized as a short-duration localized mass source that is triggered when the layer thickness falls below a critical value. Radiation is parameterized as a steady uniform mass sink. Both models tend toward a statistically steady state—a state of radiative-convective equilibrium, not just on a global scale but also on the scale of each MJO event. This gives  $k \sim (S_c/c)^{1/2}$ , where  $S_c$  is the spatial-temporal frequency of convection events and  $c$  is the Kelvin wave speed. We offer this scaling as a prediction of how the MJO would respond to climate change.

---

\* Appeared as: Yang, Da, and Andrew P. Ingersoll 2014: A theory of the MJO horizontal scale. *Geophys. Res. Lett.*, **41**, 1059–1064.

## 4.2 Introduction

The Madden-Julian Oscillation (MJO) is the dominant intraseasonal variability in the tropics. It is a slowly eastward propagating ( $\sim 5$  m/s) planetary-scale envelope of organized convection (Madden and Julian 1972, 1994; Zhang 2005). Within the large-scale envelope, there are both westward- and eastward-moving fine-scale structures (Nakazawa 1988).

Many previous studies consider the MJO as a large-scale unstable mode in the tropics, which is often referred to as the moisture mode. The moisture mode arises from positive feedbacks between precipitation and the source of moist static energy (e.g., Neelin and Yu 1994, Sobel et al. 2001, Fuchs and Raymond 2002, 2005, Bretherton et al. 2005, Fuchs and Raymond 2007, Maloney 2009, Raymond and Fuchs 2009, Andersen and Kuang 2012). Consistent with treating the MJO as a large-scale low-frequency mode, convection is usually treated as a quasi-equilibrium (QE) process (Emanuel et al. 1994). In the soft QE context, *i.e.*, finite time-scale convection, high-frequency waves are damped the fastest due to the moist convective damping effect (Emanuel et al. 1994). Therefore, the role of high-frequency waves has not really been evaluated in these theories.

However, there is growing evidence, both in the models and in the observations, suggesting that triggered convection might be important to the MJO. As opposed to QE convection, triggered convection allows the atmosphere to accumulate convective available potential energy (CAPE), and convection is therefore intermittent and energetic. For instance, Holloway et al. (2013) find that explicit convection simulations perform better than parameterized simulations in matching the strength and propagation speed of the MJO.

Models with a good MJO representation have increased generation of available potential energy and conversion of that energy into kinetic energy. These models also have a more realistic relationship between lower-free-tropospheric moisture and precipitation. Holloway *et al.* (2013) conclude that moisture-convection feedback is a key process for MJO propagation. Here we explore the idea that generation of CAPE by triggered convection is the important process. Zuluaga and Houze (2013) use radar-reflectivity fields, ECMWF ERA-interim reanalysis data, and three-hourly atmospheric soundings to examine the most extreme convective entities during the Dynamics of the MJO (DYNAMO) field project. Their analyses show that rainfall is intermittent and separated by non-rainy days during active phases of the MJO. They also show that CAPE increases before maximum rainfall accumulation and then decreases. The magnitude of change in CAPE is 200-300 J/kg. This result indicates that triggered convection does happen during the active phase of the MJO. They further propose that the rainfall intermittency is due to high-frequency equatorial waves.

Yang and Ingersoll (2013, hereafter YI13) developed a 2D shallow water model of the MJO that emphasizes the role of triggered convection and high-frequency waves. Convection is parameterized as a short-duration localized mass source and is triggered when the layer thickness falls below a critical value. Radiation is parameterized as a steady uniform mass sink. Over a wide range of parameters, they observed MJO-like signals (Figures 1, 3, and 4 in YI13) similar to the observed MJO in the upper troposphere. Based on their simulation results, YI13 proposed that the MJO could be an interference pattern of the westward and eastward (WIG and EIG) inertia gravity waves. The propagation speed of

the MJO is approximately equal to one-half the phase speed difference between the EIG and WIG waves.

In this paper, we further explore the YI13 model and seek a quantitative understanding of what controls the MJO horizontal scale. In section 2, we briefly describe the YI13 model, present the simulation results, and propose a radiative-convective equilibrium (RCE) scaling theory. In section 3, we derive a 1D  $\beta$ -plane model based on the YI13 model, and use this 1D model to test the RCE scaling. In section 4, we present our conclusions and plans for future work, and we discuss some possible climatological implications of our results.

### 4.3 2D Shallow Water Model

YI13 used a global 2D shallow water model to simulate the upper troposphere by assuming the MJO is dominated by the first baroclinic mode in the vertical. Thus divergence in this model refers to upper level divergence and low-level convergence. Similarly, small layer thickness in the model corresponds to low pressure aloft and high pressure near the surface, implying low average tropospheric temperature.

In YI13, we modify the 2D shallow water equations by adding convective heating  $q$  and radiative cooling  $r$  in the continuity equation, which is given by

$$\partial_t \phi + \nabla \cdot (\vec{V} \phi) = q - r. \quad (4.1)$$

In (1),  $\phi$  is the geopotential, which is gravity times the layer thickness;  $\vec{V}$  is the vector velocity, composed of zonal and meridional velocities. In this model, convection is a small-scale mass source, and is triggered when  $\phi$  is lower than a threshold  $\phi_c$ . The convective heating is given by:

$$q = \begin{cases} \frac{q_0}{\tau_c A_c} \left[ 1 - \left( \frac{\Delta t - \tau_c / 2}{\tau_c / 2} \right)^2 \right] \left( 1 - \frac{L^2}{R_c^2} \right), & \text{when } \phi < \phi_c, \quad 0 < \Delta t < \tau_c, \quad L^2 < R_c^2; \\ 0, & \text{otherwise.} \end{cases} \quad (4.2)$$

Here  $q_0$  is the heating amplitude,  $\tau_c$  is the convective timescale, and  $\Delta t$  is measured relative to the time when convection is triggered. Each convective event operates in a certain area  $A_c = \pi R_c^2$ , where  $R_c$  is the radius of each convective event. The convective heating will be superposed if one location sits between two separate convection events.  $\Delta t$  is then calculated separately for two events.  $L$  is distance from the convective center. Each convection event increases  $\phi$  by an amount  $\frac{q_0}{3}$  during its lifetime. The radiative cooling term  $r$  removes mass uniformly at a steady rate. In a statistically steady state,  $\phi$  fluctuates around the equilibrium geopotential  $\phi_c$ , and the convective heating balances the radiative cooling over the globe. According to this mass balance, we define the number density of convection  $S_c$ , with units number area<sup>-1</sup> time<sup>-1</sup>, as follows:

$$S_c = 3r / q_0. \quad (4.3)$$

We keep the forcing amplitude small, so the fluid dynamics is linear. Then we have 4 independent parameters in this model, and they are  $\tau_c$ ,  $R_c$ ,  $S_c$ , and the Kelvin wave speed  $c$ , defined as  $\sqrt{\phi_c}$ . The planetary radius  $a$  and the rotation rate  $\Omega$  define the length and time

scales of the problem. We systematically vary the first 4 parameters and explore the parameter dependence of the MJO wavenumber  $k$ , which corresponds to dimensional wavelength  $2\pi a/k$ .

Figure 4.1 shows the parameter dependence of  $k$  in 10-based log-log plots. Each marker represents one simulation result. To estimate  $k$ , we first construct the wavenumber-frequency diagram (*e.g.*, Fig. 3a in YI13). Then we search the wavenumber that occupies the most spectral power at each frequency in the MJO region, the white box area in Fig. 3a of YI13. The wavenumber of the MJO is the weighted average of these wavenumbers. In this study, we draw a wider white box than that in YI13 in both frequency and wavenumber to include the entire MJO spectral power.  $\log k$  increases linearly with  $\log S_c$ , and the slope is  $\sim 0.4$  (Fig. 4.1a).  $\log k$  decreases linearly with  $\log c$ , and the slope is  $\sim -0.7$  (Fig. 4.1b).  $\log k$  increases linearly with  $\log R_c$ , and the slope is  $\sim 0.5$  (Fig. 4.1c). In Fig. 4.1a, b, c, these linear relations suggest power law relations between  $k$  and  $S_c$ ,  $c$ , and  $R_c$ . These power law relations break down when  $k$  gets too small or too large. When  $k$  is close to 2, the MJO horizontal scale is large and is limited by the size of the planet. When  $k$  is 10 or above, we cannot distinguish one MJO event from another, and  $k$  is therefore saturated. In the next section, we construct a 1D model that solves an equatorial channel with large zonal domain and can avoid this problem. Figure 4.1d shows the  $k$  dependence on  $\tau_c$ . Although we have varied  $\tau_c$  by one order of magnitude,  $k$  does not change much, especially compared to other parameters. Therefore,  $k$  has a very weak dependence on  $\tau_c$ . Since  $k$  is a discrete number, there are uncertainties in estimating  $k$ , especially when  $k$  is small. In Fig. 4.1a, b, and c, the grey solid and dashed lines illustrate the largest and smallest slopes

calculated using simulations varying the corresponding x-axis variable only. This spread in slope is a measure of uncertainties in estimating  $k$ .

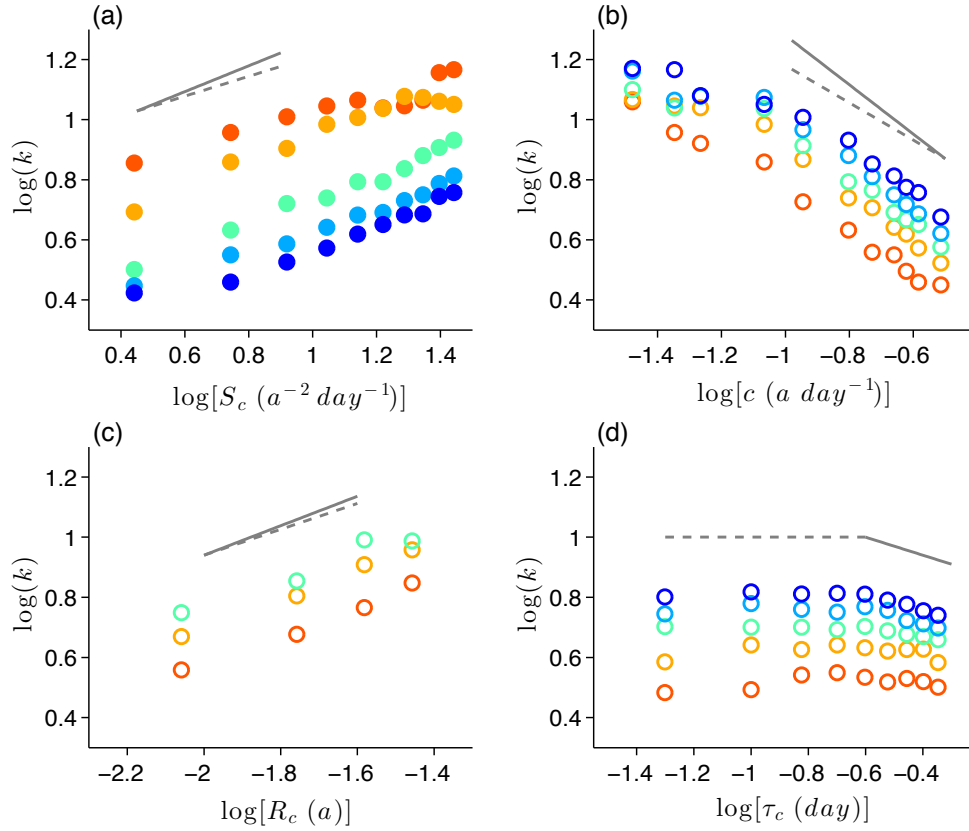


**Figure 4.1.** Sensitivity study results in 10-based logarithmic scale. (a) the MJO wavenumber  $k$  vs number density of convection  $S_c (a^{-2} \text{ day}^{-1})$ . Different colors represent simulations with different Kelvin wave speeds. They increase from red to blue, and the values are  $\sim 3, 6, 12, 16, 19 \text{ m s}^{-1}$ . The solid (dashed) line is with the slope of 0.43 (0.33). (b)  $k$  vs Kelvin wave speed  $c (a \text{ day}^{-1})$ . The solid (dashed) line has a slope of -0.82 (-0.62). (c)  $k$  vs the radius of a convection event  $R_c (a)$ . The solid (dashed) line has a slope of 0.43 (0.49). (d)  $k$  vs  $\tau_c (\text{day})$ . The solid (dashed) line has a slope of -0.3 (0.0). In (b), (c), and (d), colors represent simulations with  $S_c$  increasing from red to blue. The values of  $S_c$  are  $\sim (5.6 \ 11.2 \ 16.8 \ 22.4 \ 28.0) a^{-2} \text{ day}^{-1}$ .

According to our simulation results, we propose an empirical scaling relation between the MJO wavenumber and the model parameters

$$k = S_c^{0.4} R_c^{0.5} c^{-0.7} \Omega^{0.3} a^{1.1} F(\tau\Omega). \quad (4.4)$$

The exponents of  $\Omega$  and  $a$  are derived through dimensional analysis, and  $F(\tau\Omega) \sim O(1)$ . In Figure 4.2, we plot the simulation results according to (4). Most of the simulation results collapse into one curve. When  $k$  is between 2 and 10, this curve is linear and is parallel to the dashed line. Since the dashed line has the slope of 1, it suggests that the proposed scaling fits our simulation results.

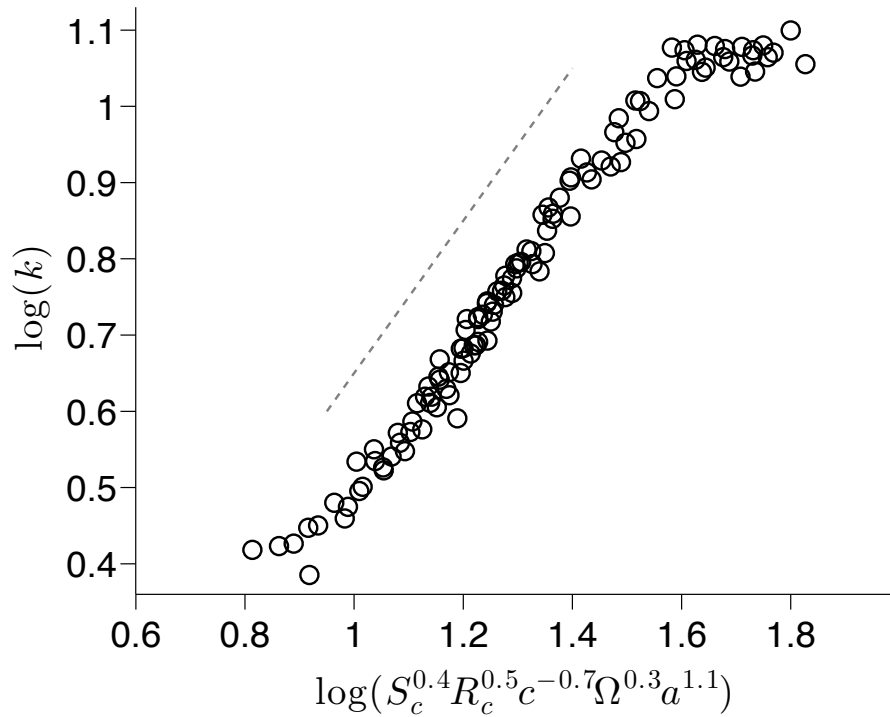


**Figure 4.2.** The proposed scaling relation in a 10-based log-log plot. Each marker represents a simulation result. The dashed line has a slope of 1.

Next we propose a simpler scaling that approximately reproduces the empirical scaling in (4.4). Since  $S_c$  is the number of convective events per unit area per unit time, we let each convective event occupy a box in space and time of dimensions  $L_z \times L_m \times T$ , where  $L_z = ak^{-1}$  is the zonal dimension,  $L_m \propto R_c$  is the meridional dimension, and  $T = ak^{-1}/c$  is the time dimension. This gives

$$k \sim S_c^{0.5} (R_c)^{0.5} c^{-0.5} a^{1.0} F(\tau\Omega) \sim (S_c R_c / c)^{1/2} a. \quad (4.5)$$

In effect, we are assuming that each MJO cycle is in RCE. On average, there is  $O(1)$  convective event within the box, which is defined partly by the MJO zonal scale  $L_z$  and the time it takes a gravity wave to propagate across that scale. We have associated the meridional dimension of the box with the size  $R_c$  of an individual convection event, although other interpretations are possible. That assumption has the advantage of giving the same  $R_c$  dependence in the two equations, (4.4) and (4.5). The MJO envelope is composed of many of these boxes defined above, which give the complex and multiscale structure of the MJO. It is difficult to compare our results with observations, e.g., precipitation inferred from infrared images (Chen *et al.* 1996), since it is not clear what constitutes an individual event in the sense we are using it. Nevertheless, the scaling of Eq. (4.5) is consistent with Fig. 1d of YI13, and that figure more or less matches the number of convective events seen in the infrared images.

Equations (4.4) and (4.5) are similar. The differences can be attributed to: 1) Each MJO event might not be in RCE because of interference between the MJO and mid-latitude activity, e.g., Rossby waves excited by convection at midlatitudes; 2)  $k$  is discrete, and the estimation of  $k$  is reliable only if  $k \gg 1$ . This situation, however, is never met, because  $k$

gets saturated when  $k \rightarrow 10$ . In other words, there are uncertainties when estimating  $k$ . To test this RCE scaling, we construct a 1D  $\beta$ -plane model. This 1D model does not have a meridional scale or interference from higher latitudes. Also, it has a much larger domain, so the uncertainties in estimating  $k$  are smaller.

#### 4.4 1D $\beta$ -plane Model

Since we keep the forcing amplitude small, and the MJO is confined to tropics, the linearized  $\beta$ -plane model keeps all the essential dynamics of the YI13 model. Following *Matsuno* (1966), we start with the 2D shallow water equations on an equatorial  $\beta$ -plane. To construct the 1D model, we assume the meridional structure of zonal wind  $U$ , meridional wind  $V$  and geopotential  $\phi$  as follows:

$$U = (u + by^2) \exp(-\beta y^2 / 2c), \quad (4.6)$$

$$V = vy \exp(-\beta y^2 / 2c), \quad (4.7)$$

$$\phi = (f + gy^2) \exp(-\beta y^2 / 2c). \quad (4.8)$$

$u$ ,  $v$ ,  $b$ ,  $f$ , and  $g$  are functions of  $x$  and  $t$ . After substitution into the equatorial  $\beta$ -plane equations, the  $b$  variable drops out, and we are left with four equations that exactly capture the lowest symmetric meridional modes—the Kelvin wave and the  $n = 1$  equatorial Rossby and inertia gravity (IG) waves. We use  $(c/\beta)^{1/2}$  as our length scale, and  $(\beta c)^{-1/2}$  as our timescale. The non-dimensional model equations are

$$\hat{u}_t = -\hat{f}_x, \quad (4.9)$$

$$\hat{v}_t = -\hat{u} - 2\hat{g} + \hat{f}, \quad (4.10)$$

$$\hat{f}_t = -\hat{u}_x - \hat{v} - \hat{r} + \hat{q}, \quad (4.11)$$

$$\hat{g}_t = -\hat{g}_x + \hat{v} - \hat{r} + \hat{q}, \quad (4.12)$$

where  $\hat{\cdot}$  represents nondimensional variables. Here  $\hat{r}$  is the radiative cooling, and  $\hat{q}$  is the convective heating. The radiation and convection parameterizations are the same as in the YI13 model. Convection is triggered when the geopotential  $\hat{f} + \hat{g}$  is lower than a threshold. The convective timescale is  $\hat{\tau}_c$ , and the size of each convection event is  $\hat{R}_c$ . In this 1D model, there are 3 nondimensional parameters,  $\hat{\tau}_c$ ,  $\hat{R}_c$  and  $\hat{S}_c = \frac{9}{8} \frac{\hat{r}}{\hat{q}_0}$ , where the proportionality comes from the temporal and spatial integration over the duration and size of each convective storm. Since there is no meridional dimension, the units of  $S_c$  are number  $\text{length}^{-1} \text{time}^{-1}$ , and  $R_c$  is the width of the convection in the zonal direction. The domain size of this model is 400 in the nondimensional units of the equatorial Rossby radius  $\sqrt{c/\beta}$ . This domain size is about 10 times larger than the Earth's equatorial circumference in the dimensional sense. In the previous section, wavenumber is a nondimensional quantity scaled by Earth's radius  $a$ , which is absent in this 1D model. In this part, we define the MJO nondimensional wavenumber  $\hat{k}$  as  $2\pi/\hat{\lambda}$ , where  $\hat{\lambda}$  is the MJO nondimensional wavelength.

Figure 4.3 shows the power spectrum of  $\hat{u}$  of the 1D model results. The most striking feature is the intense power density at low frequency and low positive wavenumber, which is associated with the MJO. The spectral power density is enhanced along the theoretical dispersion curves, which suggests that Kelvin waves and  $n = 1$  Rossby and IG waves are

present. The high-frequency IG waves are strongest among these equatorial waves. This may imply that the IG waves are important to the MJO. As this model keeps all the essential dynamics of the Y113 model, the governing mechanism of the MJO in this 1D model is the same as that of the 2D model. We will test the RCE scaling using this 1D model.

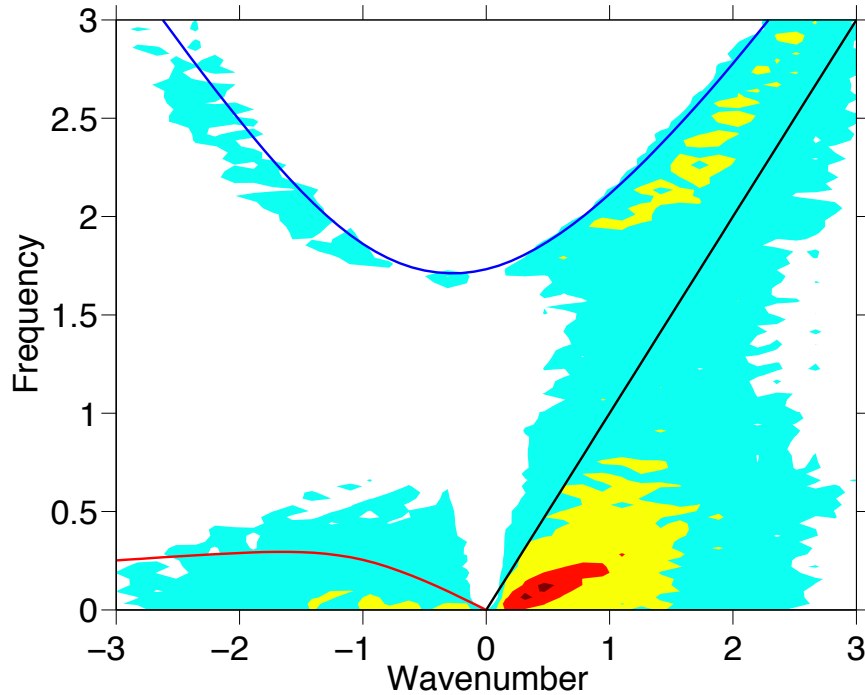


**Figure 4.3.** The power spectrum of  $\hat{u}$  from the 1D  $\beta$ -plane model. The contours show the power spectral density in intervals of log to the base 10. Red represents high-power density, and blue represents low-power density. Red, blue, and black lines denote dispersion curves of Rossby, IG, and Kelvin waves, respectively.

Figure 4.4 shows  $\hat{k}$  and  $\hat{S}_c$  in the 10-based logarithmic scale with different values of  $\hat{\tau}_c$  and  $\hat{R}_c$ . Each marker represents one simulation result. All of the simulation results collapse

onto one straight line with the slope of 0.54. The implication is that  $\hat{k}$  does not depend on  $\hat{\tau}_c$  and  $\hat{R}_c$ . An exponent of 0.50 would fit the RCE scaling, the dimensional form of which is

$$k \sim \left(\frac{S_c}{c}\right)^{1/2} . \quad (4.13)$$

Here  $k$  has dimensions of 1/length, whereas in (4.4) and (4.5)  $k$  was dimensionless, having been scaled by the Earth radius  $a$ . Another difference is that  $S_c$  is per unit length and time in (4.13) and per unit area and time in (4.5). Comparing the 1D scaling (4.13) with the 2D scaling (4.5), we confirm that the size of convection  $R_c$  only enters by affecting the meridional length scale. Physically, the horizontal scale of the MJO is the scale within which positive-only convective heating balances the radiative cooling. This has two consequences. First,  $k$  increases ( $\lambda$  decreases) with  $S_c$ . Our interpretation is that weaker convection (larger  $S_c$ ) can only balance radiation over a smaller scale, i.e., smaller MJOs (larger  $k$ ). Second,  $k$  decreases with  $c$ . Our interpretation is that if the gravity wave travels faster, it can spread the convective heating to further distance, i.e., larger MJOs (smaller  $k$ ).

## 4.5 Conclusion and Discussion

In this paper, we study what controls the MJO wavenumber by using the YI13 model and a 1D  $\beta$ -plane model. From our simulation results, we find a power law relation between  $k$  and the model parameters:  $S_c$ ,  $c$ , and  $R_c$ . Then we derive a scaling for  $k$  based on the assumption that each MJO event is in RCE, and this RCE scaling argument explains our

simulation results. This RCE scaling is consistent with the findings in YI13 that the positive-only convection produces the large-scale envelope of the MJO.

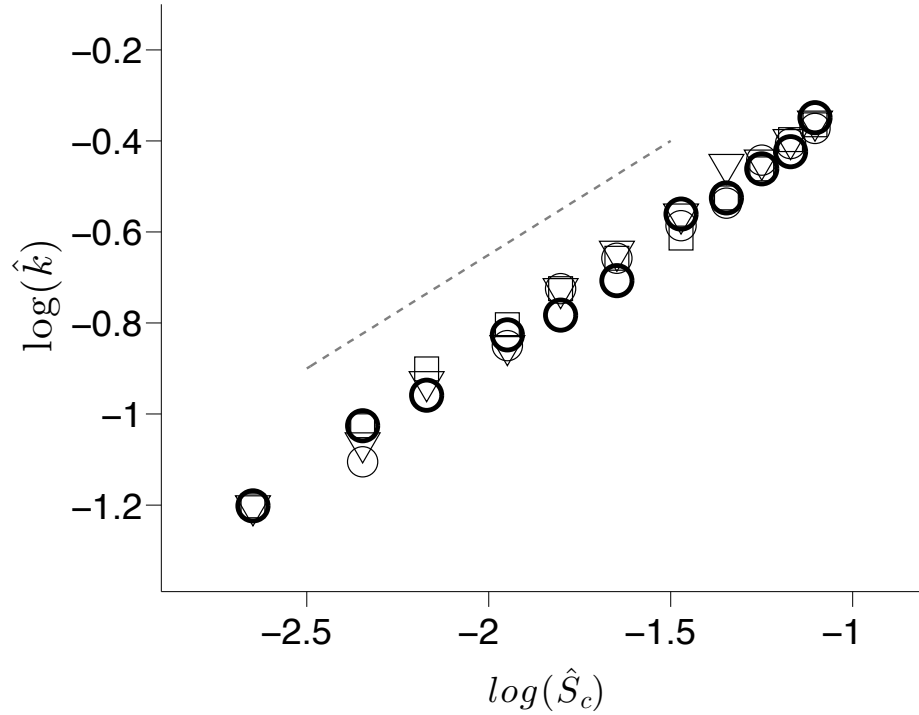


**Figure 4.4.** The 1D scaling relation in a 10-based log-log plot. Each marker represents a simulation result. The simulation results with  $\hat{R}_c = 0.4, 0.8, 1.6$  are labeled with squares, circles, and triangles. The simulation results with  $\hat{\tau}_c = 0.2$  and  $0.4$  are labeled with thick and thin markers. The dashed line has a slope of 0.5.

This success in simulating the MJO using both 1D and 2D models suggests that triggered convection might be important in simulating the MJO. With only three non-dimensional parameters, the 1D model is arguably the minimum model that includes all the essential recipes of the MJO—equatorial wave dynamics and self-excited, intermittent and energetic convective events. Although there is not a moisture variable in our model, we do not exclude the role of moisture in the MJO. Only with moisture could triggered convection

happen in the atmosphere. As a test of these low dimension models, we are simulating the MJO with a 3D moist GCM, in which triggered convection is applied.

One use of this study is to predict the MJO behavior in a different climate. In a warmer climate, convection is more vigorous (larger  $q_0$ ) and dry static stability increases. As a result,  $S_c$  will decrease and  $c$  will increase. If  $R_c$  does not vary,  $k$  will decrease according to (5). Meanwhile, the number of convection events in each MJO event is constant in different climates. In a warmer climate, the MJO is stronger because the convective events are more vigorous. Our prediction is qualitatively consistent with the SPCAM simulations (Arnold *et al.*, 2013). To test whether our scaling arguments could explain the SPCAM simulations quantitatively, we propose to run the SPCAM over a wide range of climates, and quantify  $q_0$ ,  $S_c$  and  $c$  in the SPCAM simulations.

**Acknowledgements.** Da Yang was supported by the Earle C. Anthony Professor of Planetary Science Research Pool and the Division of Geological and Planetary Sciences Davidow Fund of the California Institute of Technology. He is currently supported by the National Science Foundation under Grant No. AST-1109299. We thank these organizations for their support.

## References:

- Andersen, J. A., and Z. Kuang 2012: Moist static energy budget of MJO-like disturbances in the atmosphere of a zonally symmetric aquaplanet. *J. Climate*, **25**, 2782–2804.
- Arnold, N. P., Z. Kuang, and E. Tziperman 2013: Enhanced MJO-like Variability at High SST. *J. Climate*, **26**, 988–1001.
- Bretherton, C. S., P. N. Blossey, and M. Khairoutdinov 2005: An energy-balance analysis of deep convective self-aggregation above uniform SST. *J. Atmos. Sci.*, **62**, 4273–4292.
- Chen, S. S., R. A. Houze, and B. E. Mapes 1996: Multiscale variability of deep convection in relation to large-scale circulation in TOGA COARE. *J. Atmos. Sci.*, **53**, 1380–1409.
- Emanuel, K., J. Neelin, and C. Bretherton 1994: On large-scale circulations in convecting atmospheres. *Q. J. R. Meteorol. Soc.*, **120**, 1111–1143.
- Fuchs, Z., and D. J. Raymond 2002: Large-scale modes of a nonrotating atmosphere with water vapor and cloud–radiation feedbacks. *J. Atmos. Sci.*, **59**, 1669–1679.
- , and ——— 2005: Large-scale modes in a rotating atmosphere with radiative–convective instability and WISHE. *J. Atmos. Sci.*, **62**, 4084–4094.
- , and ——— 2007: A simple, vertically resolved model of tropical disturbances with a humidity closure. *Tellus*, **59A**, 344–354.
- Holloway, C. E., S. J. Woolnough, and G. M. S. Lister 2013: The effects of explicit versus parameterized convection on the MJO in a large-domain high-resolution tropical case study. Part I: Characterization of large-scale organization and propagation. *J. Atmos. Sci.*, **70**, 1342–1369.
- Madden, R. A., and P. R. Julian 1972: Description of global-scale circulation cells in the tropics with a 40–50 day period. *J. Atmos. Sci.*, **29**, 1109–1123.
- , and ——— 1994: Observations of the 40–50-day tropical oscillation—A review. *Mon.*

*Weather Rev.*, **122**, 814–837.

Maloney, E. D. 2009: The moist static energy budget of a composite tropical intraseasonal oscillation in a climate model. *J. Climate*, **22**, 711–729.

Matsuno, T. 1966: Quasi-geostrophic motions in the equatorial area. *J. Meteorol. Soc. Jpn.*, **44**, 25–43.

Nakazawa, T. 1988: Tropical super clusters within intraseasonal variations over the western Pacific. *J. Meteorol. Soc. Jpn.*, **66**, 823–839.

Neelin, J. D., and J.-Y. Yu 1994: Modes of tropical variability under convective adjustment and the Madden–Julian oscillation. Part I: Analytical theory. *J. Atmos. Sci.*, **51**, 1876–1894.

Raymond, D. J., and Z. Fuchs 2009: Moisture modes and the Madden–Julian oscillation. *J. Climate*, **22**, 3031–3046.

Sobel, A. H., J. Nilsson, and L. M. Polvani 2001: The weak temperature gradient approximation and balanced tropical moisture waves. *J. Atmos. Sci.*, **58**, 3650–3665.

Yang, D., and A. P. Ingersoll 2013: Triggered convection, gravity waves, and the MJO: A shallow-water model. *J. Atmos. Sci.*, **70**, 2476–2486.

Zhang, C. 2005: Madden-Julian Oscillation. *Rev. Geophys.*, **43**, RG2003, doi:10.1029/2004RG000158.

Zuluaga, M. D., and H. A. Robert 2013: Evolution of the population of precipitating convective systems over the equatorial Indian Ocean in active phases of the Madden-Julian Oscillation. *J. Atmos. Sci.*, **70**, 2713–2725, doi:10.1175/JAS-D-12-0311.1.



## Chapter 5

# Simulating the MJO in a 3D model with a convection threshold leading to intermittency\*

### 5.1 Abstract

It is still a challenge today to simulate the Madden-Julian Oscillation (MJO) in a 3D general circulation model (GCM) even though the MJO was first discovered 40 years ago. Here we simulate the MJO in an idealized GCM focusing on intermittent convection and high-frequency waves, which we suggest are essential to the MJO. We carry out four different experiments. We use the default GCM setup as the control simulation, and there is no MJO. We then make convection more intermittent by separately raising the convection threshold in three different variables: column integrated precipitable water, convective available energy (CAPE), and convection inhibition (CIN). The MJO emerges from each of these simulations with the observed drift rate and spatial structures, and the high-frequency waves are stronger in these simulations than in the control simulation. This is consistent

---

\* Submitted to *J. Atmos. Sci.* for publication.

with the Yang and Ingersoll (2013, 2014) hypothesis that the triggered convection and high-frequency waves are important to the MJO. This study has broader implications on improving GCM convection parameterizations.

## 5.2 Introduction

There are two distinct schools of MJO theories. One school considers the MJO as a large-scale, low-frequency unstable mode in the tropics, e.g., a moisture mode. It arises from moisture-convection feedback, i.e., positive feedbacks between convection and the source of moist static energy (MSE) (e.g., Neelin and Yu, 1994; Sobel et al., 2001; Fuchs and Raymond, 2002, 2005, 2007; Maloney, 2009; Raymond and Fuchs, 2009). Evidence comes from the fact that making deep convection sensitive to free troposphere moisture improves the MJO simulations in general circulation models (GCMs) (e.g., Grabowski, 2003; Bechtold et al., 2008; Holloway et al., 2013). Then convection is usually treated as a quasi-equilibrium (QE) process by emphasizing its effect on large-scale, slowly varying circulations. However, GCMs significantly underestimate the MJO variability, and simple models do not agree on the basic mechanisms.

The other school emphasizes the role of high-frequency, small-scale waves (e.g., Moncrieff 2004; Biello and Majda 2005; Majda and Stechmann 2009, 2011; Yang and Ingersoll 2011; Solodoch et al. 2011). Yang and Ingersoll (2013, 2014, hereafter YI13 and YI14) consider that the MJO is a large-scale, long-lasting envelope of small-scale high-frequency waves, and convection is a set of intermittent energetic events that are triggered when a certain threshold in the environment is exceeded. YI13 and YI14 suggest that the intermittency of

precipitation is key to simulating the MJO. YI13 develop a 2D shallow water model of the MJO that emphasizes the role of triggered convection and high-frequency waves. Convection is parameterized as a short-duration localized mass source and is triggered when the layer thickness falls below a critical value. Radiation is parameterized as a steady uniform mass sink. Over a wide range of parameters, they observed MJO-like signals with the observed drift rate and horizontal structures. Based on their simulation results, YI13 propose that the MJO could be an interference pattern of the westward and eastward inertia gravity (WIG and EIG) waves. The propagation speed of the MJO is approximately equal to one-half the phase speed difference between the EIG and WIG waves. YI14 present a 1D  $\beta$ -plane model that successfully simulates the MJO using the same governing mechanism as in the 2D YI13 model. Using this 1D model, they derive a scaling theory for the MJO horizontal wavenumber by assuming that each MJO event is in radiative-convective equilibrium (RCE). As a result, the MJO horizontal scale is the distance that the temperature anomaly can be effectively smoothed by gravity waves. This scaling theory says that the MJO wavenumber increases with the number density of precipitation events, and decreases with the Kelvin wave speed. This scaling theory further predicts that the MJO becomes stronger and larger in a warmer climate. This prediction is qualitatively consistent with recent superparameterized Community Atmosphere Model (SPCAM) simulation results (Arnold et al. 2013). In addition to the above theoretical studies, there is also growing observational evidence suggesting that the intermittency of precipitation and high-frequency waves might be important to the MJO (e.g., Nakazawa 1988; Tung and Yanai 2002; Kikuchi and Wang 2010; Zuluaga and Houze 2013).

In this paper, we will use a 3D GCM to further test if the intermittency of precipitation and high-frequency waves are important to the MJO. In section 2, we describe our model configuration and experiment setup. In section 3, we show our simulation results. In section 4, we present our conclusions, discussions, and plans for future work.

### 5.3 Model and Experiment Setup

We use a 3D moist GCM similar to those described by O’Gorman and Schneider (2008) and Frierson (2007). This GCM is based on the Geophysical Fluid Dynamics Laboratory (GFDL) spectral dynamical core and has a slab ocean as the lower boundary condition. There are no continents or solid surfaces. This GCM uses a gray radiation scheme and a simplified Betts-Miller convection scheme. This convection scheme relaxes temperature and moisture with a time constant of 2 hours to reference temperature and moisture profiles, which are calculated by assuming a pseudoadiabatic process with a fixed relative humidity of 0.8. In the control simulation, deep convection happens when both the convective available potential energy (CAPE) and the column water excess ( $\delta q$ ) are positive with respect to the reference moisture profile. In the original setup, this GCM cannot simulate the MJO (Frierson, 2007).

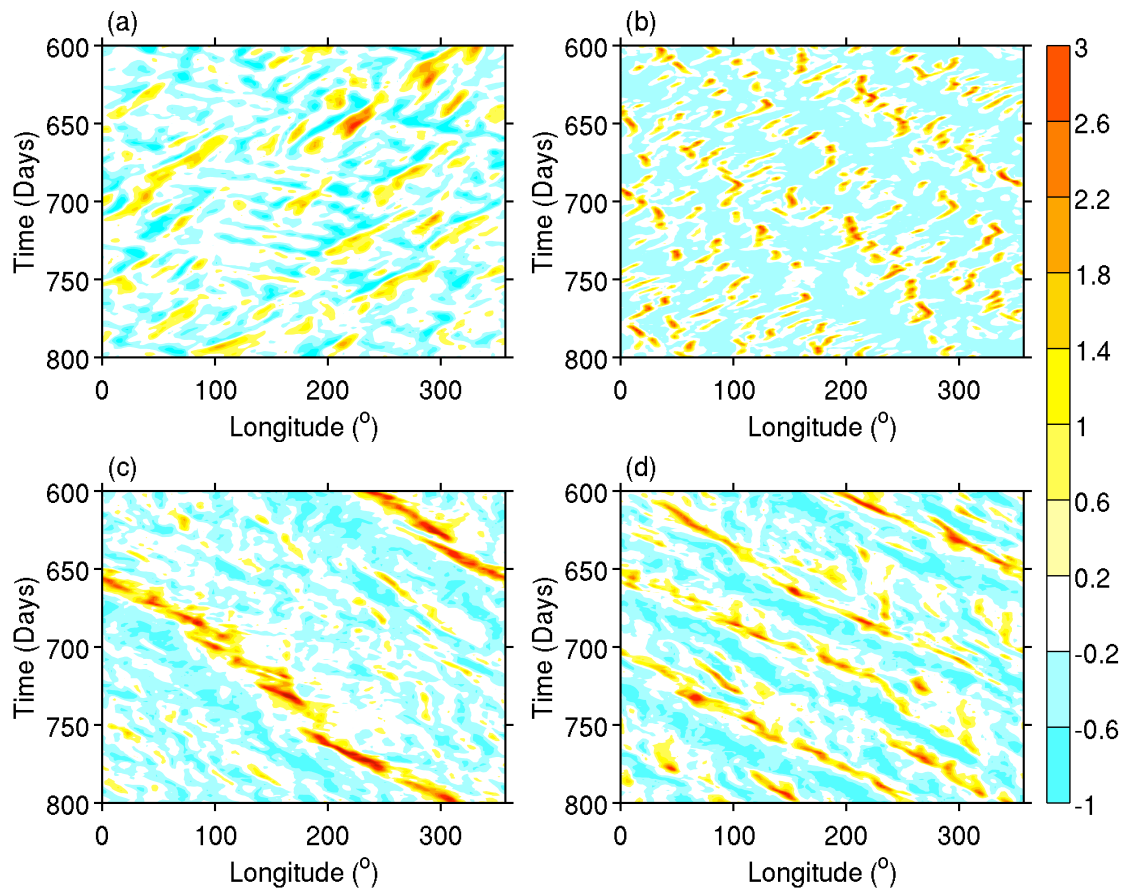
To test our hypothesis, we make precipitation more intermittent by raising the convection threshold in three different ways, i.e., convection only happens when  $\text{CAPE} > \text{CAPE}_o$ , when  $\delta q > \delta q_o$ , and when  $\text{CIN} < \text{CIN}_o$ , where CIN is convective inhibition—the minimum amount of energy to activate convection. Each of the above methods can make precipitation more intermittent, and we implement them separately. The simulations have

uniform short wave incoming radiation and globally uniform optical depth. This heavily reduces the meridional temperature gradient and therefore reduces the meridional moisture gradient.

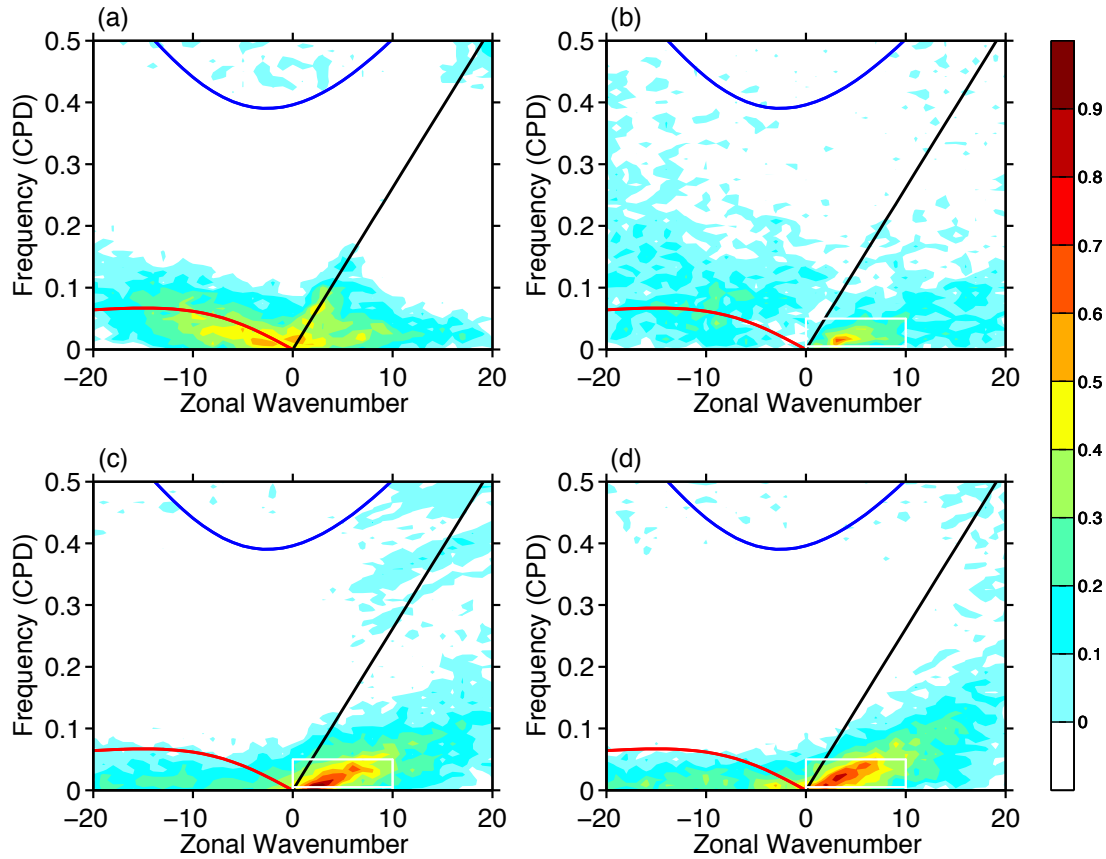
## 5.4 Simulation Results

Figure 5.1 shows the Hovmoller diagram of precipitation averaged over 10°S to 10°N. In the control experiment (Fig. 5.1a), there are both eastward propagating Kelvin waves and westward propagating equatorial Rossby waves, and most strong precipitation events propagate westward. The equatorial waves seen here are the convectively coupled waves. The Kelvin wave speed is  $\sim 20$  m/s and is significantly slower than the dry Kelvin wave speed, which is about 50 m/s. This reduction in speed has been documented in Frierson (2007) and is due to the reduction of effective static stability by moist convection. The MJO, however, is absent in this experiment. In the  $\delta q$  experiment (Fig. 5.1b), short-lived precipitation events mainly propagate westward, but the large-scale envelope of these precipitation events propagate eastward at  $\sim 2.3$  m/s and show wavenumber 3 structure. These large-scale envelopes are the MJO-like signals, and raising the precipitable water threshold can improve the MJO simulation. In the CAPE experiment (Fig. 5.1c), the large-scale long-lasting precipitation events are the dominant signals and propagate eastward at  $\sim 3.1$  m/s. There is a strong MJO event that loops the equator from day 600 to day 750. There are also weak ones with the same drift rate. According to this experiment, raising the CAPE threshold can improve the MJO simulation. In the CIN experiment (Fig. 5.1d), MJO-like signals dominate the precipitation. They show wavenumber 2 structure and propagate at  $\sim 3.9$  m/s. This suggests that raising the CIN threshold can also improve the MJO simulation.

We have so far improved the MJO simulation in one GCM with three different methods. One method—the  $\delta q$  experiment—has elements in common with the moisture-convection feedback, but the other two experiments do not. Since all three experiments can simulate the MJO, this suggests that the moisture-convection feedback is not essential to the MJO. The similarity in the above three methods is to make convection more intermittent and energetic. According to Y113 and Y114, such convection events will excite high-frequency waves that form the large-scale envelope of the MJO. This hypothesis puts these three different experiments in a coherent picture.



**Figure 5.1.** Hovmoller diagram of precipitation anomalies ( $\text{kg/m}^2/\text{s}$ ) averaged over  $10^\circ\text{S}$  to  $10^\circ\text{N}$ . (a) Control experiment, (b)  $\delta q$  experiment, (c) CAPE experiment, (d) CIN experiment. The precipitation anomaly has been multiplied by 3 to illustrate in the same color scale.



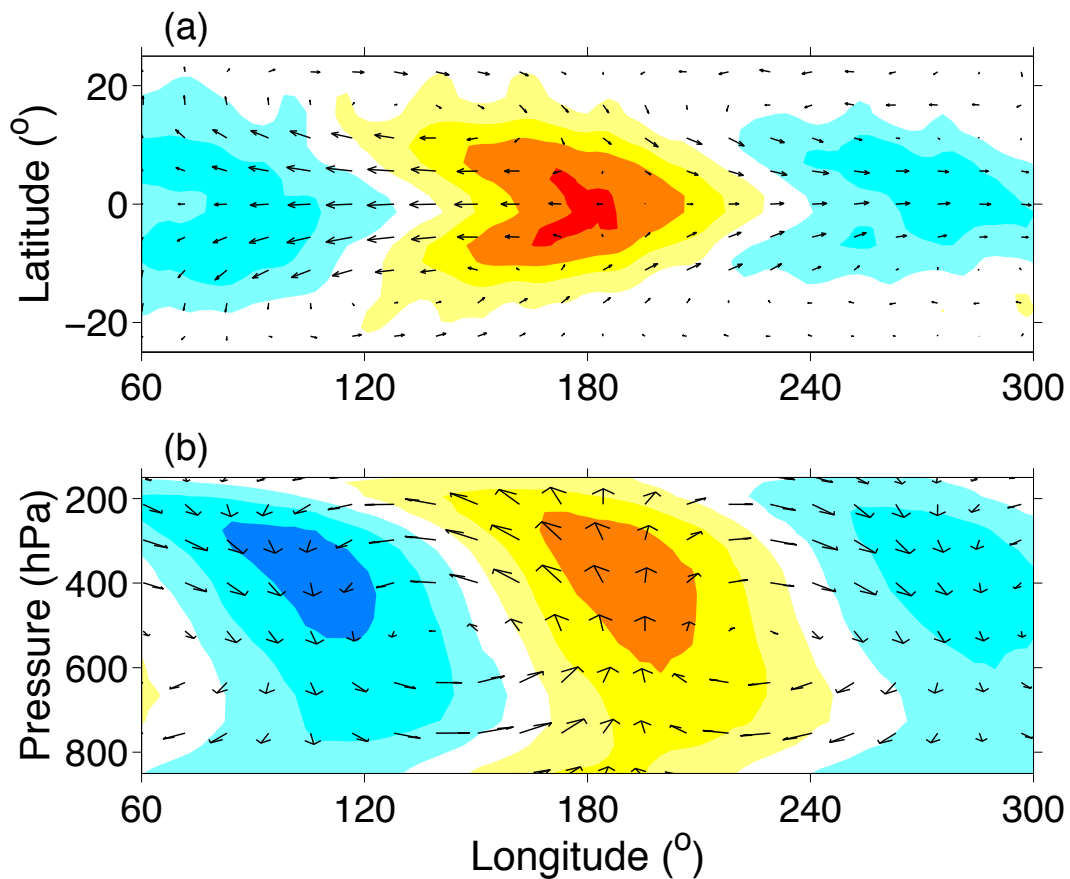
**Figure 5.2.** Power spectra of the symmetric component of precipitation averaged over  $10^{\circ}\text{S}$  to  $10^{\circ}\text{N}$  in 10-based logarithm scale. Background spectra have been removed. (a) Control experiment, (b)  $\delta q$  experiment, (c) CAPE experiment, (d) CIN experiment. The colors represent the spectral power density, and solid lines show the dispersion relations of the lowest order symmetric equatorial waves at 15 m equivalent depth. The black line represents the Kelvin wave, the red line represents the Rossby wave, and the blue line represents the IG wave. The white box contains the MJO signal.

Figure 5.2 shows the 2D power spectra of the symmetric components of precipitation averaged over  $10^{\circ}\text{S}$  to  $10^{\circ}\text{N}$  with the background spectra removed following Wheeler and Kiladis (1999). In the control experiment (Fig. 5.2a), there are both Rossby and Kelvin wave signals along the corresponding dispersion curves, but there is no MJO. In the  $\delta q$

experiment (Fig. 5.2b), the Rossby and Kelvin wave signals are weak along the corresponding dispersion curves, and there is a spectral peak within the white box in the low wavenumber and low frequency region. This spectral peak is associated with the MJO that we observed in Fig. 5.1b. In both the CAPE and CIN experiments (Figs. 5.2c and d), the Rossby and Kelvin wave signals are weak along the corresponding dispersion curves, and there are spectral peaks associated with the MJO. Compared to the control experiment, the CAPE and CIN experiments have weaker westward power and stronger eastward power in total. Figure 5.2 illustrates that, in the spectral domain, the experiments with raised convection threshold have better MJO simulations than the control experiment.

The MJO signals show similar spatial structures in all three experiments. Figure 5.3 shows the horizontal and vertical structure of the MJO composite in the CAPE experiment. The composites shown here are based on a widely used linear regression method (e.g., Anderson and Kuang 2012; Arnold et al., 2013), in which we filter the MJO precipitation signal by taking the Fourier coefficients within the white box (Fig. 5.2c) and transferring it back to the physical domain. Then we get the MJO composite in precipitation and use the precipitation time series at  $180^\circ$  longitude as the reference time series in regressing other fields. Figure 5.3a shows the upper level map view of the MJO composite. The active precipitation envelope of the MJO occupies  $\sim 100^\circ$  of longitude. The associated wind intrudes from the subtropics, diverges around the convective center along the equator and forms off-equatorial cyclonic and anticyclonic vortices to the east and west, respectively. This structure is consistent with the observed MJO horizontal structures (Kiladis et al. 2005). Figure 5.3b shows the vertical wind and specific humidity structures associated with

the MJO. The wind anomalies show the first baroclinic structure—lower level convergence and upper level divergence—around the convective center. Consistent with observations (e.g., Kiladis et al., 2005), the specific humidity shows a significant tilting structure with height, and there are positive specific humidity anomalies to the east of the MJO convective center at  $180^\circ$  longitude.



**Figure 5.3.** Horizontal and vertical structure of the MJO composite. (a) Map view of the MJO precipitation anomalies ( $10^{-4} \text{ kg/m}^2/\text{s}$ , colors). Vectors represent the MJO horizontal wind anomalies at  $\sim 200 \text{ hPa}$ . (b) Vertical cross section of the MJO. The color shows the correlation between the specific humidity and the MJO precipitation anomaly. The color interval in both panels is 0.1385, and white indicates zero correlation.

We have simulated MJO-like signals with the observed drift rate and the observed horizontal and vertical structures in  $\delta q$ , CAPE, and CIN experiments. The common feature of these experiments is raising the threshold for convection and increasing the intermittency of precipitation. Now we further test our hypothesis by examining if these simulations have stronger high-frequency waves compared to the control simulation, in which there is no MJO signal. Figure 5.4 shows the power spectra with MJO signals normalized by the control simulation power spectrum in the 10-based logarithm scale. There are three striking common features of these simulation results. First, relative to the control, there are strong high-frequency wave signals associated with IG waves in all three experiments. This supports the idea that the MJO is a large-scale envelope of high-frequency IG waves and is consistent with simple model simulation results in YI13 and YI14. It suggests that better simulating the high-frequency waves helps to improve the MJO simulations. Second, there are strong eastward propagating signals with frequencies below 0.5 CPD and wavenumbers from 10 to 40, labeled with white boxes. These signals do not fit in the equatorial wave dynamics, and the phase speeds of these signals are similar to the MJO speed. We interpret these enhanced signals as a by-product of the MJO. The MJO convection envelope provides a large-scale environment that favors convection, and the slowly eastward propagating convection variability is enhanced by the MJO envelope. Third, the Rossby and Kelvin wave signals are weaker than or similar to those in the control experiment. This suggests that Rossby and Kelvin waves are not essential to the MJO.

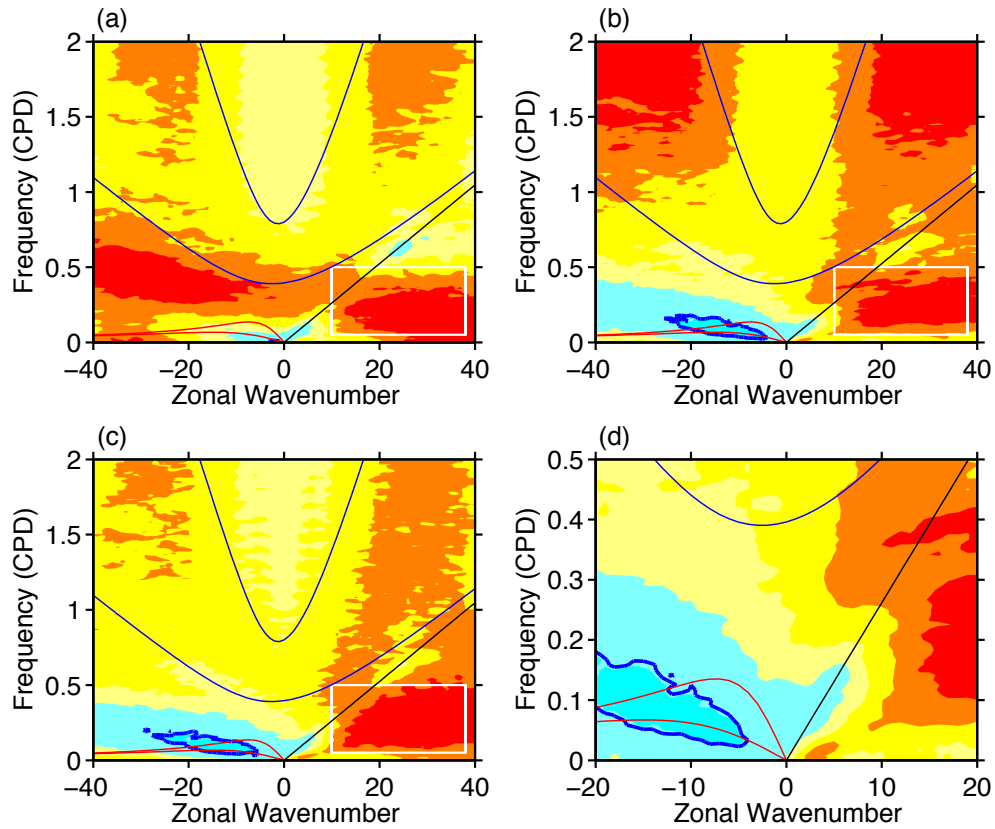


**Figure 5.4.** Normalized power spectrum of (a) the  $\delta q$  experiment, (b) the CAPE experiment, (c) the CIN experiment and (d) the CAPE experiment with zoomed in wavenumber and frequency range. Normalization means relative to the control experiment (Fig. 5.2a). The contour interval is 0.25 with a 10-based logarithm scale, and the zero line is labeled by the blue contour. The black line represents the Kelvin wave dispersion relation with equivalent depth as 15 m. The blue lines represent the IG wave dispersion relations with equivalent depths of 15 m and 250 m. The red lines represent the corresponding Rossby waves.

## 5.5 Conclusion and Discussions

We have simulated MJO signals through raising the convection threshold in three different ways in an idealized GCM. We find that the intermittent convection excites high-frequency waves, and these high-frequency waves are much stronger in the simulations with MJOs. This is consistent with the hypothesis in YI13 and YI14 and suggests that high-frequency waves are essential to the MJO.

This study implies that departures from QE convection are important. The importance of such departures has been recognized, and superparameterization has been used to capture departures from QE by including a small-scale cloud-resolving model in each GCM grid box (Grabowski 2001; Randall et al. 2003). Recent studies (e.g., Benedict and Randall 2009) with SPCAM show improved MJO simulations. Our next objective is to develop a convection scheme that accounts for the departures from the QE and can simulate the MJO.

This study is in contrast to previous studies that consider the MJO as a moisture mode, in which the moisture-convection feedback is essential. Recent moisture-mode studies investigate the MSE budget of the MJO and conclude that cloud-radiation feedback is the leading component of the MSE budget and is essential to the MJO (e.g., Anderson and Kuang, 2012; Arnold et al., 2013). Our simulations do not have cloud-radiation feedback, and yet they have an MJO-like signal. In addition, Anderson and Kuang (2012) suggest that drying to the west of the MJO convection center due to advection of subtropical dry air is important to the eastward propagation. However, our simulations have the same degree of moisture-convection feedback as in the control experiment, and yet the control experiment

does not have an MJO-like signal. Further our GCM is in the aquaplanet setup and is forced by grey radiation uniformly distributed in latitude. There is no meridional temperature gradient and no significant moisture gradient, and yet we still simulate the MJO. Our results suggest that cloud-radiation feedback, moisture-convection feedback, and the meridional moisture gradient, as identified in previous MSE budget analyses, are not essential to the existence and propagation of the MJO. This further suggests that the underlying mechanism of the MJO has not been revealed through the MSE budget analysis. Instead of driving the MJO, the anomalous MSE associated with the MJO might be a response of the already existing eastward propagating MJO.

We have, so far, only tested our hypothesis in this particular GCM. To further test the Yang and Ingersoll models, we will implement similar thresholds in other GCMs with different convection schemes and examine if the MJO simulation has been improved. In our  $\delta q$ , CAPE, and CIN experiments the equatorial Rossby waves and Kelvin waves are suppressed. Similar deficiencies have been found in other MJO simulations with simple convection schemes as well (e.g., Ajayamohan et al., 2013). We will investigate what process suppresses the equatorial Rossby and Kelvin waves in our model and use these tests to improve our convection scheme.

**Acknowledgements.** Da Yang was supported by the Earle C. Anthony Professor of Planetary Science Research Pool and the Division of Geological and Planetary Sciences Davidow Fund of the California Institute of Technology. He is currently supported by the National Science Foundation under Grant No. AST-1109299.

## References:

Ajayamohan, R. S., B. Khouider, and A. J. Majda, 2013, Realistic initiation and dynamics of the Madden-Julian Oscillation in a coarse resolution aquaplanet GCM, *Geophys. Res. Lett.*, **40**, 6252–6257, doi:10.1002/2013GL058187.

Andersen, J. A., and Z. Kuang, 2012: Moist static energy budget of MJO-like disturbances in the atmosphere of a zonally symmetric aquaplanet. *J. Climate*, **25**, 2782–2804.

Arnold, N. P., Z. Kuang, and E. Tziperman, 2013: Enhanced MJO-like Variability at High SST. *J. Climate*, **26**, 988–1001.

Bechtold, P., M. Kohler, T. Jung, F. Doblas-Reyes, M. Leutbecher, M. J. Rodwell, F. Vitart, and G. Balsamo, 2008: Advances in simulating atmospheric variability with the ECMWF model: From synoptic to decadal time scales. *Q. J. R. Meteorol. Soc.*, **134**, 1337–1351.

Benedict, J. J., and D. A. Randall, 2009: Structure of the Madden–Julian Oscillation in the Superparameterized CAM. *J. Atmos. Sci.*, **66**, 3277–3296.

Biello, J. A. and A. J. Majda, 2005: A new multiscale model for the Madden–Julian Oscillation. *J. Atmos. Sci.*, **62**, 1694–1721.

Bretherton, C. S., P. N. Blossey, and M. Khairoutdinov, 2005: An energy-balance analysis of deep convective self-aggregation above uniform SST. *J. Atmos. Sci.*, **62**, 4273–4292.

Frierson, D. M. W., 2007: Convectively Coupled Kelvin Waves in an Idealized Moist General Circulation Model. *J. Atmos. Sci.*, **64**, 2076–2090.

Fuchs, Z., and D. J. Raymond, 2002: Large-scale modes of a nonrotating atmosphere with

water vapor and cloud–radiation feedbacks. *J. Atmos. Sci.*, **59**, 1669–1679.

——, and ——, 2005: Large-scale modes in a rotating atmosphere with radiative–convective instability and WISHE. *J. Atmos. Sci.*, **62**, 4084–4094.

——, and ——, 2007: A simple, vertically resolved model of tropical disturbances with a humidity closure. *Tellus*, **59A**, 344–354.

Grabowski, Wojciech W., 2003: MJO-like Coherent Structures: Sensitivity Simulations Using the Cloud-Resolving Convection Parameterization (CRCP). *J. Atmos. Sci.*, **60**, 847–864.

Holloway, C. E., S. J. Woolnough, G. M. S. Lister (2013), The Effects of Explicit versus Parameterized Convection on the MJO in a Large-Domain High-Resolution Tropical Case Study. Part I: Characterization of Large-Scale Organization and Propagation, *J. Atmos. Sci.*, **70**, 1342–1369.

Kikuchi, K., B. Wang, 2010: Spatiotemporal Wavelet Transform and the Multiscale Behavior of the Madden–Julian Oscillation. *J. Climate*, **23**, 3814–3834.

Kiladis, G. N., K. H. Straub, P. T. Haertel, 2005: Zonal and Vertical Structure of the Madden–Julian Oscillation. *J. Atmos. Sci.*, **62**, 2790–2809.

Madden, R. A., and P. R. Julian, 1972: Description of global-scale circulation cells in the tropics with a 40–50 day period. *J. Atmos. Sci.*, **29**, 1109–1123.

——, and ——, 1994: Observations of the 40–50-day tropical oscillation—A review. *Mon. Wea. Rev.*, **122**, 814–837.

Majda, A. J. and S. N. Stechmann, 2009: The skeleton of tropical intraseasonal oscillations. *Proceedings of the National Academy of Sciences*, **106**, 8417–8422.

——, and ——, 2011: Nonlinear dynamics and regional variations in the mjo skeleton. *J. Atmos. Sci.*, **68**, 3053–3071, doi:10.1175/JAS-D-11-053.1.

Maloney, E. D., 2009: The moist static energy budget of a composite tropical intraseasonal oscillation in a climate model. *J. Climate*, **22**, 711–729.

Moncrieff, M. W., 2004: Analytic representation of the large-scale organization of tropical convection. *J. Atmos. Sci.*, **61**, 1521–1538.

Nakazawa, T., 1988: Tropical super clusters within intraseasonal variations over the western Pacific. *J. Meteor. Soc. Japan*, **66**, 823–839.

Neelin, J. D., and J.-Y. Yu, 1994: Modes of tropical variability under convective adjustment and the Madden–Julian oscillation. Part I: Analytical theory. *J. Atmos. Sci.*, **51**, 1876–1894.

Randall, D., M. Khairoutdinov, A. Arakawa, W. Grabowski, 2003: Breaking the Cloud Parameterization Deadlock. *Bull. Amer. Meteor. Soc.*, **84**, 1547–1564.

Raymond, D. J., and Z. Fuchs, 2009: Moisture modes and the Madden–Julian oscillation. *J. Climate*, **22**, 3031–3046.

Sobel, A. H., J. Nilsson, and L. M. Polvani, 2001: The weak temperature gradient approximation and balanced tropical moisture waves. *J. Atmos. Sci.*, **58**, 3650–3665.

Solodoch, A., W. R. Boos, Z. Kuang, and E. Tziperman, 2011: Excitation of Intraseasonal Variability in the Equatorial Atmosphere by Yanai Wave Groups via WISHE-Induced Convection. *J. Atmos. Sci.*, **68**, 210–225, doi:10.1175/2010JAS3564.1.

Tung, W.-W. and M. Yanai, 2002: Convective Momentum Transport Observed during the

TOGA COARE IOP. Part I: General Features. *J. Atmos. Sci.*, **59**, 1857–1871.

Yang, D. and A. P. Ingersoll, 2011: Testing the Hypothesis that the MJO is a Mixed Rossby-Gravity Wave Packet. *J. Atmos. Sci.*, **68**, 226–239, doi:10.1175/2010JAS3563.1.

Yang, D., and A. P. Ingersoll, 2013: Triggered Convection, Gravity Waves, and the MJO: A Shallow-Water Model. *J. Atmos. Sci.*, **70**, 2476–2486.

Yang, D., and A. P. Ingersoll, 2014: A theory of the MJO horizontal scale. *Geophys. Res. Lett.*, **41**, doi:10.1002/2013GL058542.

Zhang, C., 2005: Madden-Julian Oscillation. *Rev. Geophys.*, **43**, RG2003.

Zuluaga, M. D., and H. A. Robert, 2013: Evolution of the population of precipitating convective systems over the equatorial Indian Ocean in active phases of the Madden-Julian Oscillation. *J. Atmos. Sci.*, **70**, 2713–2725, doi:10.1175/JAS-D-12-0311.1.



## Chapter 6

### Conclusion and Discussion

#### 6.1 Conclusion

In this thesis, we study the nature of the MJO and focus on the role of high-frequency small-scale waves. Our major findings are in contrast to previous MJO theories that consider the MJO as a large-scale mode, and we summarize our findings here.

In Chapter 2, we test the hypothesis that the MJO is a wave packet of MRG waves. We simulate the MRG wave packet in an idealized GCM, and the simulated wave packet bears common features with the MJO, including propagation speed and horizontal scale. We use the OLR dataset to further test this hypothesis and find significant correlations between the MJO and the MRG wave packet. The MRG wave packet, however, can only explain limited MJO variance. In Chapters 3 and 4, we develop the first 1D and 2D models that successfully capture the basic features of the MJO. In these models, convection is a self-excited process and is treated as a set of small-scale, intermittent and energetic events. With only three non-dimensional parameters, our 1D model is the simplest model that can successfully simulate the MJO. Based on our simulation results, we propose that the MJO

is a large-scale envelope of westward and eastward inertia-gravity waves, and the propagation speed is determined by the east-west asymmetry of these waves. We further develop a scaling theory that accounts for the MJO horizontal scale and intensity. This scaling theory makes predictions on how the MJO responds to climate change. The successes in Chapters 3 and 4 suggest that triggered convection is important in simulating the MJO. In Chapter 5, we test if triggered convection could improve MJO simulations in GCMs. We implement triggered convection in a GCM by raising the convection threshold, and we observe robust MJO signals in our simulations. The theory presented in this thesis explains the basic features of the MJO and put the MJO-related observations and recent modeling progresses in a coherent picture.

## **6.2 Discussion**

To further confirm our theory and paint a complete picture of the MJO dynamics, we need more supportive evidence from observations. The high-frequency inertia-gravity waves are proposed to be the key, and yet they are weak in observations. One hypothesis is that the sampling rate of most observations is not high enough to resolve high-frequency inertia-gravity waves, and these waves are aliased into low-frequency signals. Another hypothesis is that not just the amplitude, but also the phase of these waves matters. Although each wave is weak, the collective amplitude can be strong if they are all in phase. Testing these hypotheses and searching observational evidence are definitely the direction we will follow.

